JUSTUS-LIEBIG-UNIVERSITÄT GIESSEN

DLR Deutsches Zentrum für Luft- und Raumfahrt

Effects of Cosmic Radiation on Active Implanted Medical Devices

DISSERTATION

zur Erlangung des
Doktorgrades der Naturwissenschaften
(Dr. rer. nat.)

Mona C. Plettenberg

II. Physikalisches Institut
Justus-Liebig-Universität, Gießen

Gießen, 2024

Erstgutachter:	Prof. Dr. Kai-Thomas Brinkmann Justus-Liebig-Universität, Gießen
Zweitgutachter:	Prof. Dr. Klemens Zink Technische Hochschule Mittelhessen, Gießen
Externe Betreuung:	Dr. Matthias M. Meier Deutsches Zentrum für Luft- und Raumfahrt, Köln

Zusammenfassung

In der immer älter werdenden Gesellschaft wächst die Zahl von Menschen mit aktiven implantierten medizinischen Geräten wie Herzschrittmachern, Kardioverter Defibrillatoren sowie Neurostimulatoren ständig. Gleichzeitig sind diese Personen der kosmischen Strahlung in der Atmosphäre auf Reiseflughöhen oder während starker solarer Teilchenereignisse ausgesetzt. In der Strahlentherapie ist es bereits bekannt, dass es zu Unregelmäßigkeiten in der Funktion dieser Geräte in Form von einem Zurücksetzen in einen suboptimalen Back-up Modus kommen kann. Diese werden insbesondere durch Neutronen ausgelöst, die ebenso eine bedeutende Komponente der kosmischen Strahlung sind. Allerdings wurden die Effekte von Teilchenstrahlung auf aktive implantierte Medizingeräte bisher nicht ausreichend quantifiziert.

Mithilfe eines Modelsystems, bestehend aus mehreren einfachen SRAM Chips, wurde eine Methode zur Vorhersage der Rate von Fehlfunktionen in verschiedenen Strahlungsumgebungen entwickelt. Es wurden die Effekte von Neutronen und Protonen verschiedenster Energien sowohl auf SRAMs als auch Herzschrittmacher und Defibrillatoren untersucht und Wahrscheinlichkeiten für Single Event Upsets bestimmt. Mithilfe von Wichtungsfunktionen wurden die Ergebnisse anschließend auf die Neutronenspektren der kosmischen Strahlung am Erdboden, auf Reiseflughöhen, während starker solarer Teilchenereignisse sowie der Protonentherapie angewandt und eine Effektrate bestimmt.

In den verschiedenen Szenarien am Erdboden und auf Reiseflughöhen wurde die Rate von Unregelmäßigkeiten in den Geräten als gering für die einzelne Person bestimmt, allerdings als nicht zu vernachlässigen hinsichtlich der Gesamtheit der weltweit im Einsatz befindlichen Geräte eingeschätzt. In der Strahlentherapie sowie bei starken solaren Teilchenereignisse auf Reiseflughöhen sind die Raten jedoch deutlich erhöht. Davon ausgehend ist eine Diskussion über Risikobewertung und eventuelle Strahlenschutzmaßnahmen möglich.

Abstract

In an ageing society, the number of people with active implanted medical devices such as pacemakers, cardioverter defibrillators and neurostimulators is constantly growing. At the same time, these people are exposed to cosmic radiation in the atmosphere at aviation altitudes or during severe solar particle events. In radiation therapy, it is already known that irregularities in the function of these devices can occur in the form of a reset to a suboptimal back-up mode. These are triggered in particular by neutrons, which are also a significant component of cosmic radiation. However, the effects of particle radiation on active implanted medical devices have not yet been sufficiently quantified.

Using a model system consisting of several simple SRAM chips, a method for predicting malfunctions in different radiation environments was developed. The effects of neutrons and protons of different energies on SRAMs as well as pacemakers and defibrillators were investigated and probabilities for single event upsets were determined. Using weighting functions, the results were consequently applied to the neutron spectra of cosmic radiation on the Earth's surface, at aviation altitudes, during severe solar radiation events, and proton radiation therapy to determine an effect rate.

In the various scenarios on the ground and at aviation altitudes, the rate of irregularities in the devices was determined to be low for the individual person but not negligible for the entirety of the devices in use worldwide. However, the rates are distinctly higher for radiation therapy and for severe solar radiation events at aviation altitudes. Based on this, a discussion on risk assessment and possible radiation protection measures is possible.

Erklärung

Ich erkläre: Ich habe die vorgelegte Dissertation selbständig und ohne unerlaubte fremde Hilfe und nur mit den Hilfen angefertigt, die ich in der Dissertation angegeben habe. Alle Textstellen, die wörtlich oder sinngemäß aus veröffentlichten Schriften entnommen sind, und alle Angaben, die auf mündlichen Auskünften beruhen, sind als solche kenntlich gemacht. Bei den von mir durchgeführten und in der Dissertation erwähnten Untersuchungen habe ich die Grundsätze guter wissenschaftlicher Praxis, wie sie in der „Satzung der Justus-Liebig-Universität Gießen zur Sicherung guter wissenschaftlicher Praxis“ niedergelegt sind, eingehalten.

Ort, Datum .....

(Mona Plettenberg)

Acknowledgements

I would like to express my sincere gratitude and appreciation to the many people who have played a significant role in the completion of my doctoral thesis. First of all, I would like to thank my supervisor Prof. Dr. Kai-Thomas Brinkmann for his valuable guidance, his great expertise, and continuous support in the pursuit of promising opportunities throughout the entire research journey. In addition, I would like to thank my second supervisor Dr. Matthias M. Meier for giving me the demanding opportunity to work on this project, for always supporting me the past years, and for challenging me to grow as a person and scientist.

I would like to extend my sincere thanks to Dr. Kai Schennetten for our detailed discussions, his tireless support during measurement campaigns, and continuous encouragement throughout the entire time. Furthermore, I would like to thank Dr. Daniel Matthiä who generously provided knowledge and expertise and helped me move forward with his valuable feedback and constructive suggestions. I am grateful to Dr. Karel Marsalek and Moritz Kasemann for their constant support in technical troubleshooting and for the extensive intellectual discussions we had in the past years. Finally, I would like to thank Dr. Hans-Georg Zaunick for his thoughtful comments and recommendations and for giving me the opportunity to take part in several measurement campaigns.

This endeavor would not have been possible without the generous support of the Studienstiftung des deutschen Volkes. I would like to thank the Institute of Aerospace Medicine at German Aerospace Center and especially PD Dr. Christine Hellweg for providing a conductive academic environment and resources necessary for my work. Finally, I would like to acknowledge the Helmholtz Graduate School for Hadron and Ion Research for their travel support and the impactful and inspiring courses.

I am thankful for the collaboration with Dr. Ehsan Berenjkoub and Dr. Frank Schwarm and their contributions that made my research possible. I would like to thank Dr. Kilian Baumann and Dr. Larissa Derksen for their collaboration, expertise, and support. Moreover, I would very much like to acknowledge all scientists and staff at the various irradiation facilities who helped to carry out successful measurements. A special thanks to RADNEXT for providing me with the two opportunities for beam time.

I could not have undertaken this journey without my colleagues, peers, and friends who

provided an encouraging and stimulating academic community, who guided me through thoughtful and inspiring conversations, and who kept me sane throughout my doctoral studies. I'm extremely grateful to my family, for their unwavering love and encouragement, their patience, and emotional support during this at many times extremely challenging academic pursuit. Finally, I would like to acknowledge all those whose support, advice, and encouragement may not be explicitly mentioned here but have undoubtedly influenced my academic journey. Thank you all for your invaluable contributions to the completion of this thesis.

Contents

List of Abbreviations

AIMD	Active Implanted Medical Device
Am-Be	Americium-Beryllium
BEOL	Back End of Line
CIED	Cardiac Implanted Electronic Device
CLK	Clock
CME	Coronal Mass Ejection
CMOS	Complementary Metal Oxide Semiconductor
COTS	Commercial of the Shelf
CRT	Cardiac Resynchronization Therapy
DDD	Dual Chamber Pacing
DUT	Device under Test
ERI	Elective Replacement Indicator
GANIL	Grand Accelerateur National d'Ion Lourds
GCR	Galactic Cosmic Radiation
GLE	Ground Level Enhancement
ICD	Implanted Cardioverter Defibrillator
LET	Linear Energy Transfer
MAUDE	Manufacturer and User Facility Device Experience
MC	Monte Carlo
MCU	Multiple Cell Upset
MISO	Master Input, Slave Output
MIT	Marburger Ionentherapiestrahlzentrum
MOSI	Master Output, Slave Input
PM	Pacemaker
PMMA	Polymethylmethacrylat
RPP	Rectangular Parallelepiped
SBU	Single Bit Upset
SEE	Single Event Effect
SER	Single Event Rate
SEU	Single Event Upset
SOBP	Spread Out Bragg Peak
SPE	Solar Particle Event
SPI	Serial Peripheral Interface
SRAM	Static Random Access Memory
TLD	Thermoluminescence Dosimeter
VVI	Ventricular Inhibitory Pacing

List of Figures

List of Tables

1. Introduction

Feeling your implanted, life-saving pacemaker suddenly having an atypical function while being on a plane must be a highly distressing situation. Marie Moe was on her way to Amsterdam when suddenly a muscle in her chest began twitching in the rhythm of her paced heartbeat. If the incident had not occurred just 20 minutes away from the destination, the pilot would have considered an emergency landing at an alternate airport. Upon arrival, immediate help waited for Marie Moe and she was subsequently hospitalized where a malfunction of her pacemaker was diagnosed (Baraniuk, 2022). The most probable cause: a particle from outer space which corrupted the data in the little computer in her chest. Was Marie Moe just an unlucky person or is there a significant risk to people with active implanted medical devices taking flights? How likely is the occurrence of adverse events in pacemakers and defibrillators due to cosmic radiation?

It is well-known that particle radiation can alter the memory of computers in so-called single event effects (Ziegler and Lanford, 1979). This particularly affects the space industry where spacecraft electronics is constantly exposed to intense cosmic radiation. Therefore, each component of the circuits is thoroughly evaluated for their sensitivity to radiation to ensure mission success. Especially memory chips are designed radiation hard from the outset or are extensively tested before they are sent to space.

Although attenuated through the Earth's magnetosphere and atmosphere, cosmic radiation is present at aviation altitudes and even on ground. In these environments, there have been several but rather anecdotal reports of single event effects, since it is difficult to prove that an electrical failure was caused by a cosmic particle. Only if all other potential causes for the reported events can be ruled out, cosmic radiation may be the sole remaining explanation. For example, there were exactly 4096 more votes counted than actually registered at a Belgian election which were traced back to a possible random and spontaneous bit flip in the memory of the voting machine (Willems et al., 2003). Furthermore, a plane suddenly pitched-down twice due to incorrect data in one of the inertial reference units of the avionics, causing serious injuries in several passengers and crew. In the final report of the Australian Transportation Safety Bureau it was speculated that a single event effect may have triggered the incident (Australian Transport Safety Bureau, 2008).

Similar to Marie Moe's experience, there have been some further reports in the sci-

entific literature about effects of cosmic radiation on active implanted medical devices. Ferrick et al., Clair et al., and Paz et al. describe in total 5 cases of implanted cardiac defibrillators with altered function after flights which they attribute to cosmic radiation (Ferrick et al., 2008; Clair et al., 2013; Paz et al., 2017). On that basis, Bhakta and Foreman concluded in their comment that further research is needed to correctly advise patients before air travel (Bhakta and Foreman, 2008). Nevertheless, it was still questionable if effects of particle radiation were actually a relevant issue for the millions of patients world-wide, apart from few isolated cases in air travel.

Besides the cosmic radiation environment, device malfunctions are a well-known complication in radiation therapy, occurring in approximately 3 % of all treatments (Zaremba et al., 2015). Multiple factors have been found to predict malfunctions, such as radiation and medical device type, or beam energy. Thus, many different national and international guidelines for the management of patients with cardiac implanted electronic devices in radiation therapy have been established (e.g.,Indik et al. 2017; Gauter-Fleckenstein et al. 2015). However, they are mostly based on observations and expert opinions (Malavasi et al., 2023). Consequently, there is need for a more sophisticated method for the prediction of device malfunctions due to particle radiation. Its development and subsequent application to several radiation environments as well as the consequent analysis of event rates after exposure to particle radiation was the main objective of this thesis.

Since medical devices are complex in their function, at first a model system was used to develop a method for radiation testing according to international standards. Simple static random-access memory chips were tested to investigate how they responded to neutron and proton radiation at different energies, how single event effects could be simulated and finally how the single event rate could be predicted in different radiation environments. This model later served as a reference tool in the actual testing of devices.

Once the travel restrictions due to the Covid Pandemic were lifted, measurements at different accelerator facilities across Europe were finally possible. Initial data for the model system were collected, the developed method was applied and subsequently verified. In cooperation with the Krankenhaus Porz am Rhein and the University Hospital Giessen, active implanted medical devices were eventually collected and the probability of effects due to hadronic radiation was assessed. Multiple particle energies were selected for testing since it was examined if there were different sensitivities at different neutron energy ranges. Subsequently, it was determined how often these devices experience malfunctions in arbitrary radiation environments. In particular, the event rates due to cosmic radiation on ground, at aviation altitudes, and during severe solar radiation events as well as during proton radiation therapy were investigated. In the end, this enables scientifically informed reflections on the risk for patients with implanted medical devices in certain radiation environments and discussions on necessary radiation protection measures.

2. Background

Before exploring the radiation sensitivity of pacemakers, defibrillators, and intrathecal infusion pumps in depth, it is crucial to discuss the mechanisms behind the induced adverse function of these devices. Therefore, the general operation and purpose of the active implanted medical devices are described. Furthermore, the radiation environments that the devices are exposed to are defined and characterized. Subsequently, the general effects of radiation on matter and the specific response of electronics, especially in memory circuits is explained. Finally, the method for calculating event rates of devices in various radiation environments is described.

2.1 Active Implanted Medical Devices

According to the EU Medical Device Regulation 2017/745 an active implanted medical device (AIMD) is defined as a device that depends on energy which is not generated by the human body to function. Moreover, the device must be designed to remain within the human body after it has been fully inserted during a medical procedure (EU, 2017, Article 2 (4-5)). This definition includes, e.g., cardiac implantable electronic devices (CIEDs) such as cardiac pacemakers (PM) and implanted cardioverter defibrillators (ICD) as well as neurostimulators, intrathecal infusion pumps, or cochlear implants. Various diseases of the heart, the nervous and the endocrine system can be managed with AIMDs. This can improve the quality of life noticeably and even save lives.

Since the first implantation of a pacemaker in Sweden in 1958, millions of people have received a device which helps to manage their cardiac disorders. In 2009, approximately 730 000 new pacemakers and 220 000 new ICDs were implanted in 61 countries leading to an estimation of 1.1 million patients receiving a CIED worldwide in that year (Mond and Proclemer, 2011). Due to our aging society and the concomitant increase of age related chronic cardiovascular or neurological diseases, the number of patients relying on AIMDs is overall expected to increase considerably in the next few years. In 2021, there were 73 000 pacemakers and 20 000 ICDs first-implanted in Germany alone. However, at least in this country the implantation of pacemakers has remained constant since 2011 while the numbers of ICDs decreased by 30 %, most likely due to more effective drug

(a) (b) (c)

Figure 2.1: Examples of active implanted medical devices: (a) pacemaker, (b) implanted cardioverter defibrillator, (c) intrathecal infusion pump.

treatments and changed guidelines. (Burger et al., 2024a; Burger et al., 2024b)

There is no recent absolute evaluation of patients with CIEDs. However, it is estimated that worldwide between 8 and 10 million people have a device implanted.

2.1.1 Cardiac Pacemakers

A cardiac pacemaker is an implanted device for the treatment of arrhythmias. It generates electrical pulses which are delivered to the ventricles or atria. Consequently, the chambers contract and ultimately pump blood. Therefore, an adequate heart rate can be maintained or restored. Leading indications for implanting a pacemaker are disruptions of the natural electrical conduction system of the heart such as atrioventricular blocks, or a dysfunction of the sinus node causing non-reversible bradyarrhythmia. (Glikson et al., 2021)

In general, a pacemaker consists of a pulse generator, a lead, and an electrode. An example device without lead and electrode is shown in Figure 2.1a. The pulse generator contains the electric circuitry and the battery and generates the electrical pulses. It is implanted in the chest or abdomen. The lead is an insulated wire which connects the generator with the cardiac chamber inside the heart. Finally, the electrode is attached to the target chamber. It senses the heartbeat and delivers an electric pulse if an inappropriate natural activity was detected. There may be a single lead that only paces the right ventricle or a double lead that additionally paces the right atrium. Cardiac resynchronization therapy (CRT) uses a third lead (biventricular pacemaker) that also stimulates the left ventricle. The latter therapy is especially used in a condition of heart failure. (Glikson et al., 2021)

2.1.2 Implanted Cardioverter Defibrillator (ICD)

Unlike cardiac pacemakers, an implanted cardioverter defibrillator provides defibrillation and/or cardioversion to prevent the risk of sudden cardiac death due to ventricular tachycardia or ventricular fibrillation. The device constantly monitors the heart rate. If a potentially life-threatening arrhythmia is detected, the device delivers a synchronized or non-synchronized electrical shock to restore a regular heart rhythm. Additionally, an ICD is capable of stimulating the heart, similar to cardiac pacemakers, to convert a sustained ventricular tachycardia or maintain an adequate heart rhythm during bradycardia. Consequently, the set-up of the two devices is comparable. ICDs also consist of a pulse generator, depicted in figure 2.1b, one to three leads for single chamber, dual chamber or biventricular stimulation and electrodes which are attached to the heart tissue. Additionally, the generator contains a capacitor to generate an electrical shock. (Glikson and Friedman, 2001)

2.1.3 Intrathecal Infusion Pumps

Patients with severe chronic pain or cancer pain can benefit from the implantation of an intrathecal infusion pump. Via a catheter, analgesics such as morphine, hydromorphone, or fentanyl can be delivered directly to the subarachnoid space between the spinal cord and the arachnoid membrane. The therapy is adapted to the pre-programmed patient's needs. Therefore, side effects due to oral and intravenous delivery can be reduced and a decrease in the systemic drug level is achieved (Belverud et al., 2008). Furthermore, intrathecal pumps are used to control spasticity in patients with several neurological diseases through direct delivery of Baclofen into the intrathecal space (Belverud et al., 2008).
The device consists of the main infusion pump which is implanted in the abdomen (shown in Figure 2.1c) and the connected catheter to the intrathecal space. Besides a peristaltic pump, the main device contains the electronics, the battery, an inert gas for pressurization, and the drug reservoir. It can be refilled through injections into the reservoir fill port.

2.2 Radiation Environments

Humans are constantly exposed to radiation originating from both artificial and natural sources. As an example, cosmic radiation from space interacts with atoms in the atmosphere and creates cascades of various secondary particles reaching aviation altitudes and ground levels. In addition, terrestrial radiation from the decay of naturally occurring radioactive isotopes such as radon, uranium, or thorium contributes to the natural radiation exposure. Moreover, people are exposed to radiation during medical procedures like x-ray examinations or radiation therapy. (Barth et al., 2003)

Any radiation environment is characterized by its particles. It can be composed of

different species, energies, and fluxes. Neutrons and other fast hadrons are of particular interest when investigating the effects of radiation in electronics. Hence, radiation environments containing a considerable number of neutrons such as cosmic radiation in the atmosphere and particle radiation therapy will be described in more detail.

2.2.1 Cosmic Radiation

The Earth's surface is permanently exposed to particles from space which was first described by Victor Hess in 1912 (Hess, 1912). The sources of cosmic radiation are divided into the galactic cosmic radiation (GCR) and the solar particle radiation emitted from the Sun. GCR originates in outer space from stars, supernovae, quasars and hot galactic and intergalactic plasma and impinges continuously and nearly isotropically on Earth. It consists of protons (83 %), alpha particles (13 %) and heavier nuclei (1 %) as well as electrons (3 %) and is highly energetic (Smart and Shea, 1985). In contrast, charged particles emitted from the Sun are typically less energetic. This so-called solar wind mostly consists of protons and some alpha particles and traces of heavier ions. Sporadically, solar storm events can occur where solar flares and coronal mass ejections (CMEs) generate a sharp increase in the particle flux including much higher energies than the usual solar wind.

Cosmic radiation in space is in particular relevant for the reliability of electronics, e.g., in satellites or spacecraft and the radiation protection of astronauts. Due to different shielding effects, the flux of cosmic radiation on Earth depends on the geomagnetic latitude, the activity of the Sun as well as the barometric altitude in the atmosphere. (Baumann and Kruckmeyer, 2019)

The Earth's magnetic field deflects charged particles depending on their angle of incident relative to the magnetic field lines. At the poles, the magnetic field lines are oriented almost vertically to the Earth's surface. Consequently, the mostly also vertically impinging cosmic particles are not deflected. Therefore, the shielding effect is reduced at higher latitudes compared to the equatorial region where the magnetic field lines are parallel to the surface and the cosmic particles are forced onto a curved path. The resulting effect of the magnetic field on the charged particle is modeled in the concept of the geomagnetic rigidity. It is defined using $R = \frac{p}{q}$ where p represents the momentum of the particle and q its charge. The unit is given in GV. A charged particle will only reach the atmosphere, if its rigidity is above a certain cut-off rigidity R_c which is specific for each geographic position (Smart and Shea, 2005; Matthiä et al., 2014). The higher R_c, the more shielding is observed.

Additionally, the observed GCR levels on Earth are affected by the modulation of the interplanetary magnetic field and solar wind speed in the 11-year solar cycle. Therefore, during solar minimum conditions, the observed GCR intensity is elevated while it is attenuated during solar maximum conditions (Barth et al., 2003).

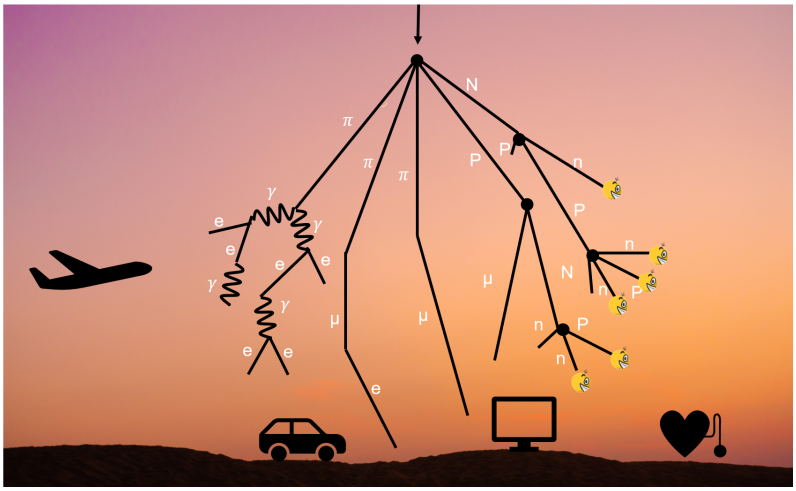

Figure 2.2: Cosmic radiation shower in the atmosphere showing neutrons (n), protons (P), pions (π), muons (μ), electrons (e), gamma-photons (γ) and other nuclei (N), adapted from (Baumann and Kruckmeyer, 2019).

Cosmic Radiation in the Atmosphere

Effects of cosmic radiation at aviation altitudes and at ground levels are highly relevant for electrical devices in the automotive industry, in avionics, supercomputers, and potentially for patients with AIMDs. When cosmic particles penetrate the Earth's atmosphere, they interact with its atoms (78 % nitrogen and 21 % oxygen) (Barth et al., 2003). Thus, secondary particles such as neutrons, protons, electrons, positrons as well as short-lived pions and muons are generated in a particle cascade (Matthiä et al., 2014). This is illustrated in figure 2.2. The atmospheric shielding is given by the atmospheric depth which represents the mass of the air above the measuring point. With increasing altitude, the atmospheric depth decreases, thus, the shielding of the atmosphere is reduced (Goldhagen, 2003). Charged particles like low-energy protons and electrons are attenuated through the Coulomb interaction with the atmospheric matter and are therefore less abundant on ground level (Matthiä et al., 2014). In contrast, the generated secondary neutrons mostly interact through scattering and reach lower regions of the atmosphere in a greater proportion and are thus further discussed (Barth et al., 2003). Due to the atmospheric shielding, less than 1 % of the primary flux of GCR can be detected on ground levels (Baumann and Kruckmeyer, 2019).

As an example, for the shielding effect of the atmosphere, the differential neutron flux at two exemplary altitudes is shown in figure 2.3a. It was calculated using the PANDOCA model (Matthiä et al., 2014) for a free atmosphere without ground effects at solar minimum and a cut-off rigidity of 4 GV (Personal Communication Matthiä, 2024). The two altitudes represent an aviation altitude at 41 000 ft and the top of the highest mountain in Germany, the Zugspitze at 8600 ft. It is evident that for the energies below 500 MeV, the differential

neutron flux is reduced by a factor of 20 at the top of the mountain compared to the aviation altitude.

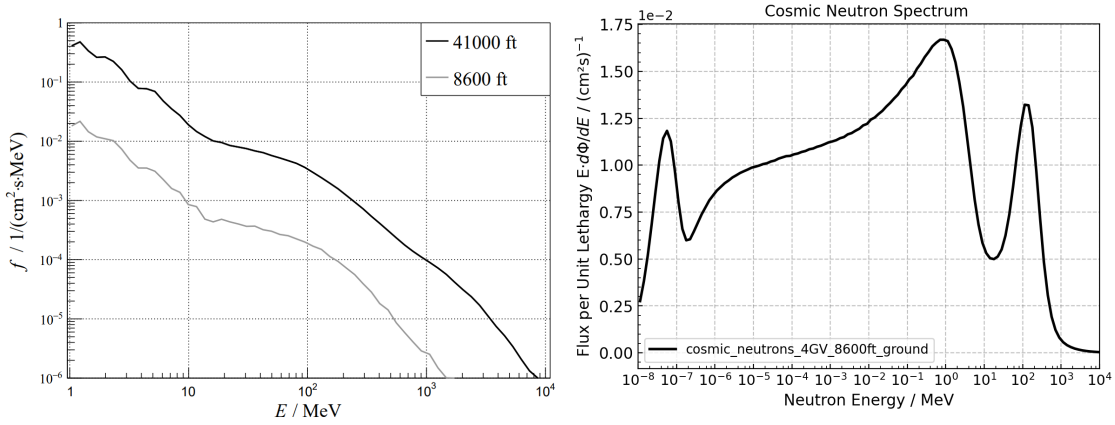

(a) (b)

Figure 2.3: a)Modeling of the differential neutron flux at two different altitudes during solar minimum and R_c = 4 GV calculated with the PANDOCA model (Matthiä et al., 2014). b) The differential neutron flux multiplied by the neutron energy for 8600 ft during solar minimum and R_c = 4 GV on ground calculated using the EXPACS tool (Sato, 2015).

When multiplying this continuous differential cosmic neutron flux by the neutron energy, the flux is given per lethargy which is mathematically equivalent to $d\Phi/d(ln(E))$. This representation simplifies the interpretation of the contribution of the fluxes at different energies to the full spectrum, given that same-sized areas under the curve exhibit an equal integral flux (Bartlett et al., 2003). As a result, three broad peaks become clear in this representation of the cosmic neutron spectrum. This is exemplarily shown for the energy spectrum at the Zugspitze in 2.3b. The first peak appears in the thermal energy range below 1 eV where the neutrons are in thermal equilibrium with the atoms in the surrounding matter. The plateau region between the epithermal ranges and approximately 0.1 MeV is the result of scattering processes of neutrons with atmospheric matter. In this energy range, they are decelerated until they reach thermal equilibrium which means that $d\Phi/dE$ is approximately proportional to $1/E$ (Gordon et al., 2004). A second broad peak, can be identified between 0.1 MeV and 10 MeV with a maximum at 1 MeV and is known as the nuclear evaporation peak. It can be attributed to the emission of neutrons from excited atmospheric nuclei following an interaction with high-energy protons or neutrons. Furthermore, fine structures as the result of nuclear resonances in oxygen and nitrogen nuclei of the atmosphere might be identified in this energy range (Goldhagen et al., 2004). Finally, there is a high-energy peak with a maximum at 100 MeV. It is generated by high-energy cosmic particles directly interacting in spallation reactions with nuclei of the upper atmosphere (Köhli et al., 2021).

Especially, neutrons with energies above 10 MeV are of significance regarding the induction of radiation effects in electronics, given the high probability of the generation of free charge carriers in the matter of the devices (Gordon et al., 2004). In some electronics, the thermal peak may also be relevant.

Cosmic Radiation Environment on Ground

On ground levels, the shape of the neutron spectrum is considerably influenced by many factors. This includes surrounding objects and elements as well as the weather and air-humidity (Dirk et al., 2003; Köhli et al., 2021). In particular, the thermal neutron flux strongly depends on the local environment due to scattering effects. On the one hand, there may be a shielding effect, e.g., of buildings, on the other hand, the neutrons may be moderated in hydrogen-rich materials which increases the thermal component considerably. As a consequence, the flux at thermal energies is not homogeneous and needs to be measured for full characterization. The standard for radiation effects testing in electronic devices on ground JEDEC JESD89B suggests a reference neutron spectrum in which a thermal neutron flux of $6.5\,\mathrm{cm^{-2}h^{-1}}$ and a high energy neutron flux above 10 MeV of $13\,\mathrm{cm^{-2}h^{-1}}$ are assumed. This leads to a thermal to high energy ratio of 0.5 in the reference environment (JEDEC, 2021).

In addition to neutrons, muons can reach the Earth's surface in considerable numbers. However, their effect on electronic devices is negligible (Baumann and Kruckmeyer, 2019).

Cosmic Radiation Environment at Aviation Altitudes

At aviation altitudes of about 40 000 ft, protons are not as attenuated as on ground. Therefore, their abundance above an energy of 10 MeV needs to be included for the analysis of radiation effects. Similar to the ground level environment, there is a standard for testing the effects of radiation effects in avionics. The IEC62396-1 states a reference flux for neutrons and protons combined of $6000\,\mathrm{cm^{-2}h^{-1}}$ for the high energy component above 10 MeV (IEC, 2016). It is assumed that the effect of the aircraft structure on neutrons is negligible above this energy. In contrast, the fraction of the thermal neutron component in the free atmosphere is comparably low, since there is no moderation from ground materials (Weulersse et al., 2018). However, inside an aircraft, hydrogen-rich objects like the fuel and the baggage, as well as the bodies of the passengers are present. Therefore, neutrons are thermalized and the thermal component of the neutron spectrum can be considerably increased dependent on the location inside the plane according to Monte-Carlo calculations by Dyer and Lei (Dyer and Lei, 2001). They conclude that the thermal neutron flux inside an aircraft might be two times higher than the high-energy neutron flux. The standard for testing radiation effects in avionics (IEC62396-5) proposes

a ratio between the thermal and high-energy neutron fluxes of 1.1 (Weulersse et al., 2018). However, recent measurements at different positions on board an aircraft indicated that the thermal neutron flux might only be one third of the high-energy neutron flux (Weulersse et al., 2023).

Cosmic Radiation Environment during Increased Space Weather Activity

Space weather describes the effects of the Sun on the conditions in the surrounding space. It is characterized by the solar activity and its effect on Earth's magnetosphere and ionosphere (Singh et al., 2010). In particular, coronal mass ejections (CME) in which huge amounts of gas and plasma are suddenly emitted from the coronal region of the Sun and solar flares which are described as the release of a large amount of energy in a short period of time from active regions of the Sun, drive the space weather. These phenomena can lead to, e.g., geomagnetic storms, the auroras, or ionospheric disturbances. During strong solar events, serious effects on technology and humans in space and on ground may be observed, e.g., the degradation of high frequency communications and radar systems, the induction of geomagnetically induced currents in power lines, or the impairment of satellite operation (Singh et al., 2010). Some solar particle events (SPEs) can lead to increased particle radiation levels in space which may have serious effects on the electronics of satellites and may result in the exposure of astronauts to high doses of radiation outside shielded areas (Singh et al., 2010). If the spectrum of the SPE is hard enough and there is a significant component of particles with energies of more than several hundreds of MeV, an increased neutron flux in the atmosphere and even on ground will be measured by, e.g., neutron monitors (Dyer et al., 2017). If two or more neutron monitors at different locations, one of which is situated near sea level, concurrently register a significant enhancement in their count rates, this will be referred to as ground level enhancement (GLE) (Poluianov et al., 2017).

As an example, figure 2.4 depicts GLE69 from 20.01.2005 and GLE42 from 29.09.1989 recorded at the Oulu Cosmic Ray Station of the University of Oulu / Sodankyla Geophysical Observatory in Finland (Usoskin, 2024). The GLE69 had an enhancement of the local neutron flux of about 260 % in its peak. In the beginning the event was characterized by a hard spectrum and a strong anisotropy, especially on the southern hemisphere which subsequently developed into a softer spectrum and a more isotropic character (McCracken et al., 2008). Similarly, the GLE42 was very anisotropic in the beginning and a rapid change in its spectrum over the course of the event was observed (Lovell et al., 1998). However, it did not reach the high local enhancement of GLE69 in Oulu. Dyer et al. calculated the neutron flux at 12 km for the GLE42 and found an increase by a factor 200 compared to background cosmic radiation at this altitude (Dyer et al., 2003). The same group likewise analyzed the strongest so far recorded GLE5 from 23.02.1956 and concluded that an event

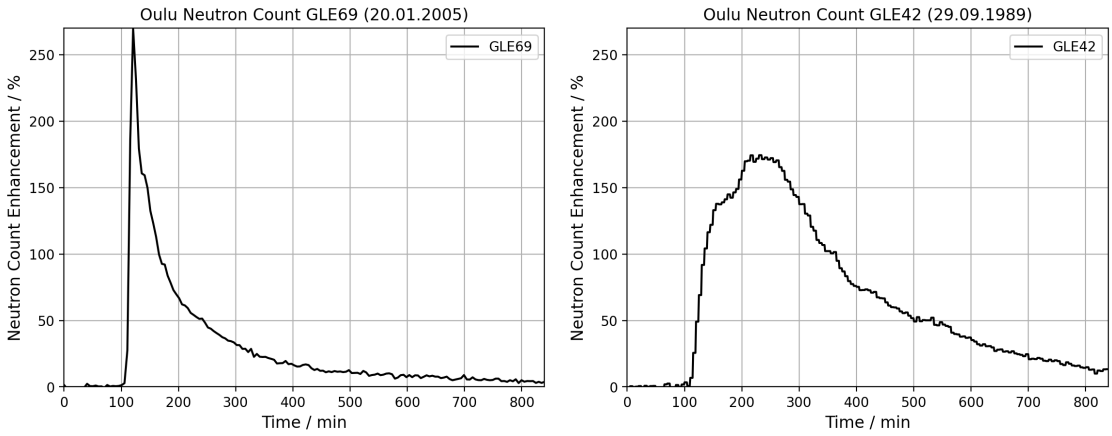

(a) GLE69 (b) GLE42

Figure 2.4: GLE69 and GLE42 neutron monitor data from Oulu (R_c = 0.81 GV, alt = 15 m) extracted from (Usoskin, 2024).

at this strength can cause considerable effects in avionics. Based on this event and cosmogenic nuclide data from historic events, they predicted neutron fluxes above energies of 10 MeV for severe events occurring, e.g., once in 150 years. Accordingly, the combined neutron and proton flux at 40 000 ft and a cut-off rigidity 0 GV could potentially reach $2.5 \cdot 10^7\,\mathrm{cm^{-2}h^{-1}}$. The authors concluded that during such events, even electronics on ground might be severely affected. (Dyer et al., 2017)

2.2.2 Radiation Therapy

Radiotherapy is a common therapy method in cancer treatment, with around 50 % of all cancer patients receiving irradiation (Yap et al., 2016). Mostly photons and protons but also other forms of ionizing radiation are used to treat primary tumors. The mixed secondary radiation field in radiotherapy is very complex and depends on the type, energy and location of the irradiation in the patient's body (Kry et al., 2017). Secondary photons, neutrons, protons and electrons contribute to doses outside of the primary target and can ultimately have an effect on AIMDs. However, it is difficult to characterize this secondary radiation field and different methods in a combination of simulations and measurements must be applied to assess it. In photon radiation therapy, secondary photo-neutrons are especially produced above 10 MV acceleration voltage in the accelerator head, the collimator, or inside the patient's body. They are emitted isotropically with a fast neutron peak around 0.1 MeV to 1 MeV and a tail towards lower energies. (Kry et al., 2017)

In proton radiation therapy, the secondary radiation field consists of neutrons, scattered protons, light ions, photons and heavy recoil ions. In particular neutrons and scattered protons are accounted for the majority of the out of field dose (Kry et al., 2017; Stolarczyk et al., 2018). They are generated through nuclear interactions with the patient's body, the

gantry, or the radiation room itself. The neutron energy spectrum in proton radiation therapy is complex and difficult to assess. It very much depends on the relative position to the isocenter of the proton irradiation and the beam energy (Vedelago et al., 2022; Stolarczyk et al., 2018). Similar to cosmic neutrons, the secondary neutron energy spectrum in proton therapy can be divided into four regimes. The inter-nuclear cascade peak is usually found between several MeV up to the highest energy of the primary protons. These neutrons are the result of direct interactions of the primary protons with nucleons and are most prominently emitted in the forward direction (Shrestha et al., 2022). Secondly, an evaporation peak can be identified including fine structures in the order of 1 MeV up to 20 MeV which is the consequence of excited target nuclei emitting neutrons in order to reach the ground state. Its relative height to the cascade peak is influenced by the beamline geometry and the position in the patient or treatment room. Sometimes the two peaks overlap and cannot be differentiated (Vedelago et al., 2024). The third regime is dominated by the moderation of neutrons and extends between 10^{-7} MeV to 1 MeV. Below this energy, the thermal peak of the neutrons in thermal-equilibrium can be identified (Vedelago et al., 2024).

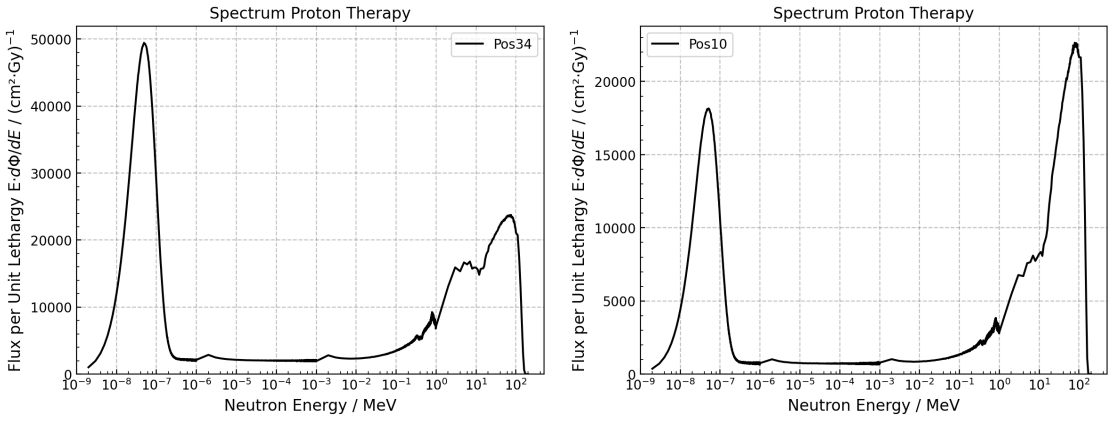

(a) (b)

Figure 2.5: Two examples for a secondary neutron spectrum in proton radiation therapy lateral to the beam at 5-10 cm distance in front of (a) and behind (b) the tumor volume. (Personal Communication Derksen, 2024)

In figure 2.5 two examples for a secondary neutron spectrum in proton radiation therapy lateral to the beam at 5-10 cm distance are presented. Figure 2.5a shows a position in front of the tumor volume with regard to the primary beam while figure 2.5b is located behind the tumor. Therefore, the effect of relative position to the primary beam on the relation of the evaporation to cascade peak can be well-identified.

2.3 Radiation Effects in Matter

The described radiation environments are very complex due to their composition of various particle types and energies. Each of them can cause different effects in matter which result in more or less severe effects in electronics.

In a general definition, radiation is the transport of energy through space. This can occur, e.g., in form of electromagnetic waves or particles like photons, electrons, or nucleons. While passing through matter, radiation interacts with atoms and consequently loses energy, changes direction, or is absorbed. If there is enough deposited energy in the matter, electrons can be knocked out of the atoms, ultimately ionizing them. Free charge carriers are generated in this process which is necessary to induce effects in electronics. Depending on the radiation type, different interactions and mechanisms are observed:

- **Ions:** When high energy ions interact with matter, they lose kinetic energy through electronic as well as nuclear interactions. Thus, a retarding force acts on the charged particles which is also known as stopping power. The electronic stopping power, i.e., the transfer of kinetic energy through elastic collisions with the bound electrons of the matter, is characterized as the linear energy transfer (LET). It describes the deposited energy per unit path length and is highly dependent on the energy and type of the impinging particle and the matter it passes through. In radiation effects testing, the LET is additionally divided by the material density to be independent of the physical state of the material, since the transferred energy is directly proportional to the density of the material (JEDEC, 2017). Hence, the LET is described as

$$LET = -\frac{1}{\rho}\frac{dE}{dx}. \tag{2.1}$$

The unit is defined as $\mathrm{MeV} \cdot \mathrm{cm}^2/\mathrm{mg}$. There is a fixed amount of energy which is required for the generation of an electron-hole pair in a material which is on average $3.6\,\mathrm{eV}$ for silicon. Thus, the deposited energy E can be translated to charge using a conversion factor of $22.5\,\mathrm{MeV/pC}$. The overall generated charge of one event results in

$$Q = \frac{E_{dep}}{22.5 MeV/pC}. \tag{2.2}$$

This generation of free charge carriers inside the material through the interaction with the ion finally leads to the effects which may result in the observed events in electronics. Therefore, the LET is a direct measure of the occurrence of effects in electronics after the hit of a particle (Baumann and Kruckmeyer, 2019). The total ionizing dose refers to the total energy which is deposited through ionization in a unit mass.

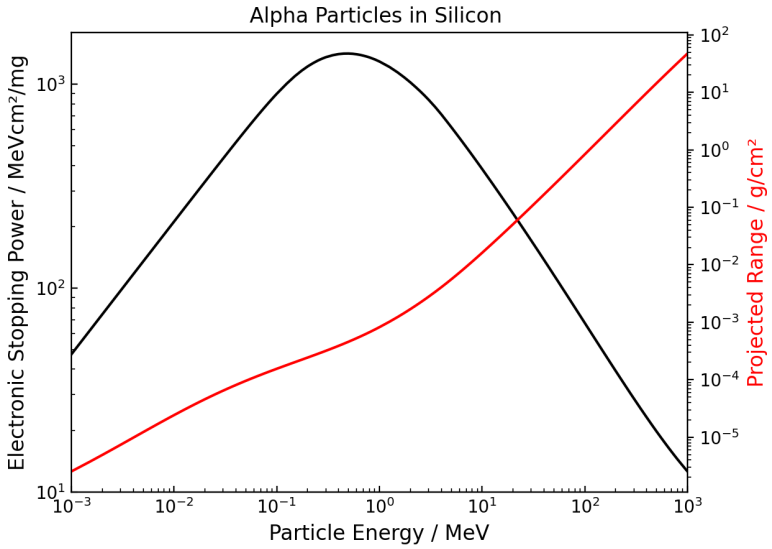

Figure 2.6: Stopping power and projected range of alpha particles in silicon. The data are extracted from NIST Standard Reference Database 124 (Berger et al., 1998).

The relation between LET and energy is described in an asymmetric function which is exemplarily shown for alpha particles in silicon in figure 2.6. The slower the ion, the higher its probability to interact with the matter along the path and the more charge carriers will be generated. Accordingly, the stopping power peaks immediately before the particle comes to rest which is also known as the Bragg Peak (Baumann and Kruckmeyer, 2019). That means, an ion traveling through matter loses kinetic energy through electronic interactions and therefore increases the LET along the path until it is completely stopped. This relationship between the average linear energy transfer and the travelled distance of the particle in the material is given in the Bragg curve (JEDEC, 2017). The projected range in silicon depending on the alpha particle's energy is additionally shown in figure 2.6. It describes the projected distance the particle travels in the material before it is completely stopped. It increases monotonically with ion energy.

The LET is statistical in nature. It can vary for the same particle species and depends on the path of the particle and the different interactions inside the material. Thus, only a mean value can be determined. The variation of range and LET from event to event is known as straggling (Baumann and Kruckmeyer, 2019).

- **Neutrons:** Neutrons have no charge, hence there is no Coulomb interaction possible between the particle and matter. Consequently, ionization is produced indirectly. In general, neutrons lose energy mostly through elastic and inelastic nuclear interactions. The occurring reaction is highly dependent on the energy of the neutron as

well as the properties of the target nucleus. In elastic scattering, a neutron collides with another nucleus and transfers some of its kinetic energy to the target which slows the primary neutron down. If the energy transfer is high enough to displace the target nucleus, this now recoiling nucleus becomes an ionizing particle itself. These recoil particles therefore generate charges and can ultimately influence the electronics.

In contrast, inelastic nuclear reactions refer to the absorption of a neutron by a target nucleus and its subsequent excitation. Depending on the primary energy of the neutron and the target nucleus, inelastic nuclear reactions finally result in the emission of gamma radiation, spallation processes, nuclear fission, or the emission of lighter fragments. Most of the secondary particles are directly ionizing and are one of the main causes for effects in electronics due to neutrons. (Baumann and Kruckmeyer, 2019)

The probability of occurrence for the different reactions is described in the nuclear cross section. Usually, it is defined as an area in the unit of barn (1 barn = $10^{-24}\,\mathrm{cm}^2$). The nuclear cross sections for the different reactions of a neutron at different energies with a Si-28 nucleus are illustrated in figure 2.7. Si-28 is the most abundant element in semiconductors. Additionally, Boron with its naturally occurring isotopes B-10 (19.9 %) and B-11 (80.1 %), is frequently used as a dopant or as insulating material (Baumann, 2005). However, only B-10 exhibits a high cross-section for reactions with neutrons and is therefore shown in figure 2.7a. The data were extracted from the ENDF VIII database (Brown et al., 2018).

As presented in 2.7a, thermal neutrons are distinctly more likely to interact with B-10 than with Si-28. B-10 has a high cross section for neutron capture and subsequent fission of the nucleus into Li-7 and an alpha particle which are highly ionizing and therefore affecting microelectronics.

In the high energy range shown in 2.7b, elastic scattering with Si-28 is the most probable reaction mechanism to occur up to 5 MeV. An estimation for the energy of the Silicon recoil is calculated using the classic elastic collision equation (Sierawski et al., 2010):

$$E_{recoil} = \frac{4mM}{(m+M)^2} E_n cos^2\theta \tag{2.3}$$

E_n and m are the respective energy and mass of the impinging neutron, θ stands for the scattering angle and M for the mass of the recoil particle. From the resulting E_{recoil}, the range of the recoil particle in the device can be derived.

Inelastic nuclear reaction are observed above a neutron energy of 5 MeV. Secondary heavy nuclei like Si, Mg, and Al as well as lighter particles like protons and alpha particles are produced which can directly induce charges in the sensitive volume

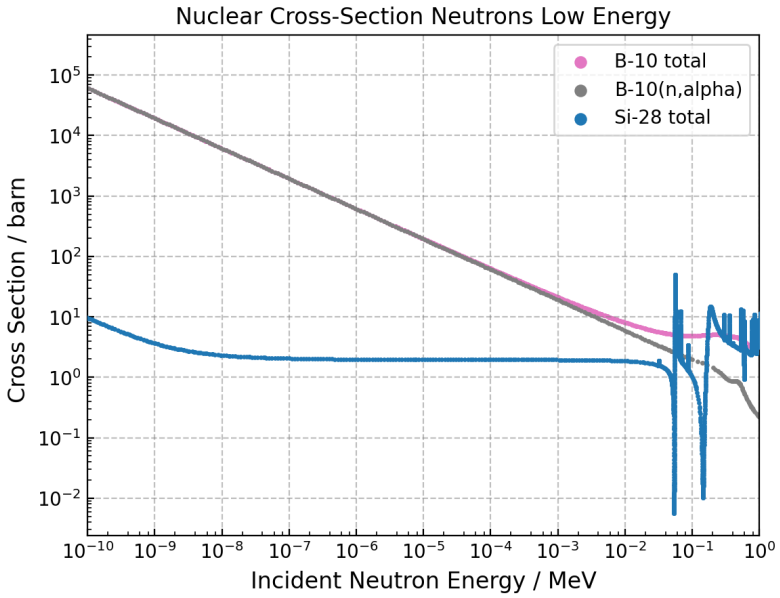

(a)

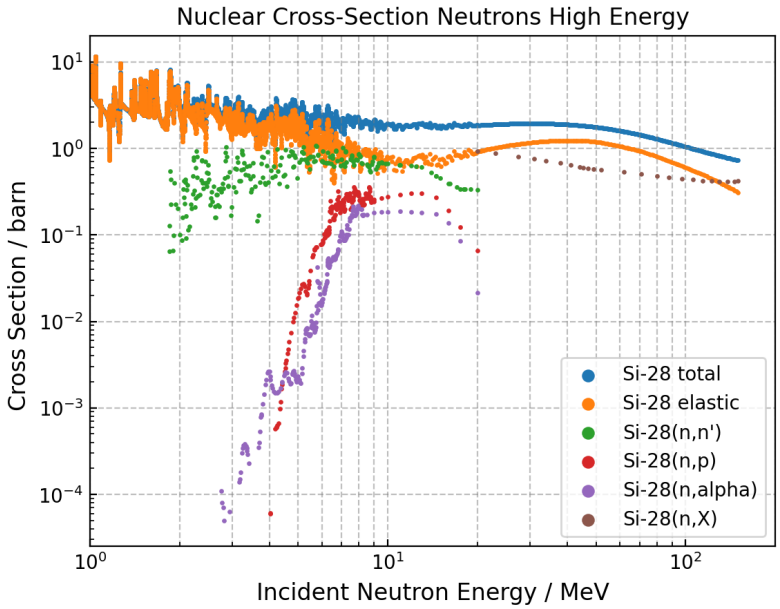

(b)

Figure 2.7: Nuclear cross section for the reaction of neutrons with Si-28 and B-10 at different energies. Data from ENDF VIII (Brown et al., 2018).

of the electrical device. For 14 MeV neutrons especially the Si-28(n,n')Si-28, Si-28(n,p)Al-28, and Si-28(n,α)Mg-25 reactions are relevant, besides the elastic reaction (Lucsányi et al., 2022). Above a neutron energy of 20 MeV other reaction channels increasingly contribute to the nuclear cross section while the probability of the previously described inelastic reactions decreases. Therefore, the production

of lighter nuclei like Na, Ne, O, and C becomes significant and the generation of heavier secondary particles decreases (Cecchetto, 2021).

- **Protons:** In contrast to neutrons, protons are charged and interact by the Coulomb force. Therefore, they are directly ionizing. However, above a particle energy of 50 MeV nuclear effects dominate the Coulomb effect. Thus, nuclear reactions similar to those observed with neutrons become relevant for protons. (Baumann and Kruckmeyer, 2019)

- **γ-Photons:** When high-energy gamma rays interact with matter, different effects can occur. Among other things, a photon can be absorbed by a nucleus leading to its excitation. Subsequently, the nucleus immediately decays with the emission of a subatomic particle. This process is called photodisintegration. It is especially relevant for the generation of neutrons in the accelerator head and beam collimator in photon radiation therapy above energies of 10 MeV. The photons interact with high Z-materials like tungsten or lead which have a higher cross-section for the (γ, n)-reaction compared to other materials in the linac. The threshold for photo neutron production is 6.74 MeV in tungsten and 6.19 MeV in lead, however, the highest probability of neutron production is in the range of 13 MeV to 18 MeV. (Naseri and Mesbahi, 2010)

There are many more particles and interactions with matter in radiation research. However, they are not primarily relevant for the effects of radiation on electronics and are therefore not further discussed.

2.3.1 Dose Quantities and Dosimeters

The amount of radiation absorbed in a material can be described in many different ways. In general, the absorbed dose is defined as the deposited energy per unit mass:

$$D = \frac{E}{m} \tag{2.4}$$

The unit is Gray [Gy]. The absorbed dose depends on the type and energy of the radiation and the material in which the energy is deposited. However, it does not consider any sensitivity of human tissue to radiation. In contrast, the equivalent dose H takes the biological effectiveness of the radiation into account. It is supposed to be a measure for stochastic effects of the radiation in tissue. For calculation, the absorbed dose D is weighted by a weighting factor W_R which is dependent on the radiation type (ICRP, 2007). Its distinct unit is Sievert [Sv]:

$$H = \sum_R W_R \cdot D_R \tag{2.5}$$

The dose can be measured with many different types of dosimeters. Among others, there are thermoluminescence dosimeters (TLDs) and bubble detectors which were used in this work for neutron dosimetry. TLDs are based on a thermoluminescent crystal such as lithium fluoride (LiF) which absorbs the ionizing radiation and traps some consequently excited electrons. When the crystal is heated after it was irradiated, it emits the trapped energy in the form of visible light. Therefore, the radiation dose is calculated according to the light that was emitted during heating (Pradhan, 1981). Dosimeters with different lithium enrichments are used for estimating the neutron dose. A TLD-600, enriched with Li-6, and a TLD-700, enriched with Li-7, are both irradiated. While the TLD-600 is sensitive to thermal neutrons and gamma radiation, the TLD-700 only records the gamma dose. With the dose difference of both dosimeters a thermal neutron dose can be estimated. (Gibson, 1986)

Bubble detectors consist of a superheated liquid which is dispersed in a clear and elastic polymer. Neutrons that pass the detector create visible bubbles due to cavitation in the superheated liquid which are then trapped in the gel. The number of bubbles can be directly converted to a tissue equivalent neutron dose. (Ing et al., 1997)

2.4 Radiation Effects in Electronics

In the terrestrial environment, radiation effects in electronics are most commonly caused by the effects of alpha particles from packaging materials, high energy cosmic neutrons, and thermal neutrons. While alpha particles cause direct effects in semiconductors, high energy neutrons need to generate secondary ionizing particles in the surrounding materials to disrupt microelectronics (Baumann, 2005). In general, effects from the total ionizing dose as well as from single particles can be observed. Especially, CMOS transistors of the Static Random Access Memory (SRAM) are particularly sensitive to radiation.

2.4.1 Total Ionizing Dose

Total ionizing dose (TID) effects are the result of long-term or high exposure to radiation, especially gamma-ray radiation. In general, transient charges from the interaction of the radiation with the semiconductor may be trapped in the insulators of the transistors. This can lead to shifts in the threshold voltage and subsequent increased leakage currents. Consequently, the power consumption of the device is increased and the reliability and its functionality might be compromised. (Baumann and Kruckmeyer, 2019)

2.4.2 Single Event Effects

Single event effects (SEE) are random and immediate disturbances of microelectronics caused by the interaction with a single particle. In contrast to TID, SEEs are not cumula-

tive. All SEEs can be derived from single event transients (SET) in the semiconducting elements of the circuits. Its mechanism is exemplarily shown in figure 2.8.

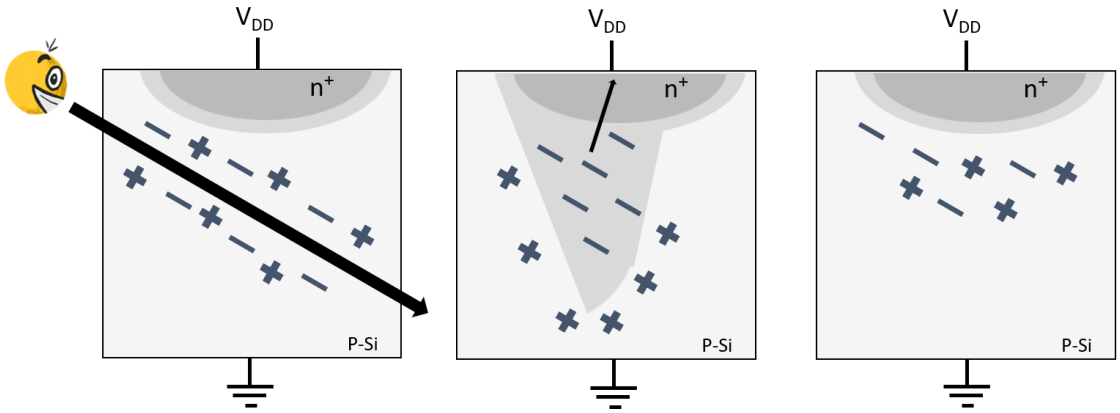

Figure 2.8: The generation of a single event effect in a semiconducting element is illustrated. A particle strikes a reversed biased junction and generates particles which are then collected by the applied electric field. Finally, all charge carriers have been collected, recombined or diffused to different areas. Adapted from Baumann and Kruckmeyer, 2019.

When an ionizing particle strikes a reverse-biased p-n junction, electron-hole pairs are generated in the cylindrical track (2.8a). Due to the electric field at the depleted region, the generated charge carriers are separated and cannot recombine immediately. In fact, a drift current is produced leading to a high current pulse at the node. The effect is enhanced when the charge carriers cause the depleted region to be deformed into a funnel shape, extending the electric field deeper into the substrate (2.8b). The volume where the charge carriers can be collected by the electrical field is referred to as the sensitive volume (SV). (Dodd and Massengill, 2003)

After the immediate phase, electrons can still diffuse into the depleted region and may be absorbed by the electrical field until all charge carriers have been collected, recombined, or diffused to different areas (2.8c) (Baumann and Kruckmeyer, 2019).

Depending on the response of the circuit to the transient charges, different effects like single event latch-ups (SEL), single event burnouts (SEB) or single event upsets (SEU) can occur. A latch-up event results in high currents in an integrated circuit due to parasitic bipolar effects in one of its transistors (the shortening of a transistor). When this effect occurs in a power MOSFET, it can result in a single event burnout (SEB). If the particle ultimately causes physical damage as seen in SELs and SEBs, the error is referred to as hard error, otherwise it is a soft error. (Baumann and Kruckmeyer, 2019) In particular relevant for the effects of cosmic radiation on AIMDs are single event upsets (SEU). It refers to a change of state in a node of a digital storage component like an SRAM due to the effects of a single particle. Consequently, this can lead to a conversion from a stored 1 to a 0 or vice versa, which is known as a bit flip.

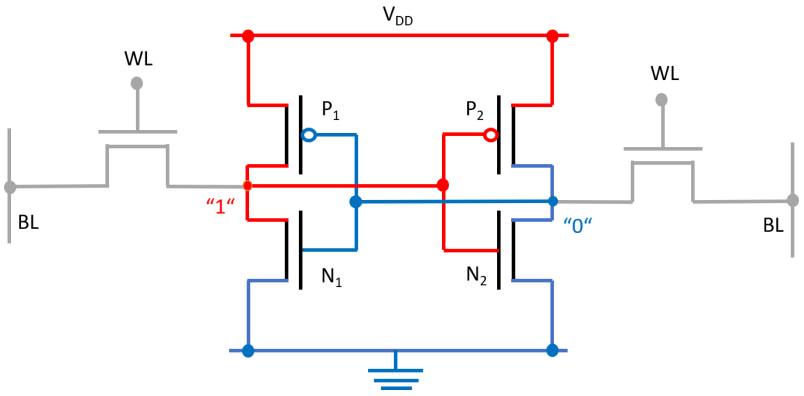

Figure 2.9: Schematic drawing of an SRAM cell. Red indicates high voltage equivalent to the ”1” state and blue areas show low voltage equivalent to the ”0” state. Adapted from Baumann and Kruckmeyer, 2019.

Typically, an SRAM cell consists of 6 transistors. A scheme of such a cell is depicted in figure 2.9. Two of them are pass transistors close to the bit lines (BL) and word lines (WL) and usually shut off during storage mode. They are only needed for the read and write operation. Furthermore, there are two P-type MOS transistors (P_1, P_2) and two N-type MOS transistors (N_1, N_2) which are required for the storing operation. The combination of the four transistors results in two cross-coupled inverters. During operation, one inverter influences the input of the other in a feedback loop. Therefore, a certain state can be maintained as long as power is applied. In the example shown in figure 2.9 P_1 is turned on resulting in a high potential (red) at the left storage node, indicated as a ”1”. Hence, the gates at P_2 and N_2 are also at high voltage leading to N_2 being turned on. This results in grounding the right storage node (blue), indicated as a ”0” and maintaining low voltage at the gate of P_1 which keeps it in an ON-state. Now, if a particle strikes the cell close to the reverse-biased drain junctions of an OFF transistors, for example N_1, electrons will be collected and the voltage at the left storage node will drop. Simultaneously, a current flow through the P_1 transistor begins for compensation. However, if the generated charge carriers exceed a certain critical charge Q_c the transistor cannot supply enough current to keep the voltage above a threshold and the cell will flip to the opposite state. (Baumann and Kruckmeyer, 2019; Dodd and Massengill, 2003)

Sometimes one particle can even strike multiple neighboring cells or produce fragments which travel to further distanced cells. Therefore, a single particle can cause multiple bits to flip at once. This is referred to as a multiple cell upset (MCU). If only a single cell is affected by a particle, this single event upset is called single bit upset (SBU). Built-in test mechanisms regularly check the memory with check sums for SBUs. If deviations occur, the device can perform a power-on-reset to correct the error. Thus, SEUs are soft errors and do not destroy the device. However, depending on the position of the changed bit, serious malfunctions of the entire device can still occur.

In general, the sensitivity of SRAMs to SEUs depends on multiple factors. The internal structure, dimensions, and materials in the device as well as the applied voltage affect, e.g., the critical charge. Furthermore, it has been demonstrated that an increase in voltage applied to the SRAM results in a corresponding rise in the critical charge required to induce a bit flip. Consequently, if the voltage is reduced, the sensitivity to SEUs of the memory device will increase (Clemente et al., 2018). Overall, an increasing susceptibility to SEUs with reduction in technology size is observed since the total capacitance of the device is decreased. (Dodd and Massengill, 2003; Kobayashi, 2021)

2.5 SEU Cross Section Functions

The sensitivity of electronics to bit flips caused by particle radiation is quantified by the cross section σ_{SEU}. In contrast to the nuclear cross section in section 2.3, it defines the probability that a single particle not only interacts with the matter but ultimately induces an SEE. It can be calculated using

$$\sigma_{SEU} = \frac{N_{SEU}}{\Phi}. \tag{2.6}$$

N_{SEU} stands for the observed number of bit flips and Φ is the overall fluence of the radiation the device was exposed to. The unit for the cross section is usually given with $cm^2/device$ or cm^2/bit, however it can also be specified with $\mu m^2/bit$ for, e.g., a direct assessment of the sensitive volume. The cross section and thus the observed number of bit flips is highly dependent on the particle species and energy of the radiation environment it is exposed to.

2.5.1 Heavy Ions

Heavy ions are generated as secondary particles, e.g., in inelastic neutron reactions, or are used for direct irradiation for testing a device. With different ion species and energies, different LET values can be obtained in the devices. In general, the higher the LET, the more charge carriers are generated when an ion passes through the sensitive volume. Hence, the probability of a single event upset increases. The dependence on the LET is characterized by a Weibull shaped function which is exemplarily shown in figure 2.10 and further described in section 4.2.1. There is a critical charge and hence a threshold LET_{th} which is required to induce an SEE. It can be deduced from the heavy ion response function. At high LETs, every ion traversing the sensitive volume of the circuit deposits enough charge to induce an SEU. Hence, the cross section saturates because it is limited by the surface area of the sensitive volume (Warren et al., 2005). At very high LETs, the sensitivity of the circuit to heavy ions is only influenced by the LET and does not depend on the primary energy of the ion (Warren et al., 2005).

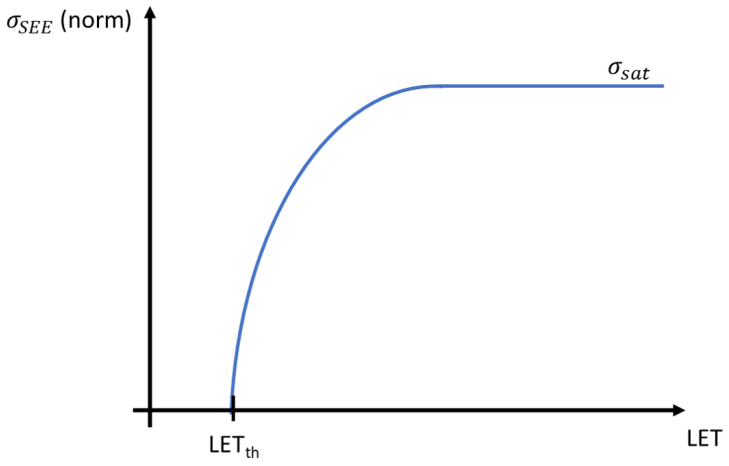

Figure 2.10: Schematic cross section curve for SEUs induced by heavy ions.

2.5.2 Neutrons

A schematic cross section curve for SEUs in an electronic device dependent on the energy of an impinging neutron is shown in figure 2.11 for reference (Cecchetto, 2021). It consists of a low-energy regime that is dominated by the neutron capture effects and a part where the various reaction channels of the high energy neutrons are considered. The transition between these two sections is characterized by a threshold energy E_{thresh}.

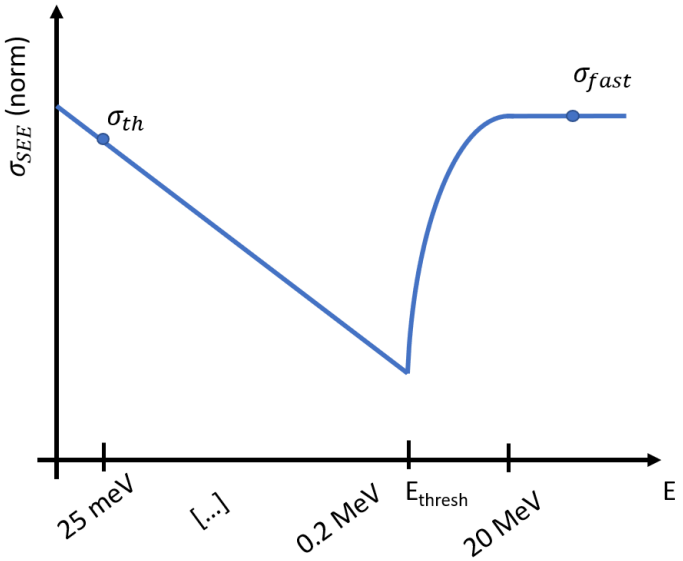

Figure 2.11: Schematic cross section curve for SEUs dependent on the neutron energy. It is divided into a thermal section and a high energy section, seperated by a threshold energy E_{thresh}. Adapted from (Cecchetto, 2021).

As described in section 2.3, the sensitivity of electronics to thermal neutrons mostly depends on the amount and location of B-10 inside the device. In the past, boron doped

phosphosilicate glass (BPSG) was used as a dielectric layer inside the semiconductor. Since then, multiple studies have found the BPSG as the primary cause for soft errors and recommended the elimination of this material (Baumann, 2005). Nowadays, boron is only used as a p-type dopant in the silicon (Auden et al., 2020). Referring to the nuclear cross section of the neutron interaction with boron (see fig. 2.7a), the effectiveness of inducing effects is much more likely in the thermal region than at higher energies. However, if boron is not abundant in the semiconductor, the probability of inducing an SEU due to a thermal neutron was found to be an order of magnitude lower than due to a high-energy neutron (Dyer and Lei, 2001). In general, it is assumed that the probability of effects due to neutrons of the low-energy regime decreases with $E^{-1/2}$ referring to the decrease of the neutron capture cross section.

A neutron energy threshold of $0.2\,\mathrm{MeV}$ has previously been assumed for the onset of effects by high-energy neutrons in microelectronics. This energy refers to the lowest onset energy of an inelastic reaction between neutrons and materials found in the structure of the electronics (Cecchetto et al., 2021). Above this threshold, up to $20\,\mathrm{MeV}$, the response of the electronics to neutrons is highly dependent on the particle's energy. As described in the nuclear cross section in figure 2.7b, various reaction channels with different generated secondary particles can be observed in this energy range. The probability of an SEU dependent on the neutron energy is described with a Weibull shaped function. This range of the spectrum is referred to as intermediate neutron energies.

Above a neutron energy of $20\,\mathrm{MeV}$, it is assumed that all hadrons, regardless of their energy, will cause similar effects and the SEU cross section curve will saturate. According to Cecchetto, this occurs due to the decrease of the cross section for inelastic nuclear reactions, the consequent reduced production of heavier ions, and the simultaneous strong production of light ions in (n,x)-reactions above $20\,\mathrm{MeV}$ (also refer to section 2.3) (Cecchetto, 2021).

2.6 Calculating the Single Event Rate in Mixed Radiation Environments

The energy dependent function for the cross section for SEUs ($\sigma(E)$), described in the previous section, needs to be measured or simulated when a device should be assessed for its radiation sensitivity in a certain radiation environment with mixed neutron energies. The actual process of radiation effects testing is further described and discussed in chapter 4. Subsequently, this function can be applied to a known neutron energy spectrum for the calculation of a single event rate (SER) in this radiation environment. For this purpose, $\sigma(E)$ is folded with the differential energy spectrum of interest.

Since it is often not possible to test devices for their SEU cross section in the full neutron energy range, the differential neutron flux in the specific radiation environment is

weighted according to the previously described observations of neutron effects in electronics. With this method, adopted from Røed et al. and Cecchetto et al., only cross sections for the effects of thermal and high energy neutrons need to be determined in the device under test (Røed et al., 2011; Cecchetto, 2021). An overview of the method is given in figure 2.12.

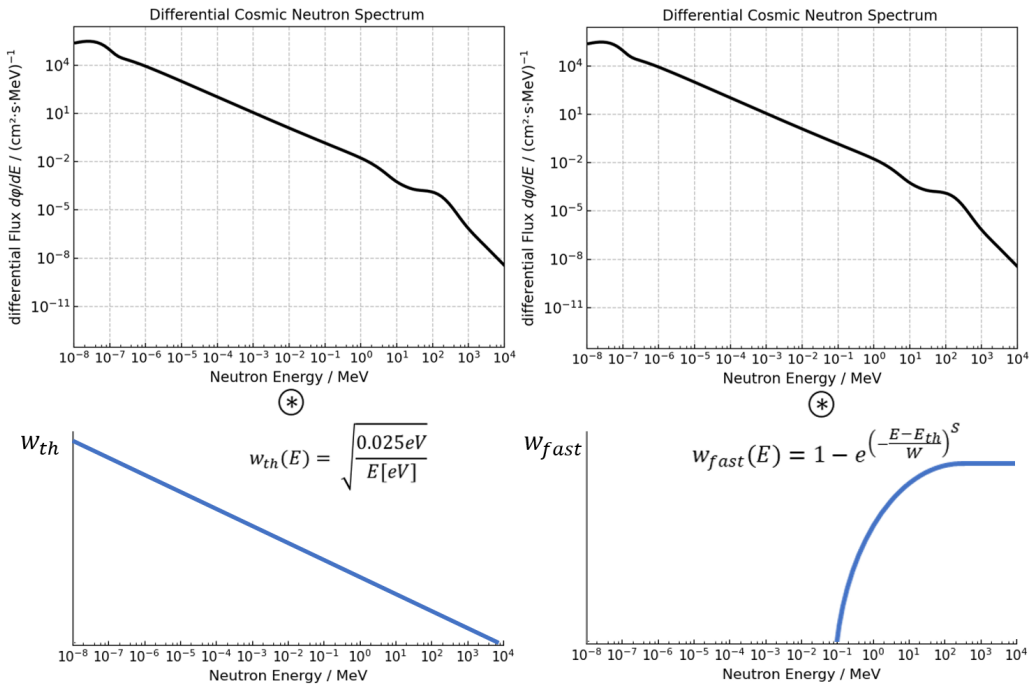

$$SER = \sigma_{th}\varphi_{th} + \sigma_{fast}(\varphi_{im} + \varphi_{he})$$

Figure 2.12: The Single Event Rate (SER) consists of a thermal equivalent and fast equivalent part. For the calculation, the differential neutron spectrum is folded with weighting functions for the calculation of a thermal equivalent flux and a high energy equivalent flux. The results are multiplied with the measured cross sections. The method was adopted from Røed et al., 2011 and Cecchetto, 2021.

In contrast to equation 2.6, the rate of expected events in a certain radiation environment is calculated using the neutron flux φ. The calculation is divided into a thermal equivalent part and a term which considers fast neutrons. It is a combination of the flux of intermediate neutrons φ_{im} between a threshold energy and 20 MeV and the high-energy neutron flux φ_{he} above 20 MeV:

$$SER = \sigma_{th}\varphi_{th} + \sigma_{fast}(\varphi_{im} + \varphi_{he}) \tag{2.7}$$

The equivalent flux for thermal neutrons and for the intermediate and high-energy neutrons is derived from the differential spectrum and weighted by the respective function.

For low energy neutrons the equivalent flux can therefore be written as:

$$\varphi_{th} = \int_0^{E_{thresh}} w_{th}(E) \frac{d\varphi}{dE} dE \tag{2.8}$$

As described above, the probability of thermal to low energy neutrons to interact with matter decreases with the inverse square root of the energy. Therefore, the thermal weighting function is defined as:

$$w_{th}(E) = \sqrt{\frac{0.025\,\text{eV}}{E[eV]}} \tag{2.9}$$

For intermediate neutrons above the threshold energy and below $20\,\text{MeV}$, the weighted flux is written as:

$$\varphi_{im} = \int_{E_{thresh}}^{20\,\text{MeV}} w_{im}(E) \frac{d\varphi}{dE} dE \tag{2.10}$$

The energy dependent weighting in this range is performed using a Weibull function:

$$w_{im}(E) = 1 - e^{\left(-\frac{E - E_{thresh}}{W}\right)^S} \tag{2.11}$$

The individual parameters and the energy threshold are determined with fully characterized SRAMs as reference devices (Røed et al., 2011; Cecchetto et al., 2021). Above a particle energy of $20\,\text{MeV}$ all hadrons are expected to cause similar effects. Hence, the flux for high-energy neutrons is weighted by a factor of 1 and is defined as:

$$\varphi_{he} = \int_{20\,\text{MeV}}^{E_{max}} \frac{d\varphi}{dE} dE \tag{2.12}$$

In a mixed radiation field, the weighted differential fluxes of different hadrons can be summed above $20\,\text{MeV}$. As a result, the expected rate of events in a mixed neutron radiation field with additional N hadrons above $20\,\text{MeV}$ is written as:

$$\begin{aligned} SER = {} & \sigma_{th} \int_0^{E_{thresh}} w_{th}(E) \frac{d\varphi}{dE} dE \\ & + \sigma_{fast} \left(\int_{E_{thresh}}^{20\,\text{MeV}} w_{im}(E) \frac{d\varphi}{dE} dE + \int_{20\,\text{MeV}}^{E_{max}} \frac{d\varphi}{dE} dE + \sum_{i=1}^{N} \int_{20\,\text{MeV}}^{E_{max}} \frac{d\varphi_i}{dE} dE \right) \end{aligned} \tag{2.13}$$

The integration of this rate over time allows for the calculation of the absolute number of expected events in a given radiation environment. In summary, when applying the presented method for the estimation of the SER in a certain radiation environment, only the parameters for w_{im} as well as the thermal and fast cross section for SEUs in the devices need to be determined.

3. Review of Radiation Effects in AIMDs

Single event effects in AIMDs result in the electrical reset of the devices forcing them into a safety or back-up mode to still provide basic therapeutic function. In 1998, Bradley and Normand reported the first extensive data set about effects of cosmic radiation on AIMDs and made predictions about failure rates (Bradley and Normand, 1998). Since then, multiple cases which occurred during air travel and radiation therapy have been reported. Furthermore, several studies were performed in order to investigate the effects of particle radiation on AIMDs. A review of the corresponding literature sums up the findings.

3.1 Literature Review of Case Reports

3.1.1 Clinical Reports of Malfunctions due to Environmental Radiation

There have been multiple reports on patients experiencing malfunctions of their devices due to environmental radiation. In 2008 Ferrick et al. reported three cases of patients with resets of their implanted cardioverter defibrillators (ICD) during flights. All other possible reasons for the malfunctions could be excluded, therefore, cosmic radiation was found to be the most likely cause. Two devices were found to be reprogrammed to increased right ventricular pacing which might be the reason for one patient experiencing mild symptoms. Furthermore, psychological side effects caused by the reset and consequent alarming of the device were observed in a third case. All three devices showed rudimentary function after the resets and still protected the patients against life-threatening conditions. Reprogramming to previous settings was successful in all devices. However, the authors suspected that electrical resets due to cosmic radiation could lead to more serious clinical consequences (Ferrick et al., 2008). Bhakta and Foreman commented on these case reports that further research on the susceptibility of CIEDs to cosmic radiation is needed and patients with ICDs may be advised before air travel, however they must be reassured that effects due to cosmic radiation are rare (Bhakta and Foreman, 2008).

Further cases were reported in the following years. Clair et al. describe a similar reset of a device during a flight. The patient did not show any physical symptoms, however, a loss of confidence in the implanted device was described (Clair et al., 2013). In contrast, in

an also air-travel related case reported by Paz et al. an ICD delivered four therapy shocks, although the heart did not exhibit a pathological rhythm. In a further interrogation, a memory error was found which was most likely triggered by cosmic radiation (Paz et al., 2017). Ferrick et al. concluded that the events might be rare but underreported if only their hospital already reported three cases in a period of two years (Ferrick et al., 2008).

Apart from aviation, a reset of a neurostimulator has been described and linked to possible effects of cosmic radiation (Dong et al., 2016). Resets without associated flights are mostly related to electromagnetic interferences or medical procedures involving radiation. However, Ajiro et al. described a power-on reset of a pacemaker without obvious cause. It can be speculated if cosmic particles on ground might be the cause of this event (Ajiro et al., 2017). Following their clinical investigations in 1998, Bradley and Normand reported 22 events caused by cosmic radiation from a total of 284 672 device days of 579 ICDs. This corresponds to a single event rate in one device of $(2.1 \pm 0.9) \cdot 10^{-2}\,\mathrm{year}^{-1}$ (Bradley and Normand, 1998). Furthermore, in the past 20 years, two manufacturers informed about resets due to cosmic radiation in one of their ICD models and recommended replacement. One manufacturer observed errors in 60 out of 36000 devices and described a rate of $2.57 \cdot 10^{-3}$ device errors in 5 years (BFArM, 2005). The second manufacturer informed that a patient had died after their subcutaneous ICD repeatedly applied an atypical amount of energy which prevented the device from detecting and treating an occurring arrhythmia. Further investigation revealed two bit flips in neighboring cells as cause for this severe malfunction. The manufacturer developed a software update to solve the problem (BFArM, 2017).

3.1.2 Reports in the MAUDE database

The Manufacturer and User Facility Device Experience (MAUDE) database of the US Food and Drug Administration (FDA) includes malfunction and adverse event reports for all medical products. In general, it is a tool for market surveillance and is supposed to promote transparency. (FDA, 2020)

A search of this database for the terms *bit flip* and *parity error* revealed a total of 1470 entries between 2010 and 2020. The majority of reported issues were related to CIEDs (1379 case reports). The remaining entries concerned neurostimulators and a few intrathecal pumps. Overall, symptoms were described by patients in 100 out of 1470 cases. Figure 3.1 presents the suspected causes of the events. Most of the resets were related to radiotherapy, followed by other radiation-based medical procedures. Some resets occurred before the devices were implanted so that they were no longer used. In total, there are 13 reports of cases attributable to aviation. However, the direct cause remains unknown in most cases or is not reported, as the actual reset event often occurred months ago and could no longer be reconstructed. Effects of cosmic radiation could be possible if all other causes like electromagnetic influences or battery depletion are ruled out.

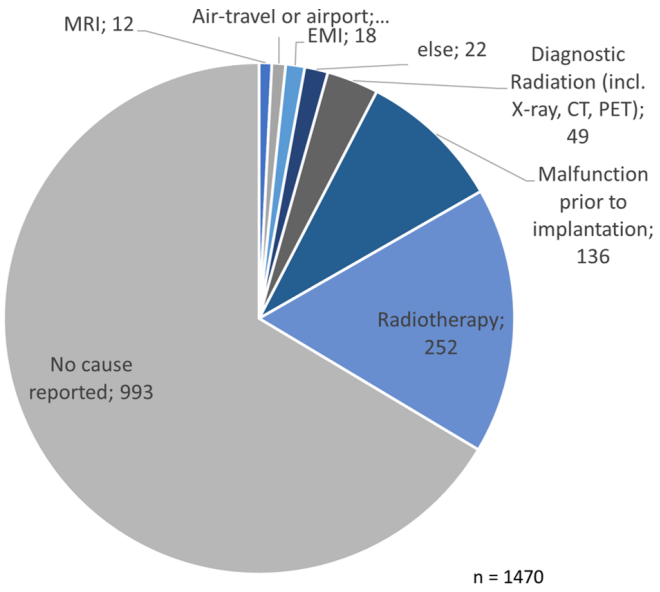

Figure 3.1: Pie chart of the assumed causes for bit flips or parity errors of AIMDs reported in the MAUDE database between 2010 and 2020 (FDA, 2020).

With respect to the absolute figures, it can be assumed that in many cases minor events such as temporary resets without severe effects are not reported. No event rates, frequency distributions, or temporal dependencies can therefore be determined from the MAUDE database. Similarly, specific manufacturers or devices cannot be compared with each other. Nevertheless, the reports give an initial impression of the quality of the events.

3.1.3 Clinical Reports from Radiation Therapy

Nearly 20 % of all cases of resets or devices found in back-up mode reported in the MAUDE database are related to radiation therapy. In addition, there are numerous publications describing cases of device errors in literature which are hereafter presented. Many studies analyzed the probable causes and influencing factors for resets in AIMDs to recommend guidelines for a safe treatment.

Photon Radiation Therapy

Patients experiencing irregularities with their AIMDs during photon radiation therapy is not a recent phenomenon. In 1982 Katzenberg et al. first reported on a failing pacemaker during radiation therapy with a linear accelerator which required immediate replacement. Subsequent analysis of the device revealed radiation-induced effects on the CMOS circuitry. The authors concluded that devices containing this then newly emerging technology may be more susceptible to radiation than previously observed (Katzenberg et al., 1982). Further cases of changed stimulation parameters after radiation therapy with linear

accelerators and a recommendation to avoid direct irradiation of the devices and moving them to a different site if needed as well as close monitoring of the patients were later given (Lee et al., 1986). Since then, numerous cases of patients experiencing irregularities with their pacemakers during radiation therapy even with life-threatening dysfunctions have been reported, e.g., but not exclusive Pourhamidi, 1983; Lewin et al., 1984; Zweng et al., 2008.

Although case reports involving pacemakers had been frequent, a patient with an ICD experiencing a device in back-up mode caused by scatter radiation during treatment was first reported in 2002 (Hoecht et al., 2002). Similarly, Thomas et al. found an electrical reset of an ICD in a patient during radiation therapy with the device being not directly in the treatment field (Thomas et al., 2004). A life-threatening dysfunction of an ICD due to effects of scattered radiation in the RAM of the device was reported by Nemec (Nemec, 2007).

A first case of the malfunction of an intrathecal infusion pump was documented in 2007 by Wu and Wang. After receiving 36 Gy using tomotherapy and 6 MV photons, the pump started alarming and could not be stopped. Later interrogation revealed complete battery depletion and damage to the electronic circuitries (Wu and Wang, 2007). However, further two studies including overall 127 patients undergoing radiation therapy between 2000 and 2019 found no effects on the pumps (Odell et al., 2021; Gebhardt et al., 2013).

In the past 15 years, there were several case reports showing that resets of CIEDs mostly occurred when the acceleration voltage was above 10 MV to 15 MV (Makkar et al., 2012; Elders et al., 2013; Gelblum and Amols, 2009; Soejima et al., 2011; Lau et al., 2008). At accelerating voltages above 10 MV neutrons can be generated by photodisintegration, especially in the collimator aperture. Hence, the effects seen in the CIEDs at these high energy irradiations were most likely the result of photo-neutrons (Elders et al., 2013). Another indication for effects caused by neutrons was already established in 1994. It was reported that a pacemaker-induced tachycardia was observed in a patient after high-energy neutron beam irradiation. The device was outside the treatment field and the estimated neutron dose was only 0.9 Gy. The detailed interrogation of the device showed considerable changes in the programming code (Raitt et al., 1994).

Grant et al. evaluated data from their radiation treatment center between 2005 and 2014 and found that device malfunctions occurred in approx. 7 % of all treatments (n = 259). All malfunctions were observed in neutron-producing radiotherapies. If only therapies with accelerator voltages of 15 MV to 18 MV were considered, malfunctions even occurred in 20 % of all irradiations (Grant et al., 2015). Since then, comparable findings have been described in several studies from different countries, e.g., Bagur et al., 2017; Riva et al., 2018; Yeung et al., 2019; Malavasi et al., 2020; Sharifzadehgan et al., 2020. In a multicenter analysis with a cohort of 560 patients, complications with devices

were reported in 3 % of all treatments (Zaremba et al., 2015). Finally, a meta-analysis of the data confirmed a higher risk of malfunctions with neutron-producing radiotherapies (Malavasi et al., 2023). The overall conclusion of the studies is that effects in radiation therapy are nowadays rare and associated with at most minor clinical events which are not life-threatening.

Proton and Carbon Radiation Therapy

Cases of changed pacing modes in pacemakers due to passive scattering proton beam radiation therapy were first described by Oshiro et al. in 2008. The devices did not receive any direct proton radiation. However, the authors concluded that a small dose of scattered neutrons could have induced the irregularities (Oshiro et al., 2008). Similarly, five cases of device resets without any adverse clinical effects in proton therapy likely due to scattered neutrons were reported by Gomez et al. The overall incidence of effects among all CIED patients treated with passive scattering therapy in the thoracic region was stated to be approximately 20 % (Gomez et al., 2013). Furthermore, CIED resets in 1 out of 4, 6 out of 47 patients, and 2 out 7 patients receiving passive scattered protons were identified by Yoshida et al., Hashimoto et al., and Ueyama et al., respectively. No adverse effects on the patients were reported (Hashimoto et al., 2022; Ueyama et al., 2016; Yoshida et al., 2023). Ueyama et al. concluded that the incidence of effects in proton radiation therapy might be higher than in photon radiation therapy and could not be predicted accurately. Hence, the analysis of the function of the device after every treatment session is advised (Ueyama et al., 2016). In contrast, Seidensaal et al. presented no irregularities in a cohort of 10 patients receiving active scanning proton beam therapy, concluding that this therapy method might be safer for CIED patients (Seidensaal et al., 2019). Interestingly, no resets were seen during carbon-ion radiation therapy, possibly due to fewer secondary neutrons and lower absorbed doses (Okano et al., 2021; Seidensaal et al., 2019; Hashimoto et al., 2022)

Management of CIED Patients in Radiation Therapy

Based on the clinical findings, the guidelines for radiation therapy in patients with CIEDs recommend to refrain from neutron-producing radiotherapy. Moreover, it is advised to completely evaluate the CIED at least before the first treatment and after completion to detect any irregularities in the device (Indik et al., 2017). Direct beam exposure should be avoided and device relocation considered if necessary (Gauter-Fleckenstein et al., 2015). It is heavily discussed if safe doses which are applied on the devices during therapy can be recommended. In principle, no correlation between failures and the irradiated dose has been established (Malavasi et al., 2023). However, the German guideline defines low risk for CIED failure below 2 Gy, intermediate risk between 2 Gy and 10 Gy

and high risk above 10 Gy. The American Association of Physicists in Medicine even defines the high-risk zone starting at 5 Gy (Miften et al., 2019). Accumulated doses above 2 Gy are always defined as high risks in patients who are pacemaker-dependent or have a history of ventricular tachyarrhythmias (Gauter-Fleckenstein et al., 2015). Measures corresponding to the risk assessment, e.g., weekly assessments of the CIED, or trained personal on stand-by to assist during device malfunction, should be applied during treatment (Gauter-Fleckenstein et al., 2015). Therefore, patient management during radiation therapy is highly personalized but sound scientific evidence for the prediction of device failure is still missing (Malavasi et al., 2023).

3.1.4 Conclusions from Case Reports

Only few reports in literature describe the malfunctions due to environmental radiation. Nevertheless, there are many uncertainties whether patients should be advised or not, e.g., when flying. The search of the MAUDE database describes many resets that have unexplained causes which could be indicative of effects due to cosmic radiation. Thus, a great underreporting of cases due to environmental radiation is assumed. In contrast, there have been many case reports about device malfunctions associated with radiation therapy. From the observations, it has been assumed that neutrons are the main cause for these effects. They can be produced with photon therapies above 10 MV or as scatter radiation during proton therapy.

It is important to distinguish between the stochastic effects which are caused by the secondary neutrons and are statistical in nature, and the deterministic effects which may be induced by the applied photon dose. The dose effects remain unclear, however, it cannot be ruled out that damage due to total dose effects could be observed. Nevertheless, when these effects are compared to those observed in other heavily exposed electronics, they would manifest in, e.g., a degradation of the device performance and functionality rather than as resets due to memory errors. In conclusion, the guidelines in place are vague and mostly based on expert opinions and previous observations. Hard scientific evidence for the prediction of device failure is missing. For more detailed information on, e.g., the influence of different neutron energies and to be able to make predictions, direct testing of devices needs to be performed.

3.2 Radiation Testing of AIMDs

Since there are numerous case reports on resets in AIMDs, especially in radiation therapy, many groups simulated radiation therapy plans with phantoms to assess the predictors of device errors. Many of the observed effects in patients could be reproduced and conclusions from the case reports were supported. However, few studies tested the effects in well-characterized radiation environments or directly with neutrons.

Radiation Testing Regulations for AIMDs

AIMDs are classified as type III medical devices which are subjected to strict regulations and require extensive tests for approval. According to major supervisory authorities, a risk management documentation is a requirement for all new products (EU, 2017). The standard ISO 14971:2019 defines the risk management process for medical devices. Manufacturers are obliged to present a risk management plan that includes the activities to identify, evaluate, and mitigate all risks, as well as criteria for determining acceptable risks (ISO, 2019b). Moreover, the ISO 14708 standard defines the test requirements for AIMDs. A detailed instruction for examining the effects of therapeutic radiation can be found in part 7 of the standard where additional requirements for cochlear and auditory brainstem implant system are defined. Accordingly, three devices placed in a water container shall be tested for effects of photon or electron irradiation with energies greater than 6 MeV. The samples are to be irradiated in fractions of 5 Gy until a cumulative dose of 100 Gy is reached. In between the fractions and at certain time points after irradiation, the output of the devices shall be characterized and any changes recorded. As a result, the manufacturer can provide information on the maximum dosage the device can be exposed to. (ISO, 2019a)

Furthermore, the accompanying documentation should include a warning, that therapeutic ionizing radiation could damage the electronics and that it might not be immediately detected (ISO, 2014). Apart from that, ionizing radiation is only considered when emitted by the device. All in all, the standard does not include any testing for single event effects (ISO, 2019a).

Photon Radiation Therapy

Detrimental effects of therapeutic radiation on the CMOS electronics of programmable cardiac pacemakers apart from electromagnetic interference were already suspected in 1982 and consequently investigated in more detail. Adamec et al. examined 25 pacemakers which were programmable and several older versions. It was found that 9 out of 13 programmable pacemakers based on CMOS technology failed after exposure while the older versions did not. As a result, it was recommended to avoid the exposure of direct pulsed radiation at therapeutic levels (Adamec et al., 1982). Any effects due to electromagnetic interferences could be excluded by Souliman and Christie (Souliman and Christie, 1994).

When Hoecht et al. described their first case report of a malfunction of an ICD during radiation therapy, they presented further in-vitro tests where they found another device in back-up mode. They concluded that his was likely caused by scatter radiation. In direct beam exposures, devices showed malfunctions only beyond 50 Gy photon dose (Hoecht et al., 2002). Similarly, Hurkmans et al. studied 19 devices at 6 MV using a phantom and

fractions of different doses. They observed that all but one of the devices showed regular function under 90 Gy. Beyond this dose 5 devices showed a premature Elective Replacement Indicator (ERI) (Hurkmans et al., 2005). Kapa et al. did not report any device reset in their 20 investigated devices at 6 MV with a cumulative dose of 4 Gy scatter radiation (Kapa et al., 2008). In contrast, Mouton et al. concluded from their study with 96 devices at 18 MV, using a polymer phantom that there was no safe dose threshold for radiation related effects. These findings are in line with previous conclusions that malfunctions are caused by secondary neutrons produced at photon energies above 10 MeV and that dose effects like premature battery depletion only occur at very high doses. Finally, Zaremba et al. compared the effects of photon therapy with 6 MV and 18 MV on 5 pacemakers and one ICD each from a different manufacturer. In total, they applied radiation with a cumulative dose of 150 Gy to the devices. Despite the high dose, no failures were reported in the 6 MV group, while electrical resets were observed in all pacemakers examined with 18 MV. In some cases, the preset parameters could be restored by reprogramming (Zaremba et al., 2014). Similar results were found in a simulated photon radiation treatment with 10 MV and 18 MV acceleration voltage in a water phantom and 8 ICDs. Neutron dosimetry was carried out, which showed that the dose of thermal and fast neutrons is 14 - 20 times higher at 18 MV than at 10 MV (Hashii et al., 2013). These studies thus confirm the clinical observations in radiotherapy. However, in 2021, Falco et al. reported one device reset in an experimental setting with all in all 140 devices irradiated at 6 MV (Falco et al., 2021). This indicates that although effects are reduced at this acceleration voltage they cannot be completely excluded.

Finally, there are indications that ICDs are more sensitive to radiation than pacemakers. Zecchin et al. found 6 out of 34 pacemakers and 13 out of 25 ICDs in back-up mode after irradiation with a phantom at 15 MV to simulate a treatment plan for prostatic cancer. This correlated with a greater but not significant neutron uptake through neutron capture reactions in ICDs than in pacemakers (Zecchin et al., 2016).

Proton Radiation Therapy

Oshiro et al. conducted a phantom test and examined the pacemaker for any adverse events, before a first patient with a CIED was treated at their proton radiation facility. Although no effects due to neutron scattering were observed, they later reported cases of resets during patient irradiation (refer to section 3.1.3) (Oshiro et al., 2008). The influence of secondary neutrons on CIEDs in proton radiation therapy was further tested by Hashimoto et al. They observed approximately one power-on-reset per 50 Gy applied proton radiation to the phantom (Hashimoto et al., 2012). Moreover, 62 devices were irradiated in a phantom study simulating a treatment with pencil beam proton radiation by Bjerre et al. They also concluded that the malfunctions are highly dependent on secondary neutron scatter (Bjerre et al., 2021).

Neutron Radiation Therapy

The effect of low-energy neutrons on pacemakers was investigated in a simulated boron neutron capture therapy (BNCT). Two different pacemakers were tested in a continuous spectrum primarily consisting of thermal and epithermal (< 9.12 keV) neutrons. The high-energy neutron flux was two orders of magnitude below the thermal and epithermal flux. The devices were irradiated for one hour resulting in a thermal and epithermal neutron fluence of about $10^{12}\ \mathrm{cm}^{-2}$ and about $10^{10}\ \mathrm{cm}^{-2}$ for high-energy neutrons. The total neutron dose at the location of the devices was estimated with $0.2\ \mathrm{Gy}$ and $0.1\ \mathrm{Gy}$, respectively. Both pacemakers subsequently showed serious malfunctions of the software and could not be read out. Furthermore, the devices were highly activated immediately after irradiation. They concluded that already comparatively low doses of neutrons can induce severe effects in pacemakers. (Koivunoro et al., 2011)

3.2.1 Calculating CIED Malfunctions

A first approach to predict malfunctions in CIEDs was already presented by Bradley and Normand. They directly characterized the integrated RAM with the theoretical Burst-Generation Method and the measurement of proton and neutron cross sections for device malfunctions. For the exposure to cosmic radiation on ground, they found single event rates for their chip between $0.01\ \mathrm{year}^{-1}$ and $0.02\ \mathrm{year}^{-1}$ which corresponds well to their observed field rate of $(2 \pm 8) \cdot 10^{-2}\ \mathrm{year}^{-1}$. (Bradley and Normand, 1998)

In addition, a total of 14 pacemakers from different manufacturers were examined with high-energy neutrons at a cyclotron facility by Trigano et al. The energy of the produced neutrons was between 3 MeV to 50 MeV with a mean energy of 20 MeV. Fluences between $10^{9}\ \mathrm{cm}^{-2}$ to $10^{10}\ \mathrm{cm}^{-2}$ were considered. After irradiation, 6 devices had performed an electrical reset but could subsequently be reprogrammed. Differences in the sensitivity of different manufacturers and models were observed. They did not notice any changes in the battery status. A failure threshold fluence based on these findings was defined and subsequently a SER in the atmospheric environment was calculated. The probability of device resets on ground after 5 years was estimated to be $6 \cdot 10^{-5}$ to $6 \cdot 10^{-4}$ for the respective fluence thresholds. (Trigano et al., 2012)

In the radiation therapy environment, Matsubara et al. found a correlation between a calculated neutron dose for prostate treatment at the device and CIED malfunction and concluded that the risk of failure is proportional to the received neutron dose (Matsubara et al., 2020). Furthermore, they did not find any correlation between accumulated and scattered photon dose with the number of malfunctions. Nevertheless, they discussed that neutron fluence is not a good predictor for CIED malfunctions since the neutron energy spectrum in radiation therapy is not monoenergetic. In contrast to the calculation of a neutron equivalent dose, it is not accounted for any energy dependence of the interaction

probability of neutrons when only considering the neutron fluence. Reanalyzing data from Hashimoto et al., they predicted the number of malfunctions for prostate treatment for photon, proton, and carbon-ion therapy which was in good agreement with previously measured values (Matsubara et al., 2020).

3.3 Method for Determining the Reset Rate in AIMDs

After reviewing the scientific literature on radiation effects in AIMDs, it is clear that few studies have investigated the sensitivity of CIEDs in primary radiation tests that are not designed to simulate radiation therapy. However, most of these studies only describe qualitatively factors that influence device sensitivity. Thus, vague predictions of device failures can be made exclusively for specific therapy scenarios. As a result, few data are available for predicting radiation induced malfunctions in CIEDs in other radiation environments. However, patients are constantly exposed to cosmic radiation at ground levels and even more at aviation altitudes when they fly. It is also important to consider extreme space weather events on ground levels as well as at aviation altitudes.

For the development of a method to calculate reset rates in AIMDs in various radiation environments, it was assumed that the observed reset events were a direct consequence of SEUs in the memory of a device. Therefore, the most accurate methodology would have been to directly test the chips that were implemented in the CIEDs to assess their sensitivity to particle radiation. However, information on the exact specification of the chips was not available and the CIEDs had to be analyzed at system level. Optimally, testing at multiple monoenergetic neutron energies should be performed to assess the energy dependent function for the cross section for SEUs. This was not feasible due to constraints in beam time and the number of available devices for testing.

Consequently, the method for calculating a single event rate in mixed radiation environments based on weighted differential energy spectra described in section 2.6 was adapted to AIMDs. In contrast to Matsubara et al., this method accounts for the different probabilities of interaction for neutrons in the device at different energies using the neutron flux. Hence, the calculation of the reset rate can be performed without the use of dose quantities which rely on material specific conversion factors.

According to the presented test method, a thermal and high-energy cross section for resets in AIMDs were to be determined. Furthermore, basic SRAMs as reference devices were to be characterized for their sensitivity to neutrons to define the Weibull weighting function for the high-energy equivalent flux and an energy threshold. In order to assess these parameters, standards established in radiation effects testing were applied.

4. Radiation Effect Testing for SEE

Radiation effects testing encompasses a multitude of methods which are for the most part designed for space applications. Full assessment of the radiation sensitivity of AIMDs requires the determination of an SEU cross section function $\sigma(E)$ of basic SRAMs. Therefore, different methods for experimental device testing of SRAM chips with hadrons and the simulation of the neutron cross section for single event effects (SEE) using parameters assessed with heavy ion testing are presented.

It was not possible to directly read out the memories of medical devices which is a prerequisite for accurate detection of SEEs. Only effects on the device level were observable. Therefore, it could only be distinguished between working and malfunctioning devices in a group of irradiated samples. Consequently, an alternative method using a reliability analysis had to be developed for the determination of the thermal and high-energy neutron cross section of AIMDs. Thus, chapter 4 and 5 focus on the radiation effects testing of SRAMs. The analysis of medical devices is then described in chapter 6.

4.1 Preparation of Radiation Effect Testing

For the various radiation environments, different standards for radiation effect testing have been established for electronic components such as SRAMs. In general, SEE testing is performed at particle accelerators. For the analysis of the ground-level or avionic environment, heavy ions, neutrons, or protons are used. The neutron cross section is energy dependent, thus, the particle species and energy for irradiation need to be selected carefully. Ultimately, with the known particle fluence and the absolute number of observed effects, a cross section can be derived.

Multiple factors can influence the single event rate (SER) in SRAMs which need to be considered when planning experimental testing of integrated circuits. Environmental conditions such as temperature as well as device specific parameters like supply voltage and operational frequency can affect the probability of effects (Kramer et al., 2011). According to the standards, these parameters should be cautiously selected, monitored, and documented (JEDEC, 2021). Since in some devices, the probability of a $1 \rightarrow 0$ directed bit flip is different from $0 \rightarrow 1$, the test pattern needs to be tested and selected carefully

(JEDEC, 2021). It can be chosen between, e.g., only ones, only zeros, or a checkerboard with alternating ones and zeros in bits and addresses. Finally, there can be effects due to the read and write mode set on the device during testing. In a static test, a specific bit pattern is written to the device prior to testing. During irradiation the device is set to stand-by mode and is not read out until the beam is turned off again. While static testing can withstand high fluxes without reasonable dead times, it does not provide temporal information that is important for the analysis of multiple bit flips. In contrast, temporal resolution can be achieved with dynamic testing. In this condition, the device is subjected to continuous read out and flipped bits are constantly corrected during irradiation. However, a high rate of bit flips can be problematic due to long dead times. (JEDEC, 2021)

4.2 Experimental Methods

4.2.1 Heavy Ion Testing

The sole purpose of heavy ion (Z>1) testing in the presented work was the estimation of the specific sensitive volume (further shown in figure 4.1) and the critical charge in the SRAM. Subsequently, these parameters were included in models for the simulation of the SER in various radiation environments (e.g., CREME96 or G4SEE) (Baumann and Kruckmeyer, 2019). In general, the aim of heavy ion testing is the determination of LET dependent cross section values for SEEs. They are then fitted to a Weibull curve. The corresponding equation is shown in eq. 4.1.

$$\sigma(LET) = \sigma_{sat} \cdot \left[1 - e^{-\left(\frac{LET - LET_{th}}{W}\right)^{s}}\right] \text{ for } LET > LET_{th} \tag{4.1}$$

σ_{sat} represents the saturated cross section which may be used for an estimation of the sensitive area of the device as described in section 2.5. If the saturation is not reached, it is likely caused by the occurrence of multiple bit flips due to a single impinging particle (Multiple Cell Upset) (ESA, 2014). LET_{th} is the threshold LET for the onset of effects, W denotes the width of the distribution and s is the shape parameter (Baumann and Kruckmeyer, 2019). In specific cases, when the device should be exposed to a known heavy ion environment, e.g., in space, $\sigma(LET)$ can be directly used for the estimation of a single event rate. (JEDEC, 2017)

Testing is performed at particle accelerators. The device under test (DUT) is placed into an ion beam with known energy and flux. The beam usually consists of only one ion species and atomic number and should have a range in silicon of at least 40 μm (ESA, 2014). The device is monitored and its response compared to the pre-irradiation status. Any altered bits are counted and a cross section can be calculated. According to the JESD57a standard, for good statistics, testing is performed until 100 events or a fluence

of $1 \cdot 10^{-7}\ \mathrm{cm}^{-2}$ is reached with a flux ranging between $10^{3}\ \mathrm{cm}^{-2}\mathrm{s}^{-1}$ to $10^{5}\ \mathrm{cm}^{-2}\mathrm{s}^{-1}$. (JEDEC, 2017)

Some ions at standard test facilities might have a range that is not sufficient to traverse the packaging of the DUT to reach the sensitive volume. Therefore, during device preparation the DUT should be delidded to expose the die directly. Since this is a complex and costly process, testing at higher ion energies can be used as an alternative (Alía et al., 2019).

For the determination of the LET dependent cross section, it is crucial to identify the expected LET of the test ion at the edge of the sensitive volume. In general, the LET is measured for a 0° incident angle on the die (perpendicular to the target). By changing the angle between the beam and the target, the distance the beam travels inside the sensitive volume is increased. Therefore, an effective LET can be defined as

$$LET_{eff} = \frac{LET}{cos(\alpha)}. \tag{4.2}$$

Hence, the number of tested LET values can be increased without changing the beam energy or particle type in an extensive process. Apart from the LET, the effective fluence on the chip changes with the incident angle. Consequently, the cross section for measurements at a certain angle is now written as

$$\sigma_{eff} = \frac{N_{SEE}}{\Phi \cdot cos(\alpha)}. \tag{4.3}$$

When considering LET_{eff}, it is crucial to know the architecture of the DUT. If the lateral dimension of the sensitive volume is much smaller than the depth, one ion at an angle could induce more than one upset leading to an overestimation of the probability of the effect (Baumann and Kruckmeyer, 2019).

Definition of Sensitive Volume and Critical Charge

When assuming that the sensitive volume is shaped as a rectangular parallelepiped as shown in figure 4.1, the saturated cross section is equal to the sensitive area of the chip, since every ion traversing the sensitive volume deposits enough charge to induce an SEU. The side lengths are therefore calculated with $l_{SA} = \sqrt{\sigma_{sat}}$. The critical charge as the collected charge up to the threshold for switching the circuit (Dodd and Sexton, 1995), is more difficult to determine due to the dependency on many different factors like supply voltage, temperature, and structure of the CMOS. Since it is a direct input parameter to the simulation of the SEU sensitivity, it is crucial to estimate the critical charge as accurately as possible. Multiple methods based on a combination of simulations and the result of heavy ion measurements have been established to quantify the critical charge.

Already in 1982 Pickel proposed a scaling trend of the critical charge by the technology size l with $Q_c = 0.85(l/4)^{1.5}$ (Pickel, 1982). This trend was found to be in good

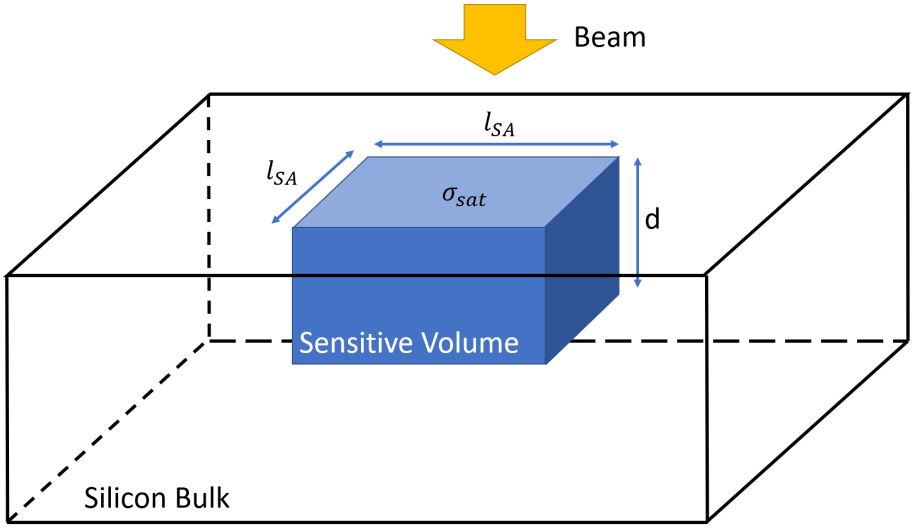

Figure 4.1: Exemplary Sensitive Volume for Single Event Effects.

agreement with experimental data (Kobayashi, 2021). Hence, the critical charge may be roughly estimated with the known technology size. In a more adaptive attempt, the current pulse propagation in the SRAM circuit is simulated after a particle hits the sensitive volume. However, detailed information about the circuit structure is necessary for an accurate determination (Dodd and Sexton, 1995).

In this work, the LET threshold obtained during heavy ion testing is used for the estimation of the critical charge. It is therefore written as (Petersen et al., 1993)

$$Q_{crit} = \frac{LET_{th} \cdot \rho \cdot e \cdot d}{X}. \tag{4.4}$$

In this equation ρ denotes the material density (for silicon $2.32\,\mathrm{g/cm^3}$), e the electron charge, X the average energy needed to create an electron-hole pair (3.6 eV for silicon) and d the depth of the sensitive volume. Determining this thickness is another not trivial task and different methods have been proposed to estimate this parameter. According to Petersen et al., it can be calculated using the depletion depth and the funnel length (Petersen et al., 1993; Kobayashi, 2021). Coronetti et al. used simulations and proton direct ionization measurements to determine the thickness of the sensitive volume (Coronetti et al., 2021). In some cases, the sensitive volume is simply defined as a cube. Thus, the thickness of the sensitive volume would equal the side length of the sensitive area. In summary, previous works assumed sensitive depths between $0.25\,\mu\mathrm{m}$ and $2\,\mu\mathrm{m}$ for the calculation of the critical charge (Alía et al., 2017; Coronetti et al., 2021; Sierawski et al., 2011; Petersen et al., 1993).

4.2.2 Testing for Neutron Radiation Environments

There are multiple standards which define the requirements for testing integrated circuits for their soft error rate (SER) in neutron radiation environments. While the JEDEC JESD89B standard is used for electronics in ground level environments (JEDEC, 2021), the IEC 62396-1 and IEC 62396-2 specify testing for avionics (IEC, 2016; IEC, 2017).

The JEDEC JESD89B standard suggests multiple approaches for the estimation of the SER. Accordingly, the most straightforward method for investigating the effect is real-time testing in an atmospheric environment. This is done by exposing a large number of DUTs to natural cosmic radiation until a sufficient number of events to estimate the SER have occurred. Since this may take months to years, accelerated testing of the atmospheric environment is generally preferred. In this case, a spallation source with a broad neutron spectrum similar to that of a terrestrial neutron environment is used. For the evaluation of the SER at ground level, only one campaign of comparable short duration is needed. However, it is neither possible to extract a soft error cross section nor to investigate the different contributions of neutron energies separately. In any case, the results can only be transferred to spectra that are similar to the tested spectrum. In contrast, energy dependent cross sections for SEEs in the full spectrum can be determined at quasi-monoenergetic sources. These neutron beams are characterized by a peak energy and a significant fraction of lower energy neutrons in a tail. The difficulty in this type of testing is to separate the effects of the peak energy neutrons form those of the tail. Thus, complex unfolding methods must be applied to estimate the contribution of both energy regimes. (JEDEC, 2021)

Testing with multiple truly monoenergetic neutron and proton sources overcomes many of the challenges presented previously. Although many different sources and some extrapolations are still required for a complete characterization, this test method ultimately allows for the calculation of the SER in any high energy neutron environment. (Cecchetto et al., 2019) Therefore, monoenergetic testing was primarily used in this work. For the consequent estimation of the energy dependent cross-section $\sigma(E)$, the standard suggests to test at least four energies and to fit the results to a four parameter Weibull equation (JEDEC, 2021):

$$\sigma(E) = \sigma_{sat} \cdot \left[1 - e^{-\left(\frac{E-E_{thresh}}{W}\right)^{s}}\right] \text{ for } E > E_{thresh} \tag{4.5}$$

The four parameters to be determined are σ_{sat} which is the asymptotic neutron or proton cross section, E_{thresh} which represents the threshold energy below which the cross section for SEEs due to high-energy neutrons is zero, as well as the width factor W and shape factor s of the curve. Energies between 1 MeV and 14 MeV, 50 MeV and 60 MeV, 90 MeV and 100 MeV and values above 200 MeV should be considered for testing (JEDEC, 2021). Monoenergetic neutrons between 1 MeV and 14 MeV are generated

from Deuterium-Tritium (DT) or Deuterium-Deuterium (DD) reactions. Above 50 MeV, testing is performed with monoenergetic protons (Baumann and Kruckmeyer, 2019).

In general, it is assumed in the standard that only neutron energies above 10 MeV are relevant for inducing SEEs. It is well-known that the onset of effects in several devices is below this assumed energy, especially in devices with a technology below 65 nm (Cecchetto et al., 2021). In fact, most of the devices show great variation of the cross section until a saturation is reached, in most cases below 50 MeV. However, the full influence of neutron energies between 1 MeV and 10 MeV in comparison with the full spectrum remains uncertain (Quinn et al., 2019). Therefore, the standard recommends testing at an additional monoenergetic energy below 10 MeV to accurately obtain a value for the varying cross section in this energy range (JEDEC, 2021). Subsequently, the fitted energy-dependent cross section curve can be folded with a known differential neutron flux for predicting a single event rate in this specific radiation environment. In the presented work, $\sigma(E)$ is applied as the SEU cross section function between E_{th} and 20 MeV for the weighting of the differential spectrum of a mixed radiation environment as presented in section 2.5 (Røed et al., 2011; Cecchetto et al., 2021).

Finally, for a comprehensive understanding of the device sensitivity to soft errors in the full range of the neutron energy spectrum, the response to thermal neutrons must be tested as an additional energy. This can be done at nuclear reactors or at particle accelerators using moderators.

In any case, full spectrum monoenergetic neutron testing for the prediction of the SER is extensive. For this reason, the standards further suggest a simplified approach for the estimation of SEUs in atmospheric environments. Either the cross section from testing with a white neutron spectrum or the highest tested monoenergetic proton energy can be multiplied with a reference neutron flux for ground-level or aviation altitudes (IEC, 2016; JEDEC, 2021). Normand and Dominik showed that even testing with 14 MeV monoenergetic neutrons can be sufficiently accurate to predict the occurrence of SEUs in the terrestrial environment for unhardened devices (Normand and Dominik, 2010). Even though this approach could underestimate the MCU response of devices (Clemens et al., 2011), Cecchetto et al. surmised that 14 MeV neutrons can be used to approximate the SEU rate of high-energy neutrons in modern technologies (Cecchetto et al., 2021).

For ground applications, the JEDEC JESD89B standard provides for geomagnetic shielding corresponding to the location of New York City, outdoors at sea level, in a mid-level solar activity an integrated neutron flux above 10 MeV of $3.596 \cdot 10^{-3}\,\mathrm{cm^{-2}s^{-1}}$. According to the IEC standard, the Boeing model is used for a reference flux in avionic applications. It considers an integrated neutron flux above 10 MeV for 12 km altitude and 45° geographic latitude at the longitude of New York City of $5600\,\mathrm{cm^{-2}h^{-1}}$. In order to account for the effect of protons at aviation altitudes, this flux is rounded up to $6000\,\mathrm{cm^{-2}h^{-1}}$. For technologies below 150 nm, neutrons with energies between 1 MeV

and 10 MeV should be considered. Therefore, the reference flux increases to $9200\ \mathrm{cm^{-2}h^{-1}}$. (IEC, 2016)

4.3 Simulation of Radiation Effects in Electronics

Since experimental device testing is a very extensive and costly process, the simulation of radiation effects in electronics was thoroughly studied in the past. For precise calculations of the SER, three different aspects need to be considered. First, the particle spectrum of the radiation environment itself must be characterized. Nowadays, there are many tools for precise calculations of, e.g., the cosmic spectrum in space and in the atmosphere, the radiation environment at particle accelerators, or in medical facilities. Secondly, the transport of the particles of the primary spectrum through matter and the generation of secondaries must be addressed. Usually, simulation tools like Geant4, FLUKA, or MCNP are used for these calculations. Finally, the processes leading to the generation of SEEs and precise thresholds for the occurrence of effects inside the electrical devices must be modeled and defined.

Up until now, numerous methods, analytical and based on Monte Carlo simulations, have been established to predict the rate of single event effects in terrestrial and space applications. Above all, the analytical rectangular parallelepiped (RPP) model has long been used for calculations of the SER. It assumes that the sensitive volume of a device is shaped as a rectangular parallelepiped. All effects are determined solely by the total energy deposition of the impinging particle within the sensitive volume. Consequently, the deposited energy is a product of the path length and the LET which is assumed to be constant and dependent only on the particle type and energy. Ultimately, if the deposited energy exceeds the critical energy of the device, an effect will occur. (Weller et al., 2009) However, there is evidence that this simplified method underestimates the SER in certain technologies and radiation environments (Reed et al., 2007). Thus, physical modeling has been introduced to accurately predict SEEs. It refines the determination of the deposited energy by using Monte Carlo simulations and therefore includes the contribution of secondary particles, nuclear reactions, and scattering events inside the sensitive volume. In addition, more complex methods can be applied to connect the deposited energy with the response of the circuit. (Weller et al., 2009)

Monte Carlo (MC) methods are nowadays widely used for the SER prediction. Using event-by-event scoring, the energy deposition distribution can be precisely determined inside the sensitive volume which in many cases is still rectangularly shaped. However, more complex shapes and even nested sensitive volumes are possible with MC-methods. All information which is required for further SEE simulations and effect discrimination can be extracted from the simulated energy deposition. Moreover, many different particles and their effects can easily be assessed. (Lucsányi et al., 2022)

In recent years, many different MC-tools have been established by different groups for SER prediction, e.g., MRED, TIARA, or MUSCA SEP (Reed et al., 2013). However, most of them are not publicly available or lack of a reasonable simulation of neutrons, in particular below an energy of 20 MeV. Furthermore, information on the exact structure of the chips is required for an accurate simulation of the effects. If details cannot be obtained due to proprietary reasons, experimental methods like heavy-ion testing can be used to determine, e.g., the sensitive volume or the critical charge.

4.3.1 G4SEE

In 2022, the G4SEE toolkit for the simulation of single event effects was released in the scope of the CERN R2E project (Lucsányi et al., 2022). Besides the simulation of effects of, e.g., heavy-ions and low energy protons in electronic devices, it especially focuses on intermediate neutrons in the energy range of 0.1 MeV to 20 MeV. They are particularly relevant in atmospheric and medical radiation environments. Validation was performed with monoenergetic neutrons between 1.2 MeV and 17 MeV (Lucsányi et al., 2022). G4SEE is free and available open source for the radiation effects community and was used for the simulation of SEEs in SRAM chips in this work.

The code is based on the Geant4-toolkit which uses MC-methods for the interactions of particles in matter for radiation transport (Agostinelli et al., 2003; Allison et al., 2006; Allison et al., 2016). Initially, Geant4 was developed by a collaboration in high-energy physics to support the simulation of detectors. Nowadays, it is widely applied in space sciences, medicine, and nuclear and accelerator physics. In the radiation effects community, it is particularly relevant for the computation of SEEs. The toolkit consists of C++ class libraries for describing the detector geometry, creating the particles and tracking their interaction with matter. Finally, everything is combined in one executable C++ program. In the G4SEE toolkit, Python 3 scripts are employed for pre- and postprocessing for the support of the main particle transport simulation.

For the application of G4SEE, the dimensions of the sensitive volume and the critical charge are required as input parameters which were assessed in heavy ion testing. The target geometry consists of a bulk volume containing a sensitive volume in the form of a rectangular parallelepiped or cylinder. Optional Back-End-Of-Line (BEOL) layers can be added on top. Any particles, with arbitrary energies, beam shapes, and angular distributions can be generated. The physics list for the definition of processes can be adapted independently by the user. Furthermore, there is an option for physics-based microscopic cross section biasing to reduce computation time. The simulation scores the results of the computation in histogram files which are then used to calculate the reverse cumulative sum of the deposited energy. Finally, the SEE cross section as a function of critical charge is obtained. (Lucsányi et al., 2022)

4.4 Facilities for SEE testing

Radiation effects testing for SEE was carried out at various facilities across Europe. Multiple SRAMs as well as AIMDs were investigated. An overview of the experiments, particles, and energies is given in table 4.1.

Table 4.1: Facilities where radiation effects testing for SEE was performed.

Facility	Location	Particles	Energy	Experiment
GANIL	Caen (F)	C-12 Fe-56	95 MeV/u 65 MeV/u	SRAM chips
Am-Be	Giessen (D)	Neutron spectrum	0.1-11 MeV	SRAM chips
FNG	Frascati (IT)	Monoenergetic neutrons	14 MeV	SRAM chips, CIEDs
MIT	Marburg (D)	Protons	50-220 MeV	SRAM chips, Intrathecal Pumps
EMMA	Didcot (UK)	Thermal neutrons	25 meV	SRAM chips, CIEDs

4.4.1 GANIL

The Grand Accélérateur National d'Ions Lourdes (GANIL) in Caen, France uses a cyclotron to accelerate various ions from carbon to uranium. It can provide maximum energies of 95 MeV/u for light ions and 24 MeV/u for heavier particles. The facility serves many different research areas from space radiation biology studies to fundamental science experiments in nuclear physics. Only a single ion energy is available during a test campaign. Therefore, degraders are used to vary the kinetic energy of the ion and thus the LET on the target. (Durantel et al., 2016)

The experiment was performed at the radiobiology beam line called IRRABAT in the D1 cave. A focused beam of 13 mm × 13 mm size was used and swept horizontally and vertically to cover a maximum irradiation field of 60 mm × 60 mm. Sweeping is performed horizontally at a frequency of 425.8 Hz and vertically at 4.4 Hz. The flux is monitored using a calibrated X-ray monitoring system and can be set between $4 \cdot 10^4$ $\mathrm{cm}^{-2}\mathrm{s}^{-1}$ and $2 \cdot 10^6$ $\mathrm{cm}^{-2}\mathrm{s}^{-1}$. (Durantel et al., 2016) The device is placed in a sample holder which can be moved automatically to the irradiation position.

The test campaigns with SRAM chips were performed using C-12 ions with a primary energy of 95 MeV/u in March 2022 and Fe-56 with a primary energy of 65 MeV/u in April 2023. For comprehensive heavy ion testing, measurements at multiple LETs were required. A degrader made of polymethylmethacrylate (PMMA) was used for the carbon

Figure 4.2: Photograph of the beam line and set up of SRAMs for testing at GANIL.

ions and the device was irradiated at different angles with iron ions. Since the chips were not delidded, the ions lost energy in the packaging material. Consequently, the LET was simulated at the edge of the sensitive volume of the SRAMs. The beam line and a set up for the SRAMs for testing at different angles is shown in figure 4.2.

Simulation of the LET

A first evaluation of the LET of the C-12 ions using SRIM (Ziegler et al., 2010) revealed strongly varying values close to the Bragg peak. Thus, Geant4 (Version: Geant4-11.0.4) was used for a more exact determination of the LET in the SRAM chip. The simulation and the corresponding physics lists are based on the *hadr02* example of Geant4. The detector construction was created according to the description of the beam line by Boissonnat et al. which is shown in figure 4.3 (Boissonnat et al., 2017).

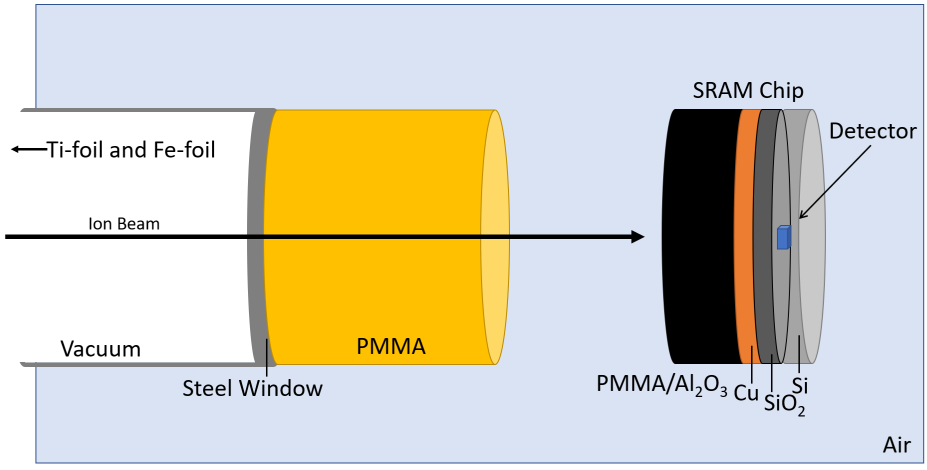

Figure 4.3: Used Geometry for the Simulation of LET at GANIL.

After generation, the simulated particles cross a 2 µm titanium foil for averaging and

widening the beam that is located 8.7 m in front of the 25 µm steel foil which separates the vacuum from the experimental hall. Additionally, the particles cross a 5.77 µm iron foil at 20 cm distance to the steel foil which is used for the X-ray monitoring system. The chips are placed at a distance of 14 cm from the extraction window in air. Only for the C-12 irradiation, additional PMMA degraders of various thicknesses were used directly behind the window. The chips are simulated with a 500 µm layer for the packaging material (67 % Al_2O_3 and 33 % PMMA) (further described in section 5.1.2), and two 4.5 µm layers made of Cu and SiO_2. The sensitive volume made of silicon is located directly behind. The deposited energy as well as the energy of the primary particles is scored in a 1 um thick silicon volume at the edge of the sensitive volume. For reasonable statistics, the simulation for C-12 included 10^5 starts. For Fe-56, 10^4 ions were simulated.

Before calculating the LET in the actual chips, the simulation was validated against the simulated and measured values by Boissonnat, Fontbonne, Balanzat, Boumard, Carniol, Cassimi, Colin, Cussol, Etasse, Fontbonne, Frelin, Hommet, and Salvador (2017). In this case the PMMA degrader was 16.9 mm and the chips were replaced by a polystyrene cell culture flask filled with Geant4 soft tissue material *G4_TISSUE_SOFT_ICRP*. Table 4.2 shows the simulated energy deposition in the tissue and primary energy of C-12 compared to the results of Boissonnat et al. The mean value from the calculated histogram as well as its standard deviation are specified.

Table 4.2: Comparison of the LET simulation with values measured by Boissonnat et al., 2017.

	Simulation	**Boissonat et al.**
Energy Deposition	$(84 \pm 24)\,\mathrm{keV/\mu m}$	$(73.4 \pm 1.1)\,\mathrm{keV/\mu m}$
Energy C-12	$(27.0 \pm 0.5)\,\mathrm{MeV/n}$	$25.7\,\mathrm{MeV/n}$

Within the standard deviation of the energy deposition histogram, the simulation is comparable with the measured values. Hence, the actual experiment set up for the carbon irradiation was simulated in order to define the LET. The resulting distribution of the deposited energy for the 17.9 mm degrader is depicted in figure 4.4a. The error bars are given as $\sqrt{n}$ of the counts in a bin. The histogram was fitted with a Gaussian distribution to gain a mean value and a standard deviation for the deposited energy. As a result, a density-corrected LET of $(0.60 \pm 0.12)\,\mathrm{MeVcm^2/mg}$ in the sensitive volume was calculated for the irradiation of the SRAM with C-12 and the 17.9 mm degrader.

In addition, a 19.8 mm thick PMMA degrader was simulated for carbon ions. It resulted in an asymmetric and spread distribution of the energy deposition, depicted in figure 4.4b. When increasing the thickness of the PMMA degrader to 20.0 mm, no energy deposition was scored. Considering the uncertainties of the positioning of the chips, the assumed layer thicknesses and the degrader itself, it can be concluded that the carbon ions

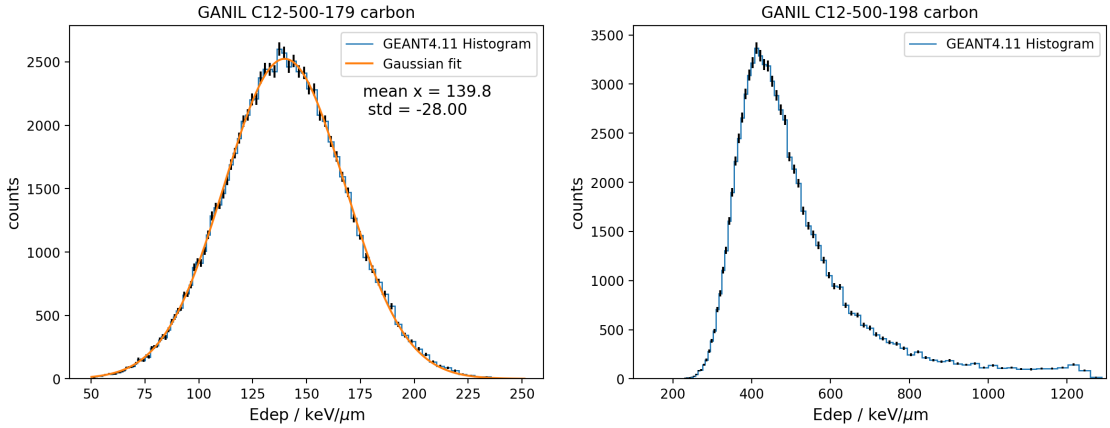

(a) 17.9 mm Degrader

(b) 19.8 mm Degrader

Figure 4.4: Simulation of the energy deposition of the C-12 ions in the sensitive volume. For the determination of the mean and the standard deviation the simulated values are fitted with a Gaussian distribution.

are stopped in the sensitive volume. Thus, no distinct LET value could be specified for an experiment performed with the 19.8 mm degrader.

In a second simulation, the energy deposition of the iron ions was simulated. The range of the tested iron ions is much shorter than that of carbon ions. For LET variation, the chips were irradiated at four different angles (0°, 40°, 50°, and 60°). Thus, the length of passage through the package material and BEOL layers is also increased by a factor $1/cos(\alpha)$. The results of the simulation which represent the distribution of energy deposition of the iron ions in the sensitive volume are shown in figure 4.5. The errors are given with $\sqrt{n}$ for the respective bin. For the calculation of a mean and a standard deviation the simulated values are fitted to a Gaussian distribution.

The values for the first three angles have little variation within the standard deviation. Thus, a constant LET can be assumed for these angles. However, the simulation at 60° shows a considerable increase in the mean deposited energies. This indicates that the iron ion might be close to its maximum range due to the longer passage through the package material at this angle. Table 4.3 summarizes the resulting density-corrected effective LETs for the four angles. It considers the longer path in the sensitive volume through the irradiation at an angle and therefore higher energy deposition with the factor $1/cos(\alpha)$.

4.4.2 Americium-Beryllium Neutron Source

Several radiation effects test of SRAMs were performed at an Americium-Beryllium (Am-Be) neutron source. The devices were tested at several distances to the source as well as behind paraffin and borosilicate glass moderators. Therefore, it was important to assess the neutron energy spectrum at the different measurement positions through simulations

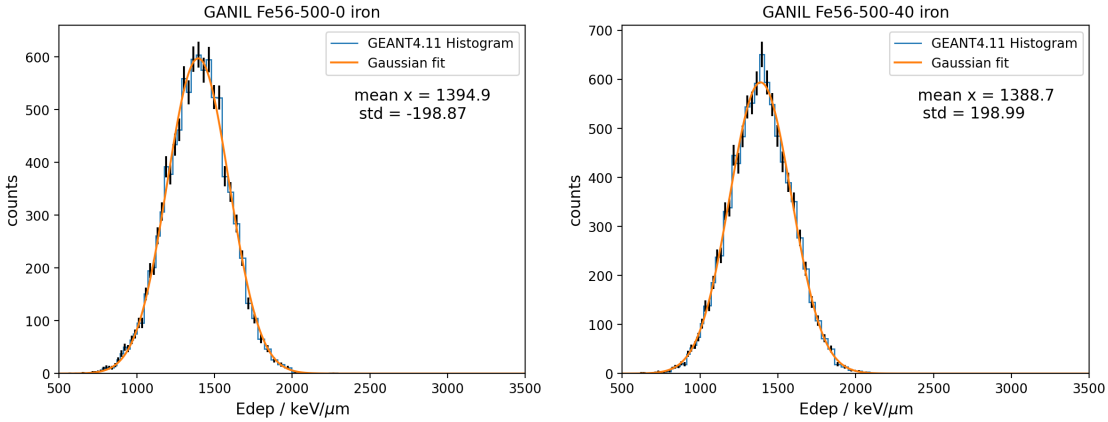

(a) 0°

(b) 40°

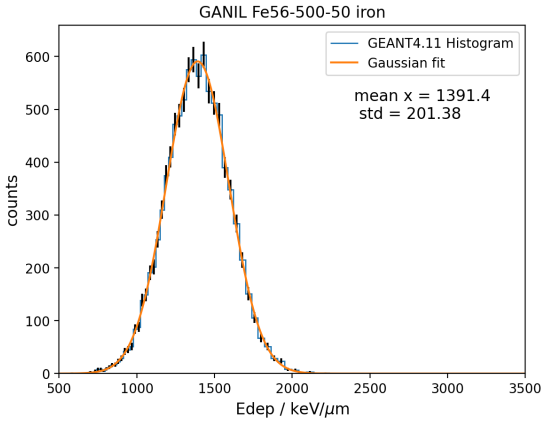

(c) 50°

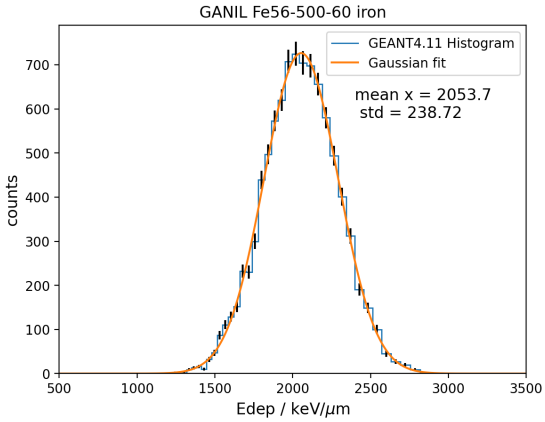

(d) 60°

Figure 4.5: Simulation of the energy deposition of the Fe-56 ions at different angles. For the determination of the mean energy deposition and the standard deviation the simulated values are fitted to a Gaussian distribution.

Table 4.3: Effective LET values for Fe-56 at different angles based on the simulation.

Angle / deg	$LET_{eff}/MeVcm^2/mg$
0	6.0 ± 0.8
40	7.8 ± 1.1
50	9.3 ± 1.3
60	17.6 ± 2.1

and validate them through measurements. Am-Be is a well-known and well-characterized neutron-emitting source. It usually consists of a mixture of powdered americium oxide with beryllium metal which is compressed into a welded steel cylinder. Am-241 decays

into Np-237 and is therefore a strong alpha emitter with a mean energy of 5.486 MeV:

$$^{241}_{94}\mathrm{Am} \longrightarrow {}^{237}_{92}\mathrm{Np} + {}^{4}_{2}\mathrm{He} \tag{4.6}$$

Beryllium on the other hand can interact with an alpha particle to C-12 resulting in the emission of a neutron:

$$^{4}_{2}\mathrm{He} + {}^{9}_{4}\mathrm{Be} \longrightarrow {}^{1}_{0}\mathrm{n} + {}^{12}_{6}\mathrm{C} \tag{4.7}$$

The resulting neutron spectrum is continuous with a maximum energy of about 11 MeV. The produced flux is highly stable and is used, e.g., for source calibration. However, the neutron emission strongly depends on the ratio of americium oxide and beryllium in the source (Didi et al., 2017).

The Am-Be source used for the measurements is located at the Gießener Strahlenzentrum in Gießen and had an activity of $2.22 \cdot 10^{11}$ Bq on 31.12.2013. The Am-Be powder mixture is assumed to be contained in a X.14 welded-steel capsule (assumable Eckert & Ziegler Nuclitec GmbH, Germany) and enclosed in lead. The weight of the full container is 1606 g. A scheme of the source is shown in 4.6. The source is situated in a 30 cm long glass cylinder beneath the platform and shielded with paraffin blocks.

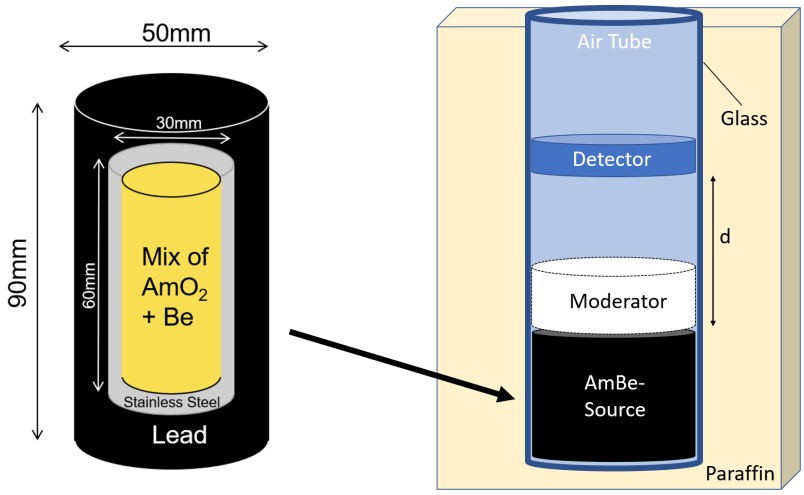

Figure 4.6: Assumed metrics of the Am-Be neutron source inside the lead enclosure and geometry of the set-up for the simulation.

According to the data sheet of a X.14 source, the neutron emission rate is $1.3{\cdot}10^{7}\ \mathrm{cm}^{-2}\mathrm{s}^{-1}$ (Eckert & Ziegler Nuclitec GmbH, 2009). However, the exact neutron flux, especially at the point of irradiation, is not known. For this reason, simulations were performed to estimate a neutron flux and spectrum for the different measurement positions.

Simulation of the Am-Be Neutron Source Flux

The simulation of the Am-Be source was performed in Geant4 (Version: Geant4-11.0.4) and is based on the Geant4 *neutronsource* example. The particle generation begins with the decay of a randomly placed Am-241 ion inside the cylindrical source volume consisting of a mixture of beryllium, oxygen and air. As described above, the mixture of AmO_2 and Be is crucial for the neutron yield. Therefore, the composition of the source volume (91 % Air, 4.5 %AmO_2, 4.5 % Be) was chosen to obtain the neutron emission rate described in the data sheet. According to the datasheet of the X.14 source, it is enclosed by a 2.4 mm layer of stainless-steel (composition: 74 % Fe, 18 % Cr, 8 % Ni). Since the exact thickness of the lead encapsulation was not known, it was estimated from the weight of the container and was assumed with 10 mm. As seen in figure 4.6, the lead-mantled source is located in an air-filled glass tube of 5 mm thickness and 60 mm diameter. The detector area with a diameter of 60 mm is placed at a variable distance d to the top of the source. Only when a neutron hits this area, it is scored with its respective energy. The space between detector and source can be filled with air or a moderator material like paraffin or borosilicate glass. The world volume outside of the glass tube is defined as paraffin.

The simulated energy spectrum of the neutron source at 1 mm distance is depicted in figure 4.7. It was simulated with $1 \cdot 10^9$ decays of an Am-241 and subsequently extrapolated to the assumed activity of the investigated source. It has a mean energy

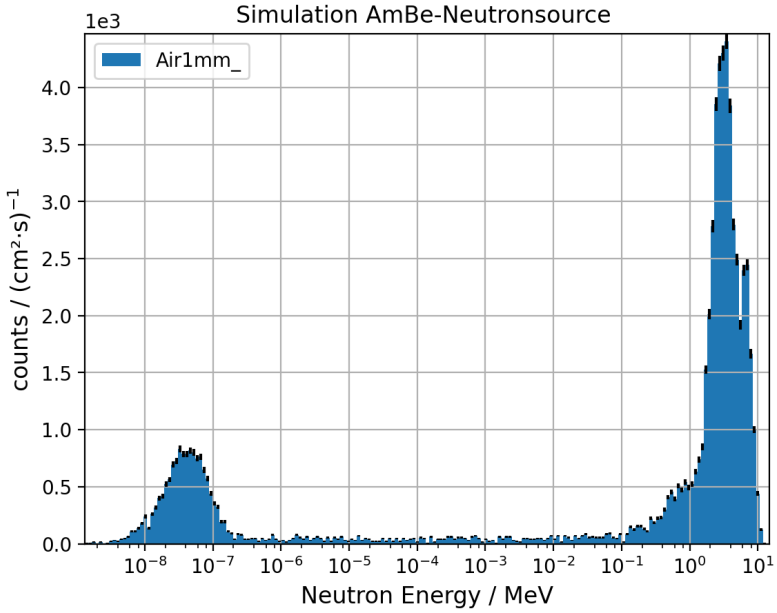

Figure 4.7: Result of the simulation of the Am-Be neutron Spectrum at 1 mm distance above the source.

of (2.55 ± 0.03) MeV and shows a thermal and fast neutron peak. The uncertainty of

each bar is given with $\sqrt{n}$. The cumulative flux is estimated with $6.9 \cdot 10^5\,\mathrm{cm}^{-2}\mathrm{s}^{-1}$. Thereof, $5.0 \cdot 10^5\,\mathrm{cm}^{-2}\mathrm{s}^{-1}$ is accounted for by the fast neutron flux above 0.1 MeV and $1.4 \cdot 10^5\,\mathrm{cm}^{-2}\mathrm{s}^{-1}$ by the thermal neutron flux below 0.5 eV. The simulation was repeated for different distances from the source. The spectral flux, as well as the dose in tissue and the equivalent dose, were calculated at each point using dose conversion factors (Personal Communication Matthiä, 2024). Several measurements at various distances from the source were subsequently performed for validating the simulation. Therefore, only the specific energy ranges corresponding to the sensitivity ranges of the dosimeters were considered for the dose calculations. The results are presented in figure 4.8.

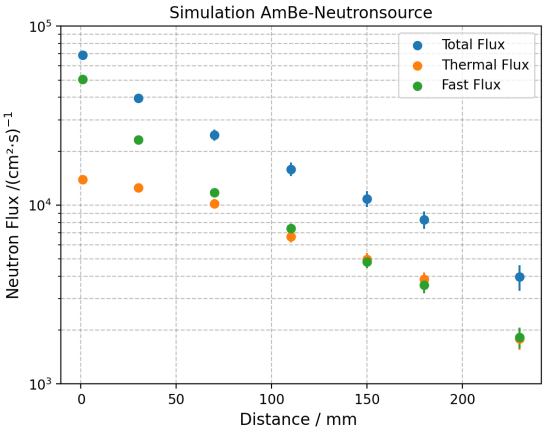

(a) Thermal, fast and total neutron flux.

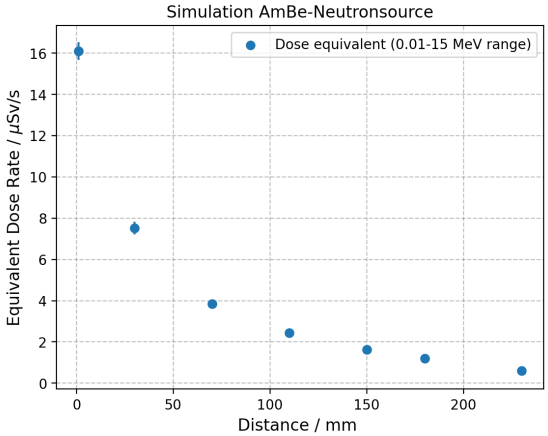

(b) Dose equivalent corresponding to the energy range of bubble detectors.

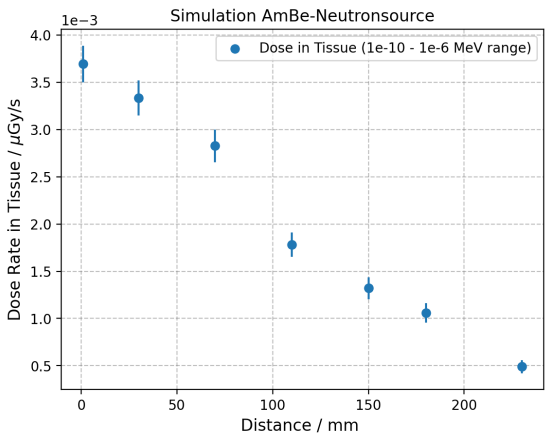

(c) Dose in tissue, corresponding to the energy range of TLDs

Figure 4.8: Simulation of flux and dose per distance in air of the Am-Be neutron source for comparison with measurements.

As expected, a reduction of the flux and dose with increasing distance is observed in all curves. The uncertainty is increasing towards greater distances due to the decrease of scored particles. Regarding the flux in figure 4.8a it can be seen, that for distances

below 60 mm the fraction of fast neutrons in the total flux is much higher than that of thermal neutrons. Beyond this distance, the fast and thermal neutron fluxes become equal. At 150 mm a neutron flux of $(2.14 \pm 0.71)\,\mathrm{cm^{-2}s^{-1}}$ was previously estimated with a diode (personal communication Zaunick, 2022). Thus, the flux is underestimated by the simulation of a factor of 2.

The calculated equivalent dose shown in figure 4.8b was further investigated at 230 mm. Two bubble detectors (Bubble Technology Industries, Canada) with a sensitivity of $1.3\ \frac{\mathrm{bub}}{\mu\mathrm{Sv}}$ in a range of 0.01 MeV to 15 MeV were used. The devices were exposed to the neutron source for 30 s. Subsequently, the emerged bubbles were counted and the equivalent dose was calculated to be (39 ± 7) µSv at this distance. The simulation estimated the equivalent dose with (18 ± 3) and therefore underestimates the measured value by a factor of 2.

Finally, the dose in tissue depicted in figure 4.8c was assessed with thermoluminescence dosimeters (TLD). For the calculation of the dose, only neutrons below $1 \cdot 10^{-6}$ MeV were included. The dosimeters were irradiated for 45 min at 30 mm distance. Besides the measurement without a moderator, the TLDs were exposed behind a 6 mm borosilicate glass plate at the same distance for the same amount of time. The plate was used to absorb the thermal component of the total neutron flux due to its boron content. Since no calibration of the TLDs and thus an exact determination of the neutron dose was available, only the ratio of the dose with and without borosilicate glass could be obtained. A ratio of (3.0 ± 0.6) was calculated which includes a statistical and systematic measurement uncertainty of 20 %. The simulation resulted in a ratio of (4.9 ± 0.6). A summary of the measurements and the corresponding simulated values is given in table 4.4.

Table 4.4: Comparison of the calculated values for dose and flux at the neutron source with values from measurements.

	Distance / mm	**Simulation**	**Measurement**
Flux / $cm^{-2}s^{-1}$	150	$(1.1 \pm 0.1) \cdot 10^4$	$(2.14 \pm 0.71) \cdot 10^4$
Equivalent dose /μSv	230	18 ± 3	39 ± 7
Ratio Thermal Neutron Dose Air / Borosilicate Glass	30	4.9 ± 0.6	3.0 ± 0.6

There are several confounding factors to explain the considerable differences between calculated and measured values. The simulation of the neutron source is based on many educated guesses about the structure, dimensions, and materials inside the lead capsule or the borosilicate glass plate, since no detailed information was available. Furthermore, there are some uncertainties in the measurements such as the exact position of the TLDs and bubble detectors in relation to the neutron source. Despite the uncertainties it was concluded that the simulated flux values are sufficiently accurate to be used for further

analysis. However, for an improved characterization of the neutron source, further measurements must be performed. For example, an activation analysis could be useful for a better estimation of the neutron flux. In addition, further measurements with calibrated TLDs at different distances to the source and with different moderators could give more information on the accuracy of the simulation.

4.4.3 **FNG -** 14.7 MeV **Neutrons**

The Frascati Neutron Generator (FNG) is located at the ENEA Frascati Research Center and was originally used for controlled thermonuclear fusion research. It generates monoenergetic neutrons with an energy of 14.7 MeV. Molecular and atomic deuterium ions are produced by a duoplasmatron and separated by a bending magnet. The atomic deuterium ions are subsequently accelerated up to 300 keV in a linear electrostatic accelerator. The beam is finally focused on a tritiated target. In a D(T,n)alpha fusion reaction a neutron with an energy of 14.7 MeV and an alpha particle are produced. (Martone et al., 1994) The resulting neutron emission is nearly isotropic with an average number of $5.0 \cdot 10^{11}\ \mathrm{s}^{-1}$. The flux is determined by counting the generated alpha particles in a small silicon surface barrier detector. (Martone et al., 1994) The neutron flux distribution around the target was calculated using MCNP Monte Carlo code and was provided by the facility for the determination of the flux at the location of irradiation. Measurements with SRAMs and medical devices were performed in July 2023 under the RADNEXT program (Alía et al., 2023). The set up for medical devices behind the tritiated target is depicted in fig. 4.9.

Figure 4.9: Set up of the medical devices in front of the tritium target of the FNG.

4.4.4 MIT

High-energy proton testing was performed at the Marburger Ionenstrahl-Therapiezentrum (MIT). The facility uses a synchrotron to accelerate protons and carbon ions for radiation therapy. An energy range of 48 MeV/u to 221 MeV/u is available for protons and 86 MeV/u to 430 MeV/u for carbon ions with a maximum intensity of $1.9{\cdot}10^9$ particles/s for protons and $6.5 \cdot 10^7$ particles/s for carbon ions (Röhn-Klinikum AG, 2024).

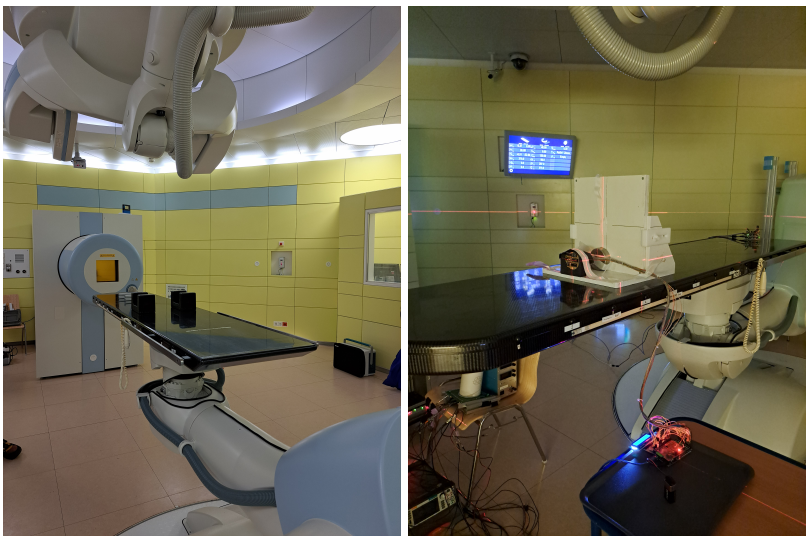

Figure 4.10: Photograph of the set-up for the SRAM irradiation at MIT.

Irradiation was carried out using a scanning beam in an area of 6 cm × 6 cm. Each point every 3 mm was irradiated with an intensity of $1.1 \cdot 10^8$ particles in a gaussian beam shape with a full-width half maximum (FWHM) dependent on the energy. Three different energies at 48.08 MeV, 152.83 MeV, and 221.07 MeV were used for testing. The respective FWHM were 32.5 mm, 11.0 mm, and 8.1 mm. In summary, a fluence of $1.2 \cdot 10^9$ cm^{-2} was obtained. The set-up is shown in Figure 4.10. Testing of SRAMs and intrathecal infusion pumps was performed in December 2022 and July 2023.

4.4.5 EMMA - Thermal Neutrons

The EMMA instrument for experiments with thermal neutrons is a beam line of the ISIS pulsed neutron source at the Rutherford Appleton Laboratory in Harwell, Oxfordshire. At this spallation source, 800 MeV protons collide with a tungsten target which results in neutron production. At the target station T1, the pulse frequency is 40 Hz. The average beam current during the beam time was 160 µA. Different moderators are introduced to slow down the neutrons after production. EMMA is in line of sight with a water moderator at room temperature at 16 m distance. For separation of the thermal component of the spectrum, a chopper is applied. It is in phase with the proton pulse to block the

beam path during neutron production and only lets the slower neutrons pass. The beam shape was adjusted to an area of 6 cm × 6 cm using B_4C jaws. (Cazzaniga et al., 2021)

Figure 4.11: Photograph of the set-up of the medical devices at EMMA.

Thermal neutron testing was performed in December 2023 under the RADNEXT program (Alía et al., 2023). An activation analysis with gold and copper foils confirmed a neutron flux of $1.53 \cdot 10^6\ \mathrm{cm^{-2}s^{-1}}$ during beam time. SRAM chips and medical devices were irradiated. The set-up for the CIEDs is displayed in Figure 4.11.

4.5 Uncertainty of the Determined Cross Sections

The main factors contributing to the uncertainty of the determined cross sections are the number of events N and the fluence Φ which was in most cases provided by the facility. Given the measurement errors ΔN and $\Delta\Phi$, the error of the calculated cross sections results in (JEDEC, 2021):

$$\frac{\Delta\sigma}{\sigma} = \sqrt{\left(\frac{\Delta N}{N}\right)^2 + \left(\frac{\Delta\Phi}{\Phi}\right)^2} \tag{4.8}$$

- **Uncertainty of the Fluence:** The uncertainty of the fluence depends on the calibration and dosimetry of the facility. Usually, there is a systematic error in the measurement of the fluence as well as an uncertainty due to the beam homogeneity. Especially, the positioning of the DUT with regard to the calibrated position influences the error in the specified fluence. Furthermore, the beam stability and neutron scattering at the experimental hall walls need to be considered. (JEDEC, 2021) In most cases, the fluence was provided by the facility and its uncertainty was considered with 10 % (Cecchetto, 2021).

- **Uncertainty of the Number of Events in SRAMs:** Bit flip events in SRAMs are of statistical nature. Therefore, their uncertainty can be decreased the more events are recorded. The number of SEE N_{SEE} is assumed to be Poisson distributed. Thus, when testing only one device and $N_{SEE} > 50$ per measurement run is reached, the uncertainty can be estimated as (Cecchetto, 2021)

$$\Delta N_{SRAM} = \sqrt{N_{SEE}}. \tag{4.9}$$

  In the most cases this number of events was not reached in each chip during the measurements. Therefore, multiple chips were tested at the same time to get a reasonably high number of events for statistics. Finally, the standard error of the mean was used as uncertainty for the number of bit flips. With this method it is additionally accounted for variations in the sensitivity to radiation across the chips of the same type.

5. The SRAM Monitor

With the previously presented methods and facilities a full characterization of the SEU cross section function for SRAMs is possible. Different measurements with multiple particle species and energies were performed in order to run simulations and compare them with experimental datasets. Ultimately, this allowed for the determination of the parameters for the intermediate neutron energy weighting function $w_{im}(E)$ for the differential neutron spectrum in order to calculate reset rates in AIMD in various radiation environments. Therefore, the response of the tested SRAMs could be directly related to the AIMDs at the not-testable neutron energies.

Concerning AIMDs, it was not possible to read out any malfunctions directly at the irradiation facility, but only a few days or even weeks later at the hospital. Hence, it could not be ascertained during the beam time that the fluence was sufficient for inducing bit flips and that the devices were irradiated successfully. Therefore, an SRAM monitor was developed based on the tested SRAMs to confirm any bit flips at a certain fluence during the irradiation of the AIMDs. SRAM detector systems are widely used to measure the fluence and are often seen as beam line monitoring systems at accelerators (Harboe-Sorensen et al., 2005; Obermueller et al., 2018; Spiezia et al., 2011). Furthermore, some devices were characterized at various beam lines throughout Europe and serve as devices for comparing the dosimetry of heavy ion and proton test facilities as well as quasi-monoenergetic neutron and spallation sources (Alía et al., 2018; Cecchetto et al., 2021; Coronetti et al., 2020). However, in order to better understand the occurring radiation effects, to estimate the influence of different particle energies, and to understand how the effects may be simulated, the SRAMs were tested at various facilities.

First of all, the response of the SRAMs was characterized with heavy ions to determine basic parameters like the sensitive volume and critical charge. This enabled the simulation of the response to neutron and proton radiation of the chips above an energy of 1 MeV using the G4SEE tool. The corresponding experimental dataset was acquired with monoenergetic neutrons and protons at five different energies according to the JEDEC JESD89B standard (JEDEC, 2021). Furthermore, the susceptibility to thermal neutrons was tested. Finally, the SEU cross section function was determined from the acquired re-

sults which was subsequently used to calculate the single event rate for the SRAM monitor in various radiation environments. With additional measurements with the Am-Be neutron source the presented method for the determination of the single event rate in mixed radiation environments was validated before it was applied to AIMDs.

5.1 SRAM Monitor Setup

The setup consisted of an Arduino Mega 2560 and a connected custom-made daughterboard with space for 13 chips. Furthermore, a display, a control button, and LEDs for monitoring and an easy read-out were added to the Arduino. The microcontroller was further extended with an external shield for the RTC-clock and SD-card to save the collected data. The full set-up is shown in figure 5.1.

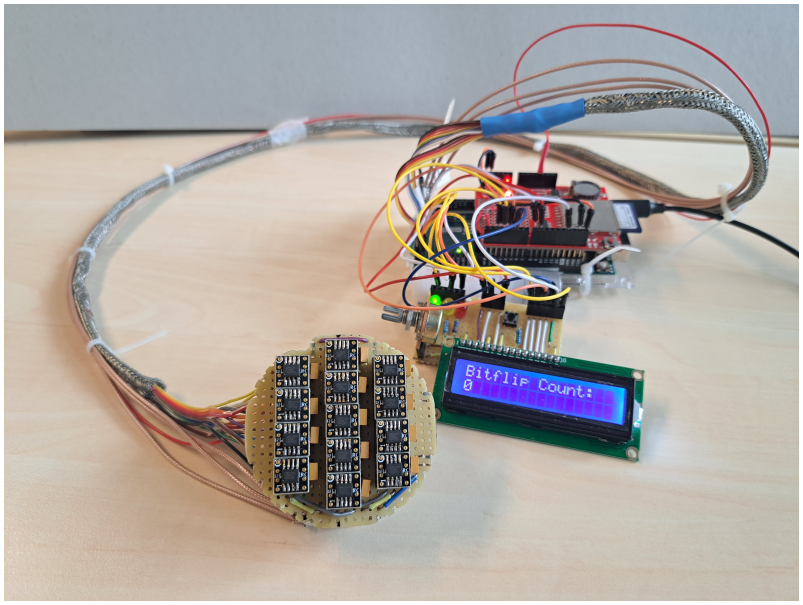

Figure 5.1: The SRAM monitor set-up with the daughterboard containing the 13 chips in the foreground. It is connected with coaxial-cables to the Arduino and the board with the display, diodes and buttons for controlling the devices.

The daughterboard was 6 cm in diameter to fit into the glass tube of the Am-Be neutron source. 13 chip-sockets with 8 pins were soldered onto the board to make an easy exchange of SRAMs possible. All MOSI, MISO and CLK pins of the individual chips were combined to communicate with the serial peripheral interface (SPI) of the Arduino. In addition, all chips were grounded. When testing radiation effects, the voltage is usually reduced to the smallest possible value to reach maximum sensitivity. However, in all experiments in this work the chips were connected to a voltage supply of 3.3 V. The CS-pins were used for individual communication with the chips. The remaining pins were soldered to resistors. The chip-daughterboard was connected with 1 m long co-axial ca-

bles to the Arduino, to keep the microcontroller out of the radiation field and to avoid any electromagnetic interference in accelerator environments.

5.1.1 Software

The Arduino was programmed to execute reading and writing operations on the chips. In the first step, a predefined pattern of bits was written on each chip. The decimal number 170 was chosen for each byte which equals 10101010 in binary. Although this is not a true checkerboard pattern, an equal number of zeros and ones could still be tested and any favored direction of bit flips identified. The chips were written sequentially, as this mode was found to provide the most accurate detection of SEEs due to the shortest dead time (Obermueller et al., 2018). Therefore, the writing process was performed in blocks of 256 addresses until the maximum number of addresses was reached. To identify any bit flips, the bytes were subsequently read out, likewise in the sequential mode. If the value of one of the bytes differed from 170, most likely a bit flip had occurred and the new value, the address, the chip, and the time of the event were logged.

Due to different fluences and expected bit flip rates in the various test environments, two different read out programs had to be designed. For a low rate of bit flips in a specific radiation environment, the chips were tested dynamically and a temporal resolution of SEUs could be achieved. Therefore, the chips were read out continuously. After a bit flip was identified, the affected chip was rewritten with the standard pattern. At a high bit flip rate, this method could have led to underestimating the number of bitflips due to the dead time during the writing process. Consequently, a second program was designed to test statically. In this case, all bytes were read out at once after irradiation which was started manually from a computer connected via USB or by pressing the control button.

5.1.2 SRAM Chips

Three different commercial-off-the-shelf (COTS) SRAMs were screened for their sensitivity to neutrons, before the final chip for the SRAM monitor was chosen. The 23LC1024 chip is a 1 Mb serial SRAM in an 8-lead Plastic Dual-in-Line package (PDIP) produced by Microchip Technology, Taiwan (Microchip Technology Inc., 2011). It is based on a 130 nm semiconductor process technology and is built in a 128k x 8-bit architecture. The IS62-65WVS2568GALL and IS62-65WVS5128GALL are Small Outline ICs (SOIC) produced by ISSI, USA. They are 2 Mb and 4 Mb in memory size, built in a 256k x 8 and 512k x 8 architecture, and rely on a low power CMOS technology (ISSI, 2021a; ISSI, 2021b). According to the manufacturer, the chips are based on a 65 nm chip technology. Subsequently, the chips are referred to as the 1 Mb, 2 Mb, and 4 Mb chips, respectively.

For device testing and any necessary simulations, it is crucial to estimate the material and thickness of the layers above the die of the SRAM. Therefore, X-ray images were

taken of each chip to measure the dimensions of the die inside the case and the thickness of the plastic in front of it. The images which were taken at the Institute of Materials Research at DLR by A. Francke are shown in figure 5.2.

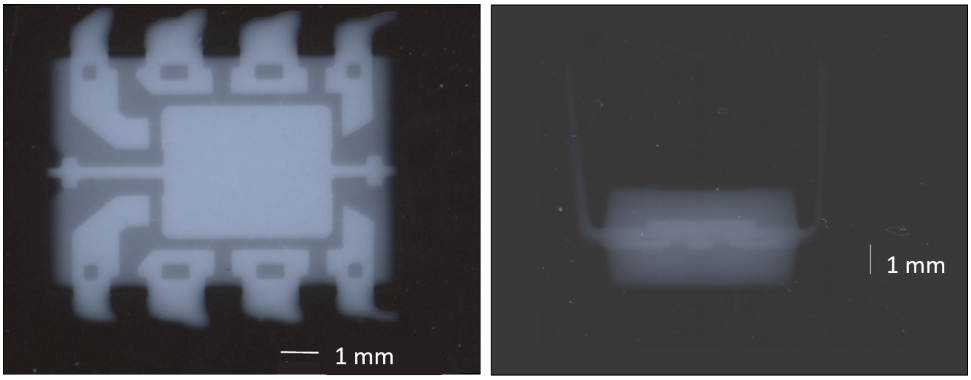

(a) 23LC1024 (1 Mb)

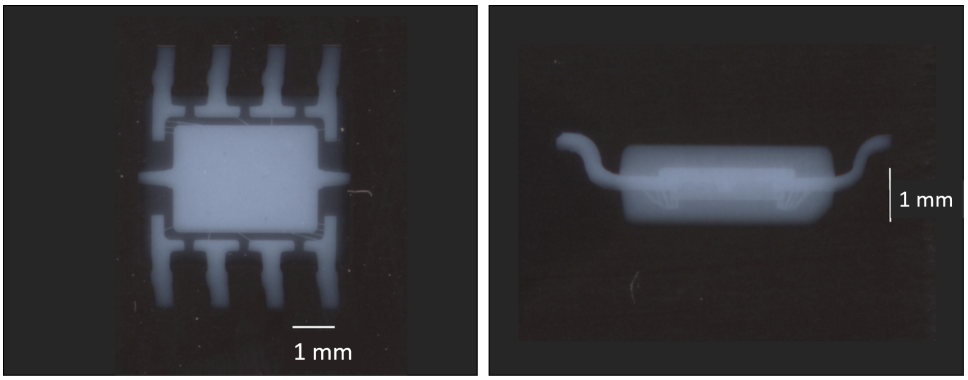

(b) IS62-65WVS2568GALL (2 Mb)

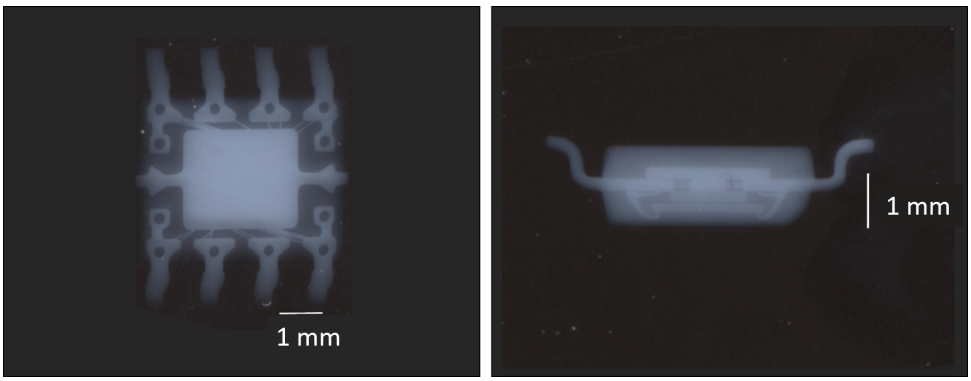

(c) IS62-65WVS5128GALL (4 Mb)

Figure 5.2: For each SRAM type the X-ray images from the top are shown on the left and the cross sectional view on the right. The images for the 23LC1024 were taken at 30 kV with 60 s exposition. The smaller chips were exposed at 20 kV for 60 s. (Personal Communication Francke, 2022)

The pictures on the left show a top view of the chips. In all three images, the die

can be well identified and measured. Even the wire bonding to the surrounding pins are visible. The cross sectional images on the right side were used to estimate the thickness of the package material above the die. All chips are shown upside down. Therefore, the thickness was measured from the lower boundary of the package to the edge of the die which was identified as the brighter plane inside. It is noteworthy that the 4 Mb chip features a stacked architecture comprising two dies. A summary of the specific device parameters for the SRAMs and the results of the measurements are shown in table 5.1.

Table 5.1: Characteristics of the different SRAM chips which were used for the screening.

Chip	Size /Mb	Tech. /nm	Die Size /mm	Package Depth /mm
23LC1024	1	130	(4.6 ± 0.1) x (3.6 ± 0.1)	1.3 ± 0.1
IS62-65WVS2568GALL	2	65	(3.5 ± 0.1) x (2.4 ± 0.1)	0.5 ± 0.1
IS62-65WVS5128GALL	4	65	(3.5 ± 0.1) x (2.4 ± 0.1)	0.3 ± 0.1 0.5 ± 0.1

Additionally, an X-ray diffraction analysis of the 1 Mb chip revealed an aluminum trihydroxide component. This is often used as filler material in polymers. Consequently, it was assumed that the package material was similar to Corian® which consists of 67 % Al_2O_3 and 33 % PMMA.

5.1.3 Analyzing Bit Flips

The raw file of the logged bit flips contains the value of the byte which differed from 170, its address, the chip number, and the time of detection for dynamic testing. In the subsequent analysis, it was distinguished between different types of bit flips. They are exemplarily shown in figure 5.3. The total number of bit flips which were recorded is referred to as ”all”. If one particle only induces one bit flip and no effects on neighboring addresses were observed, the event is hereafter called Single Bit Upset (SBU) (green dot). Any identified events that have neighboring addresses and show a bit flip at the same location in the byte are combined into one Multi Cell Upset (MCU) (blue dots). They are assumed to be caused by a single incident particle and its secondary products. Neighboring addresses are defined as addresses which are at maximum three addresses apart. Furthermore, due to the special architecture of the chips, events which are 1023, 1024, or 1025 addresses apart and happen in the same bit in the byte are also combined to one MCU. The presumed scheme of addresses in an SRAM is also shown in figure 5.3. Single Event Upsets (SEU) are defined as all events caused by one particle, regardless of the

actual number of bit flips that occurred. Hence, the number of SEUs equals the number of SBUs plus the number of MCUs.

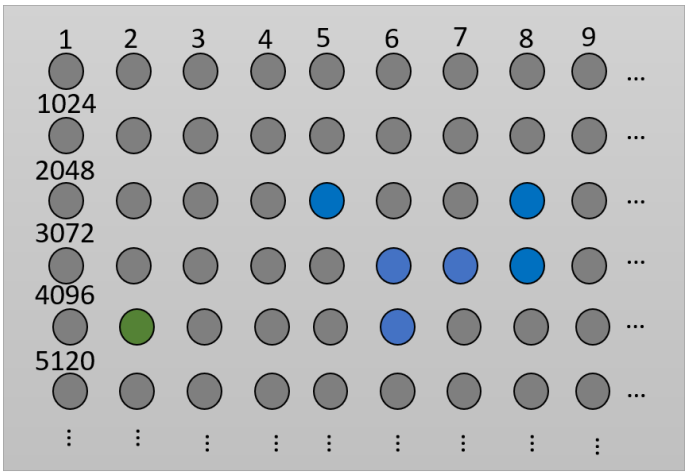

Figure 5.3: Scheme of the presumed address layout and types of bit flips. Two SEUs with all in all 7 bit flips ("all") are shown. The green dot shows one SBU, the blue dots are one MCU.

5.2 Qualification Tests at the Am-Be Neutron Source

The SRAM monitor was run for 24 h, before it was tested with any radiation. The system ran in a stable manner and did not show any bit flips. Furthermore, the 1 Mb chip was exposed in a dynamic test to 100 kGy of X-ray radiation. Neither bit flips were logged in this measurement nor any degradation in functionality of the device were observed. Therefore, it could be concluded that this dose of X-ray radiation does not induce any SEEs or total dose effects in the chip.

Subsequently, the correct function of the set-up was tested and validated with particle radiation at the Am-Be neutron source. Measurements with the static as well as the dynamic read out method were performed and no significant difference in the number of bit flips was observed. Furthermore, the frequency of the occurring bit flips was recorded for each chip. The distribution is shown in figure 5.4.

The analysis revealed that the frequency of bit flips is Poisson distributed for all three chips. Hence, the observed events are statistically independent and indeed a result of single event effects (Obermueller et al., 2018). Moreover, the occurrence of $1 \rightarrow 0$ and $0 \rightarrow 1$ bit flips was found to be balanced.

Finally, a chip screening to find the optimal chip for the monitor was performed. All in all, seven 1 Mb chips, four 2 Mb chips and two 4 Mb chips were exposed for 24 h directly on top of the source. The simulated flux of fast neutrons described in section 4.4.2 was used to calculate the fluence at each point in time. The results are presented in figure 5.5.

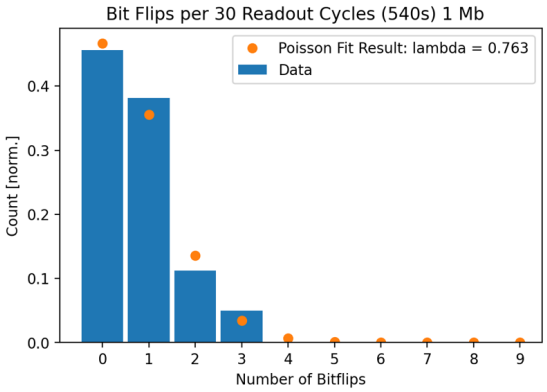

(a) 1 Mb

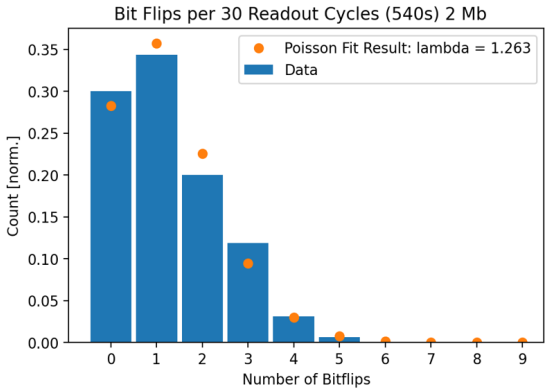

(b) 2 Mb

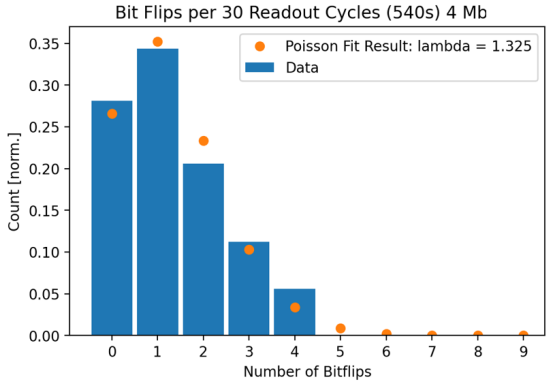

(c) 4 Mb

Figure 5.4: The number of bit flips after 30 read out cycles for each SRAM chip type fitted with a Poisson distribution.

All chips show a linear increase of the accumulated bit flips over time. The curve of each event type was fitted with a linear equation. Thus, the gradient of the curve was equal to the mean cross section of the device for the respective type of bit flip. In contrast to the larger chips, the 1 Mb chip in figure 5.5a did not show any MCUs. The 2 Mb chip in figure 5.5b was overall more sensitive to neutron radiation than the 1 Mb chip, even when normalizing the accumulated events to 1 Mb. Upon initial observation, the 4 Mb chip is more susceptible to neutron radiation than the 2 Mb chip. However, when normalizing the accumulated bit flips to 1 Mb, neutron radiation has similar effects on both chips. As a result, the 2 Mb chip was chosen for the SRAM monitor and was used in all further measurements. The 2 Mb chip is more sensitive to neutron radiation than the 1 Mb chip and therefore requires a lower fluence to cause a reasonable amount of bit flips for future measurements. Furthermore, the packaging is thinner which causes less unwanted interaction and secondary effects of radiation. Due to the same sensitivity, it can be assumed that the 4 Mb chip consists of two stacked 2 Mb chips. Since the upper chip could block radiation from the lower chip or cause more secondary particles, bit flip results could be distorted with this chip type.

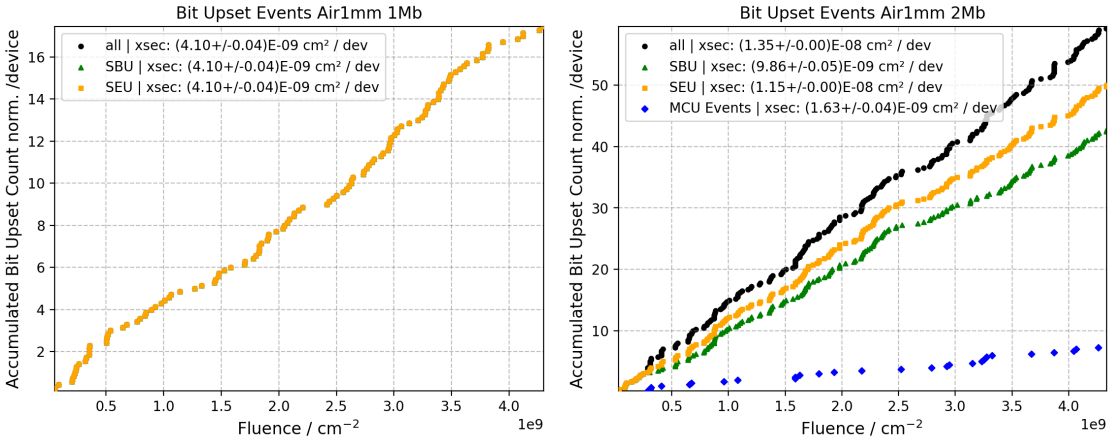

(a) 1 Mb (b) 2 Mb

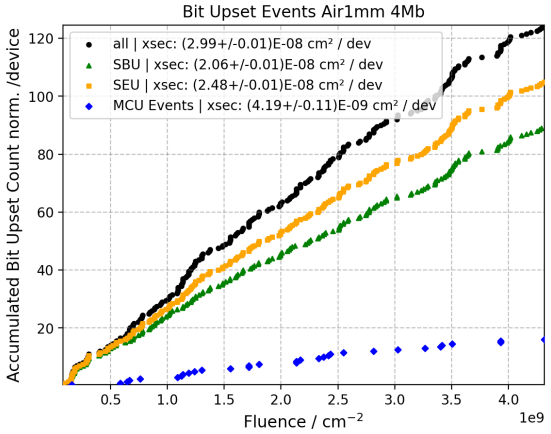

(c) 4 Mb

Figure 5.5: Accumulated bit flips over fluence for all three SRAM chip types. The black line shows all bit flips, the orange line the SEUs, the green line the SBUs and the blue line the MCUs. The fitted cross section is shown in the legend

5.3 Heavy Ion Irradiation

Heavy ion testing of the SRAM monitor was performed at GANIL using C-12 and Fe-56 ions. The goal was to determine a critical charge and a sensitive volume for the SRAM chip for subsequent simulations of the response to neutrons and high energy protons. Therefore, the cross sections for SEE at different LETs were measured and consequently the Weibull function described in section 4.2.1 was fitted to the results. For a variation in LET, the devices were tested behind two PMMA degraders with different thicknesses for the C-12 ions and at different irradiation angles for the Fe-56 ions. The respective effective LET values in the sensitive volume were previously calculated in section 4.4.1.

5.3.1 C-12

For the 17.9 mm PMMA degrader, a fluence of $1{\cdot}10^7$ cm^{-2} at a flux of $2{\cdot}10^5$ cm^{-2}s^{-1} was chosen and an LET value of 0.6 MeVcm^2/mg was determined. The number of single and multiple bit flips as well as the cross section for all events induced by one impinging particle (SEU) are presented in table 5.2.

Table 5.2: Results of the C-12 irradiation behind the 17.9 mm (0.6 MeVcm^2/mg) and 19.8 mm degrader (no LET value). The measurements were taken at a fluence of $(1.0 \pm 0.1) \cdot 10^7$ cm^{-2}

LET / MeVcm²/mg	SBU / dev.	MCU / dev.	σ_{SEU} / cm²/dev.
0.6	9395 ± 162	350 ± 18	$(9.7 \pm 0.9) \cdot 10^{-4}$
-	65 ± 4	11 ± 1	$(7.5 \pm 0.7) \cdot 10^{-6}$

Additionally, the SRAMs were tested behind a 19.8 mm PMMA degrader at the same fluence and flux. The result of this measurement is shown in the second line of table 5.2. Based on a first SRIM calculation (Ziegler et al., 2010), it was assumed that in this measurement, the number of bit flips would be higher in comparison with the 17.9 mm degrader, due to a higher expected energy deposition of the C-12 ions. However, a strong reduction is observed. As described in section 4.4.1, the Geant4 simulation for this degrader led to the assumption that the carbon ions are stopped in the sensitive volume behind the thicker degrader which was not obvious from the first SRIM simulation. Hence, any observed effect with this degrader could be attributed to ions produced due to fragmentation. Another support for this hypothesis is the high amount of observed MCU events with respect to the recorded number of SEUs in the measurement with the 19.8 mm compared to the 17.9 mm degrader. This might be caused by the effects of scattered secondary particles. Consequently, the obtained cross section for the 19.8 mm degrader cannot be used for further analysis.

5.3.2 Fe-56

In contrast to the C-12 measurement, the SRAMs were measured without degraders but at different angles in the Fe-56 campaign. This allowed for testing multiple LET_{eff} with the same ion at the same energy (refer to section 4.4.1). Before testing the different angles, an optimal fluence had to be chosen. For this reason, multiple fluences were tested at an angle of 0°. The result is shown in figure 5.6.

The number of observed bit flips increases with the fluence in a linear relation. This shows the independence of the cross section of the chosen fluence during the measurement. In addition, it could be concluded from the data that each cell in the SRAM has an equal probability to be affected by a single particle. If there was a difference in the sensitivity

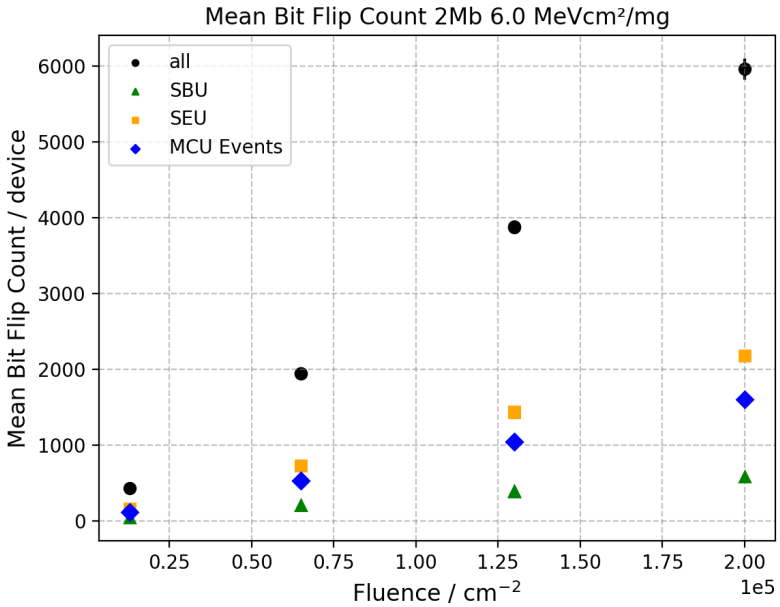

Figure 5.6: The effect of different fluences of Fe-56 ions on the count rate of the 2 Mb SRAM at 0° irradiation angle.

of the cells, the increase of the registered number of bit flips would not be linear with increased fluence. The described effects can also be observed for MCUs.

For further measurements with Fe-56 ions, a fluence of $1.3 \cdot 10^5\,\mathrm{cm}^{-2}$ at a flux of $1 \cdot 10^3\,\mathrm{cm}^{-2}\mathrm{s}^{-1}$ was chosen. The results of the irradiations at the respective LET_{eff} are presented in table 5.3. The effective fluence Φ_{eff} was used for the calculation of the cross section.

Table 5.3: Bit flips and cross sections for the Fe-56 irradiation at different LET_{eff} through a changed irradiation angle.

LET_{eff} / **MeVcm²/mg**	Φ_{eff} / cm^{-2}	**SBU** / **dev.**	**MCU** / **dev.**	σ_{SEU} / **cm²/dev.**
6.0	$(1.3 \pm 0.1) \cdot 10^5$	393 ± 4	1046 ± 18	$(1.1 \pm 0.1) \cdot 10^{-2}$
7.8	$(1.7 \pm 0.2) \cdot 10^5$	289 ± 8	1002 ± 15	$(1.3 \pm 0.1) \cdot 10^{-2}$
9.3	$(2.0 \pm 0.2) \cdot 10^5$	213 ± 6	876 ± 10	$(1.3 \pm 0.1) \cdot 10^{-2}$
17.6	$(2.6 \pm 0.3) \cdot 10^5$	189 ± 5	804 ± 12	$(1.5 \pm 0.2) \cdot 10^{-2}$

In all measurements, the observed number of MCUs is considerably higher than the number of SBUs. Therefore, one iron ion generates charges in an area which exceeds the size of one cell of the device. This is often observed in heavy ion testing and further investigated in section 5.3.3. The values for the cross sections are similar across all irradiation angles. This might indicate that the cross section has already reached its saturation value.

5.3.3 Multiple Cell Upsets

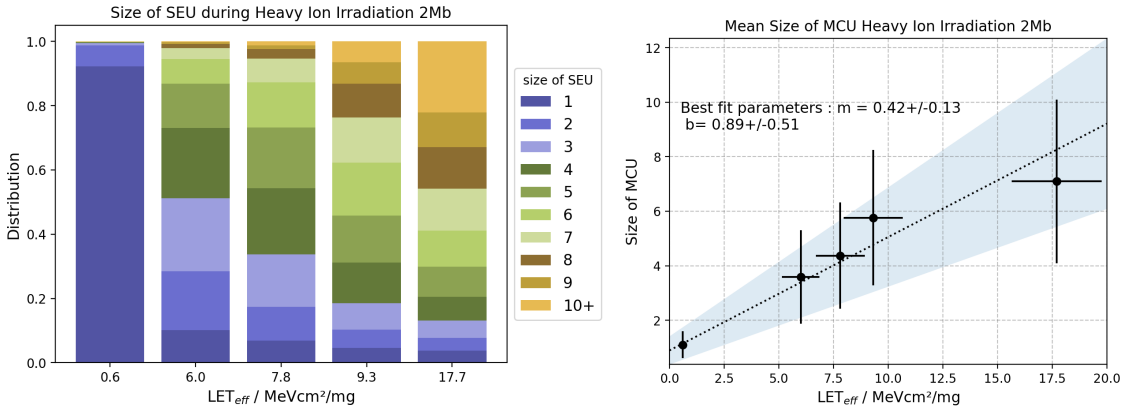

(a) Percentages of the SEU sizes related to all recorded bit flips.

(b) Mean sizes of the MCUs at different LETs.

Figure 5.7: Characterization of MCUs at different LETs.

The majority of the events observed in the Fe-56 measurements were MCUs. Figure 5.7a illustrates the distribution of SEU sizes with respect to the total number of SEUs. With higher LET_{eff} values, the MCU size increased and the relative amount of SBUs decreased. Especially in the measurements with Fe-56 ions only few SBUs were still observed. In previous investigations, a similar observations were made, e.g., (Giot et al., 2008; Lawrence and Kelly, 2008) and explained with the higher number charge carriers and their wider distribution in the material across multiple cell sizes at higher LETs. Thus, larger clusters of MCUs due to one impinging particle are observed. SBUs could consequently only be found at the edges of the structure (Correas et al., 2009). In addition, figure 5.7b depicts the mean MCU multiplicity depending on the effective LET. It shows a linear relation which could imply that the observed effects are independent of the angle of irradiation in heavy ion testing.

5.3.4 Definition of the Parameters for Simulation

The aim of the heavy ion measurements was to assess the basic chip parameters for the simulation of SEUs in the investigated SRAMs. In particular, the sensitive area and the critical charge are deduced from the measured data. Apart from the values acquired from carbon and iron irradiation, a cross section for radiation effects of alpha radiation was provided by the manufacturer (Personal communication Integrated Silicon Solution Inc.). Finally, the four-parameter Weibull function for the analysis of heavy ion testing (refer to section 4.2.1) was fitted to all data points. This is displayed in figure 5.8. In contrast to the previous results, the cross section is here described in μm/bit to directly determine the sensitive area of each bit.

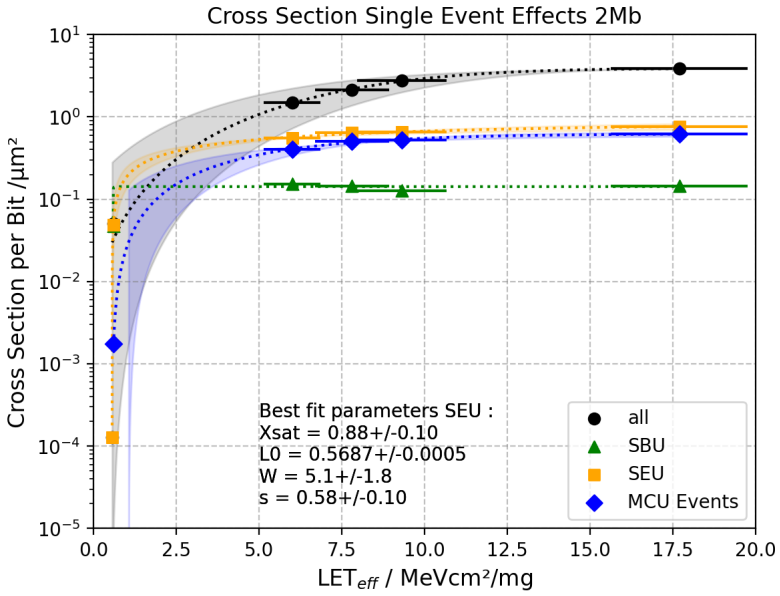

Figure 5.8: Heavy ion testing results of the SRAM monitor for C-12 and Fe-56 testing. The graph includes the fits of the Weibull curves including the uncertainties of the fit. The parameters for the SEU fit are presented.

All four curves saturate at effective LET values above 9 $\mathrm{MeVcm^2/mg}$. Furthermore, it can be identified that the ratio of SBUs to MCUs is constant in this LET range. Thus, only the multiplicity of the MCUs increases with increasing effective LETs which can be seen in the slower saturation of the curve with all recorded bit flips. There are only few points which determine the knee of the curves which results in major uncertainties. For a more sophisticated analysis at different LETs, more data points between 1 $\mathrm{MeVcm^2/mg}$ and 5 $\mathrm{MeVcm^2/mg}$ are needed. Furthermore, only two ion species were tested. Ideally, multiple ion species and angles should be tested to obtain overlapping data for comparison (JEDEC, 2017).

Nevertheless, the parameters for the Weibull fit of the SEU curve are presented in the graph. A sensitive area of 0.88 $\mu\mathrm{m}^2$ was determined. Hence, its size can be described as 940 nm × 940 nm. In previous studies values between 0.6 μm and 1.3 μm were used as side lengths for the sensitive volume of 65 nm SRAMs (Coronetti et al., 2021). Therefore, the measured result is in good agreement with previous measurements.

Since the internal structure of the SRAM chip is not known, the critical charge could not be estimated through circuit simulations. Therefore, the LET threshold of the SEU curve of 0.57 $\mathrm{MeVcm^2/mg}$ was used for the calculation of the critical charge. It is in good agreement with previous measurements for 65 nm SRAMs (Kobayashi, 2021). Using simulations, previous works found critical charges between 0.3 fC and 4 fC (Sierawski et al., 2011; Gorbunov et al., 2014) and the scaling trend approach expects 2 fC for the 65 nm technology (Pickel, 1982). As Petersen et al. proposed, an educated guess for the sensitive

depth was made and 1 μm was assumed. This results in a critical charge of 5.8 fC which is above expected values. However, it is well-known that ultra-low supply voltages lead to decreased critical charges (Clemente et al., 2018). Since, the devices were tested in the actual operating range of the chips at 3.3 V, the increased critical charge compared to previously reported values could be explained.

A summary of the input parameters for the SEE simulation is given in table 5.4.

Table 5.4: Input Parameters for the G4SEE Simulation.

Parameter	Value
Sensitive Area	940 nm × 940 nm
Sensitive Thickness	1000 nm
LET Threshold	0.57 MeVcm^2/mg
Critical Charge	5.8 fC

5.4 Simulation with G4SEE

The previously determined values were applied as input parameters for the sensitive volume in the G4SEE simulation. Additionally, the bulk was defined to be four cell sizes and therefore 1.4 μm × 1.4 μm wide and 4 μm thick. Furthermore, one BEOL layer made of SiO_2 with a thickness of 4.5 μm and a second one made of Cu with the same dimensions were added similar to what was used in previous studies and the LET simulation (Coronetti et al., 2021). A bias factor of 1000 for the physics-based microscopic cross section for the *hadElastic* and *neutronInelastic* processes were applied. Multiple monoenergetic neutron energies between 0.5 MeV and 600 MeV were simulated with 10^7 runs each. Using the simulated histograms and the determined critical charge, a neutron cross section for each energy was calculated. The result is shown in figure 5.9.

The cross section saturates already around 2 MeV. Between 2 MeV and 40 MeV the values are fluctuating around the constant saturation value. However, at higher energies above 40 MeV the cross section decreases again to a constant value of about $6 \cdot 10^{-8}$ cm^2. This simulated curve can be used as a bench mark for the measurement of neutron an proton cross sections in the SRAMs and are subsequently compared to the measured data.

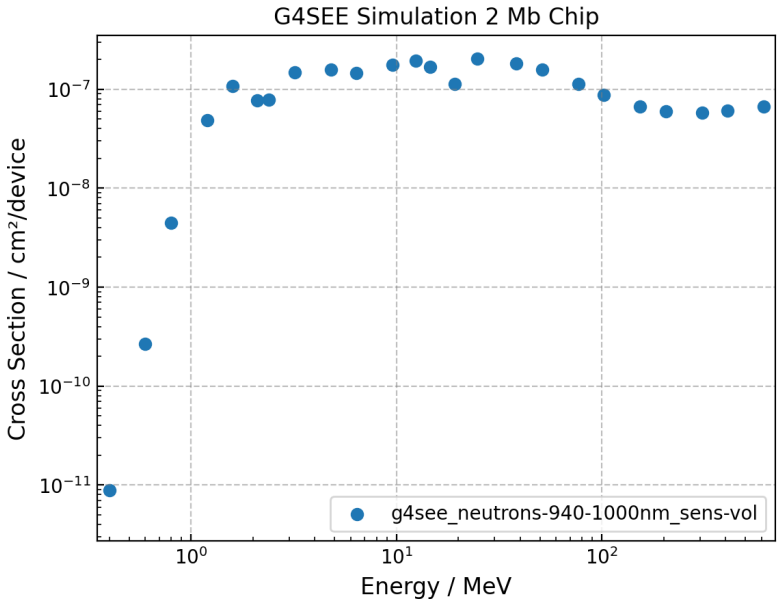

Figure 5.9: G4SEE Simulation of the cross section for SEUs for neutrons at different energies with parameters for the SRAM from table 5.4

5.5 Measurements with Neutrons and Protons

The cross section for neutrons was investigated experimentally for the SRAM monitor at the different facilities introduced in section 4.4. For the full characterization of the SRAM monitor in different radiation fields and the comparison to the previous simulation, the response to different neutron and proton energies had to be evaluated. First the SRAMs were tested for their sensitivity to thermal neutrons. Subsequently, four monoenergetic energies were tested for the determination of the Weibull function and the consequent parameters for the SEU cross section curve $\sigma(E)$, in accordance with the JEDEC JESD89B standard. The effect of high-energy hadrons was tested with protons between 50 MeV and 220 MeV, since protons and neutrons have the same characteristics regarding SEE at these energies. Moreover, 14.7 MeV neutrons and the previously described Am-Be neutron source were used for device testing.

5.5.1 Effects of Thermal Neutrons

The set-up was tested with thermal neutrons at EMMA at the ISIS Neutron Source. It was exposed for 11 h and tested dynamically. The results are presented in table 5.5

The cross section for SEUs due to thermal neutrons of $(5.6 \pm 0.8) \cdot 10^{-10}\,\mathrm{cm}^2/\mathrm{dev}$ is comparably low with regard to the first test measurements at the Am-Be neutron source presented in section 5.2. The set-up was not tested with a Cadmium blocker. Therefore, any effects of epithermal or residual fast neutrons cannot be ruled out. However, since the thermal neutron cross section is lower than the one of the Am-Be test measurements,

Table 5.5: Results for the thermal neutron irradiation at a fluence of $(6.1 \pm 0.6) \cdot 10^{10}\ \mathrm{cm}^{-2}$.

Energy / meV	SBU / dev.	MCU / dev.	σ_{SEU} / cm²/dev.
20	29 ± 3	6 ± 1	$(5.6 \pm 0.8) \cdot 10^{-10}$

distortion form these energies is unlikely. The observed MCU events consisted mostly of two bit flips. Only very few events had a multiplicity of three.

Single event effects induced by thermal neutrons are most likely the result of a neutron capture reaction with B-10. Auden et al. suggest that boron is located close to the sensitive volume either in the doped p-type silicon which can be found in the well, source, or drain of the transistors (Auden et al., 2020). All byproducts of the neutron-boron reaction, in particular the alpha particle and the Li nucleus, have a stopping distance above $2\ \mu$m (Auden et al., 2020). Hence, these secondary products can easily reach a neighboring cell and cause an MCU.

5.5.2 MIT - High Energy Protons

In general, high energy hadrons are used to determine the saturation cross section for SEE in electronics. Thus, a maximum sensitivity of the device to neutrons can be estimated. The SRAM monitor was statically tested with protons at MIT. Three different energies were used for determining the saturation cross section. The results are listed in table 5.6.

Table 5.6: Results for the irradiation with protons at different energies and a fluence of $(1.2 \pm 0.1) \cdot 10^{9}\ \mathrm{cm}^{-2}$.

Energy / MeV	SBU / dev.	MCU / dev.	σ_{SEU} / cm²/dev.
50	56 ± 6	18 ± 3	$(6.1 \pm 0.9) \cdot 10^{-8}$
150	52 ± 3	25 ± 3	$(6.4 \pm 0.7) \cdot 10^{-8}$
220	53 ± 6	25 ± 3	$(6.5 \pm 0.7) \cdot 10^{-8}$

The number of SBUs and MCUs and the resulting cross section remain constant with increasing energy, indicating that the saturation of the cross section has been reached. Therefore, the maximum SEU cross section induced by hadrons is about $6.3 \cdot 10^{-8}\ \mathrm{cm}^2/\mathrm{dev}$. The G4SEE simulation estimated the saturation cross section with $6 \cdot 10^{-8}\ \mathrm{cm}^2/\mathrm{dev}$ which is in very good agreement with the measured values. With increasing proton energy, the MCU multiplicity increases. For 50 MeV the largest MCU consists of 7 bit flips, whereas at 150 MeV 11 bit flips are observed in one event and 13 bit flips at 220 MeV.

5.5.3 FNG - 14.7 MeV Neutrons

The SRAM monitor was tested at the FNG to evaluate the response to monoenergetic 14.7 MeV neutrons. In previous studies it has been proposed that although it might underestimate the MCU sensitivity, the cross section found at this energy can be used to estimate the saturation cross section (Clemens et al., 2011; Miller et al., 2013). The SRAMs were tested in static mode and the results are reported in table 5.7.

Table 5.7: Results for the irradiation with 14.7 MeV neutrons and a fluence of $(2.0 \pm 0.2) \cdot 10^9\,\mathrm{cm}^{-2}$.

Energy / MeV	**SBU / dev.**	**MCU / dev.**	σ_{SEU} **/ cm²/dev.**
14.7	109 ± 4	29 ± 1	$(6.9 \pm 0.7) \cdot 10^{-8}$

The simulated cross section value for 14.7 MeV was estimated with $1.7 \cdot 10^{-7}\,\mathrm{cm}^2/\mathrm{dev}$, thus overestimating the measured value of $(6.9 \pm 0.7) \cdot 10^{-8}\,\mathrm{cm}^2/\mathrm{dev}$ by a factor of 2.5. However, in comparison with the measurement with high-energy protons, the measured cross section for SEUs induced by 14.7 MeV neutrons is in a similar range. This confirms previous assumptions that the high-energy saturation cross section can be estimated with 14.7 MeV at least for the tested chip. An MCU multiplicity of up to 6 bits was observed, however, in the majority of MCU events only involved 2 bits.

5.5.4 Am-Be Neutron Source

The JESD89B standard suggests testing between 1 MeV and 10 MeV for considering the effects of the varying cross section in this energy range. As a consequence, the chips were tested at the Am-Be neutron source. In contrast to the previously described measurements, this test was not performed with monoenergetic neutrons but with mixed neutron energies. As already described in section 2.5, in a mixed radiation environment the overall number of bit flips consists of the considerations for the thermal equivalent part and the high-energy section. In testing with thermal neutrons and comparing them with the high-energy hadron data, it has been found that the thermal cross section is two magnitudes lower than the high-energy cross section for the investigated chip. Hence, for calculating the cross section of the Am-Be neutron source, only the simulated flux of fast neutrons above 0.1 MeV was used. According to the performed simulation, the mean energy of the fast neutrons is (3.6 ± 2.4) MeV with a maximum energy of 12 MeV. The chips were tested in the dynamic mode. The results for the number of bit flips and the resulting cross section for SEUs are shown in table 5.8.

Due to the mixed neutron energy field, it is difficult to define a discrete energy for this radiation effects test. Ultimately, the mean energy of the fast neutrons of the simulated spectrum was used as a reference energy. Most of the reported MCUs included two flipped

Table 5.8: Results of the irradiation at the Am-Be neutron source with a fluence of $(4.3 \pm 0.4) \cdot 10^9\ \mathrm{cm}^{-2}$.

Energy / MeV	SBU / dev.	MCU / dev.	σ_{SEU} / cm²/dev.
3.56 ± 0.02	43 ± 9	8 ± 4	$(1.2 \pm 0.1) \cdot 10^{-8}$

bits. Only few were observed where three or more bits were involved with a maximum multiplicity of five. Similar observations for neutrons below 10 MeV were reported by Sierawski et al. The measured SEU cross section of $(1.2 \pm 0.1) \cdot 10^{-8}\ \mathrm{cm}^2/\mathrm{dev}$ is a factor of 5 lower than the saturated cross section of high-energy protons, indicating that there is a change of sensitivity of the SRAM to the neutrons in the energy range of the Am-Be source. While neutrons with the highest energies of the Am-Be source around 10 MeV might still induce SEUs with a cross section close to the high-energy neutron cross section, energies around the mean neutron energy of the source might already have a lower probability to induce effects.

Experimenting with Moderators

In order to specify the influence of different ranges of the neutron energy spectrum on the SEU cross section, different moderators were tested in front of the SRAM monitor. The device was placed at a distance of 30 mm to the source. In one experiment, a 6 mm thick borosilicate glass plate was used to reduce the thermal neutron flux and to confirm the assumption that neutrons with thermal energies do not influence the number of SEUs considerably in this radiation environment. In a second experiment, a 30 mm paraffin-wax block was introduced to moderate the fast neutrons and to decrease the flux of neutrons with high energies. It was proposed that if a reduction in the observed number of SEUs was found with this moderator, the SEUs would indeed be triggered by neutrons with the highest energies of the Am-Be source. The respective spectra for this investigation were calculated with the help of the neutron source model described in section 4.4.2. The results are depicted in figure 5.10, the spectrum without moderator at 30 mm distance is used as reference.

As expected, the borosilicate glass in figure 5.10a reduces the number of thermal neutrons at 30 mm distance. A measurement with TLDs confirmed a thermal neutron dose of only one third of the initial dose without a moderator at the same distance. In contrast, the total flux of neutrons with the paraffin block is reduced in comparison to the reference spectrum without a moderator. This is surprising, since an increase in the thermal neutron flux was expected and shown previously. Around a thickness of 2 cm to 5 cm of paraffin the thermalizing effect is supposed to be at maximum (Rieppo, 1984). However, no TLD measurements were available for this condition to confirm the calculated spectrum. The

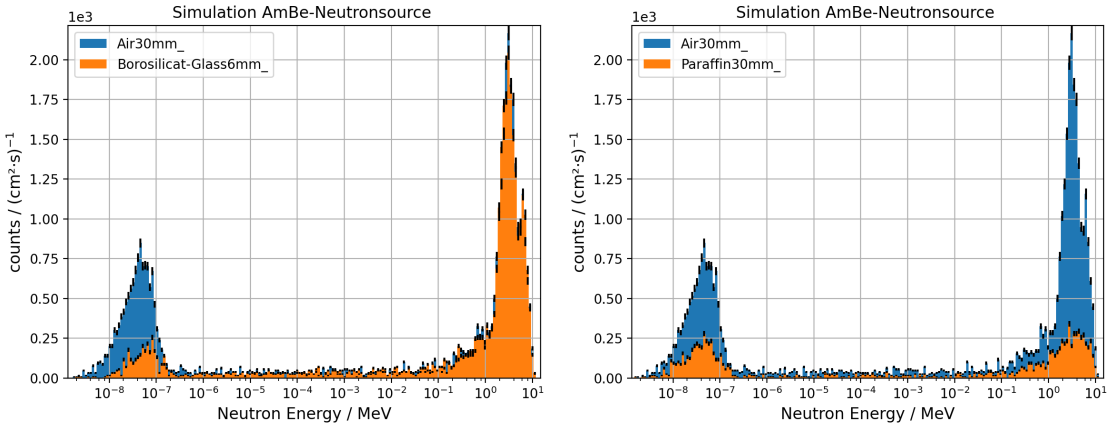

(a) 6 mm Borosilicate Glass (b) 30 mm Paraffin Wax

Figure 5.10: The simulated neutron spectra behind two different moderators are compared with the neutron spectrum without a moderator at 30 mm distance.

SRAM monitor was exposed to the different moderated neutron fields and the SEEs were recorded dynamically. The results are presented in table 5.9. The more detailed graphs for the accumulated bit flips over the simulated fast fluence for each measurement can be studied in the Appendix A.1.

Table 5.9: Results of measurements with different moderators at 30 mm distance.

Moderator	**Fast Fluence / cm^{-2}**	**SBU / dev.**	**MCU / dev.**	σ_{SEU} **/ cm²/dev.**
Air	$(1.5 \pm 0.2) \cdot 10^{9}$	20 ± 1	3 ± 1	$(1.5 \pm 0.2) \cdot 10^{-8}$
Borosilicate Glass	$(1.3 \pm 0.1) \cdot 10^{9}$	14 ± 1	2.0 ± 0.3	$(1.2 \pm 0.1) \cdot 10^{-8}$
Paraffin	$(4.5 \pm 0.5) \cdot 10^{8}$	10 ± 1	1.0 ± 0.3	$(2.5 \pm 0.3) \cdot 10^{-8}$

The contribution of thermal neutrons to the SER was again assumed to be negligible due to the small cross section. Hence, only the fast neutron components as the cause for bit flips were evaluated. As expected, the air and borosilicate glass measurements are comparable. The discrepancy can be explained by the low bit flip count and consequent weak statistics. In contrast, the cross section for SEUs with the paraffin moderator is 1.5 times higher than without a moderator. This was contradicting to the original hypothesis, since with a decrease in the fast neutron flux a decrease in the cross section for SEUs was expected. An explanation for this effect might be the emission of secondary protons produced in the paraffin with a maximum energy of around 5 MeV. They are directly ionizing and have a considerably higher cross section for SEUs than neutrons at the same energy. It can even exceed the saturation cross section for high-energy hadrons (Coronetti et al., 2021; Sierawski et al., 2009).

All in all, the moderator experiments showed that the effects are indeed produced by fast neutrons above 0.1 MeV. However, the paraffin experiment did not show the expected results and hence no conclusion can be drawn if the observed SEUs were only caused by neutrons with the highest energies of the Am-Be neutron spectrum. Further experiments with different moderators would be necessary to confirm this assumption. Nevertheless, in the absence of supplementary data points or information necessary to unfold the Am-Be spectrum, in the following analysis the Am-Be data point will be set to the mean energy of the fast neutrons at 3.6 MeV.

5.6 Comparison of Multiple Cell Upsets

At all tested neutron and proton energies, MCU events were observed. However, their percentage and multiplicity change with different particle energies. For thermal neutrons, the MCUs have already been discussed in section 5.5.1. A more detailed analysis of the MCUs at all remaining energies is shown in figure 5.11.

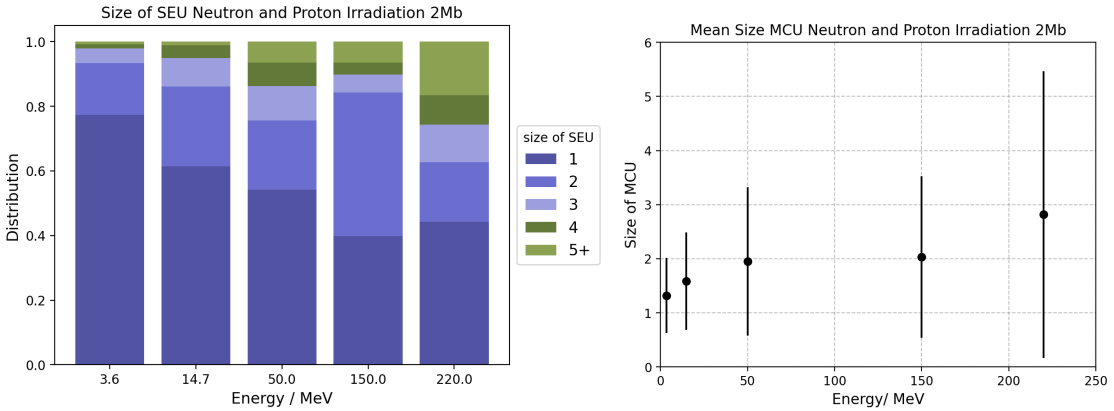

(a) Distribution of MCU sizes normalized to full number of bit flips.

(b) Mean size of MCUs

Figure 5.11: Distribution and size of MCUs at different energies.

The percentage of MCUs increases with increasing energy with the exception of the last measurement at 220 MeV shown in figure 5.11a. A previous study for a 180 nm semiconductor process technology suggests a Weibull type function for the percentage of the MCU depending on the neutron energy, saturating above an incident neutron energy of 100 MeV (Yahagi et al., 2007). Moreover, a simulation study by Serre et al. with the 65 nm chip technology found that MCUs comprise at maximum 65 % of all SEUs. Above 100 MeV, this value did not increase with a neutron energy of 1 GeV (Serre et al., 2012). The maximum percentage of MCUs was observed to be 60 % at a proton energy of 150 MeV in this work which is close to the simulated value presented by Serre et al. A saturation effect of the MCU percentage may have been observed above a proton energy of

100 MeV in the presented experimental data. However, further measurements with higher neutron or proton energies are necessary to confirm this assumption. A similar saturating effect could be observed in the mean multiplicity of events illustrated in figure 5.11b. However, the uncertainties are to extensive to take any conclusions.

SEUs induced by neutrons with energies below 10 MeV are most likely the result of elastic neutron reactions and the consequent generation of free charge carriers by recoiling particles. When calculating the energy of a Si-28 recoil from a simple elastic collision with a neutron of 10 MeV, a maximum energy of 1.3 MeV could be transferred to the silicon nucleus. Using SRIM this translates to a range of 1 μm. In the 65 nm chip technology a mean cell size of approximately 0.5 μm^2 is assumed with a side length of 0.7 μm (Correas et al., 2009). Therefore, a high energy silicon recoil nucleus could reach a neighboring cell and induce a second bit to flip. However, a higher multiplicity is unlikely to be observed with elastic neutron reactions due to the limited range of the recoiling particles. The spectrum of the Am-Be source has only a small flux of neutrons that can transfer enough energy to a silicon nucleus to reach a neighboring cell. Thus, the comparably small amount of MCUs at the 3.6 MeV datapoint in figure 5.11a is reasonable.

Above a neutron energy of 10 MeV, inelastic reactions increasingly contribute to the SEE generation. Beside alpha particles, protons, Si, Mg and Al ions become relevant for inducing bit flips. Therefore, the increase in MCU events and their multiplicity might be the result of the increase in the probability of inelastic neutron reactions with the SRAM material. At even higher neutron energies, further secondary ions are created (Serre et al., 2012). As a result, higher LETs and ion ranges can be expected which cause more MCUs in greater clusters as observed in the experimental data (Miller et al., 2013). Similarly, this effect was previously shown in the heavy ion testing. Moreover, with a higher neutron energy, more fragments are produced in inelastic reactions which is also favorable for a higher multiplicity of MCUs (Serre et al., 2012).

5.7 Combined Analysis and Comparison with Simulated Data

In comparison with the susceptibility to high-energy neutrons, the thermal neutron cross section is two orders of magnitude lower. According to Normand et al., the ratio of the thermal to the high-energy cross section can be an indication of the presence of BPSG. They conclude that if the ratio is > 0.2, BPSG is likely present (Normand et al., 2006). The examined chip has a ratio of 0.009. Hence, it can be concluded that BPSG was likely not used in the manufacturing process around the sensitive volume. Therefore, the most probable source of SEUs induced by thermal neutrons is the doping in silicon. All in all, the effect of thermal neutrons on the investigated chip is limited.

All further data from the proton and neutron measurements are summarized in figure 5.12. The values are fitted with the four parameter Weibull function using non-linear least

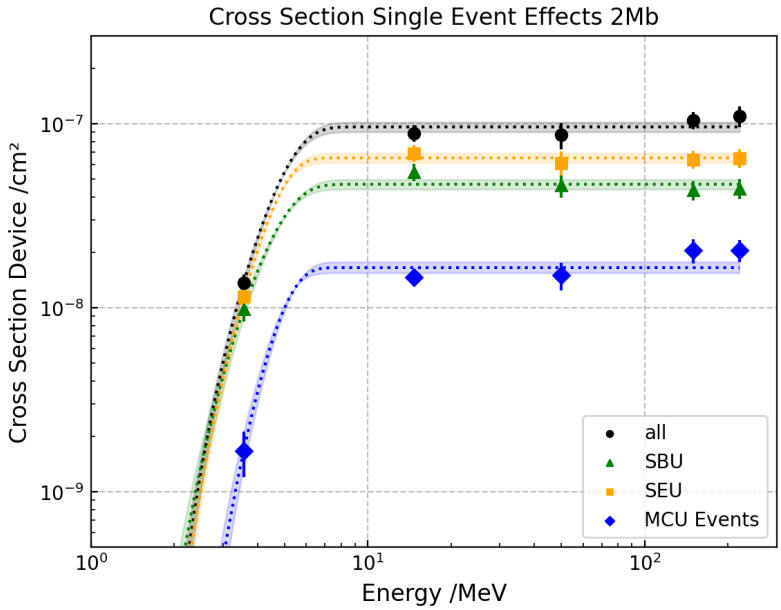

Figure 5.12: Plot of the neutron and proton cross section results for the 2 Mb SRAM. The graph includes the Weibull fits for the four types of bit flips.

square optimization. In all four bit flip types the $\sigma(E)$ has already saturated at around 6 MeV. As seen in the previous section the cross section for the MCUs tends to rise at the saturation value while the SBU cross section slightly decreases. However, the SEU cross section remains constant. It is obvious that the cross section for the Am-Be source measurement at 3.6 MeV determines the position and steepness of the knee of the fitted curve and its high uncertainty tremendously influences the outcome of $\sigma(E)$ and its parameters such as E_{thresh}. Nevertheless, it can be concluded from the measurements, that the knee of the curve must lay in the energy range of the Am-Be fast neutron peak above 3.6 MeV. Hence, for a better characterization of the cross section for SEUs of this specific chip further measurements with monoenergetic neutrons between 1 MeV and 10 MeV should be obtained.

In figure 5.13, the measured curve $\sigma(E)$ is compared to the in G4SEE simulated cross-section values for several energies. Similar to the heavy ion testing, the curve for SEUs is chosen as representation of all particles inducing events. The simulated data points reach saturation at a 4 times lower neutron energy than the measured curve. However, both curves present considerable uncertainties in the energy range of the knee of the curve due to the vague estimation of the sensitive thickness for the simulation and the absence of precise data between 1 MeV and 10 MeV.

The simulated data points exceed the measured cross-section between 6 MeV and 100 MeV by a factor of 1.5 to 3. This can be explained, e.g., by the implemented physical models and the missing knowledge of materials and layers around the sensitive volume. A factor of 2-3 can easily be caused by an over- or underrepresentation of a certain material

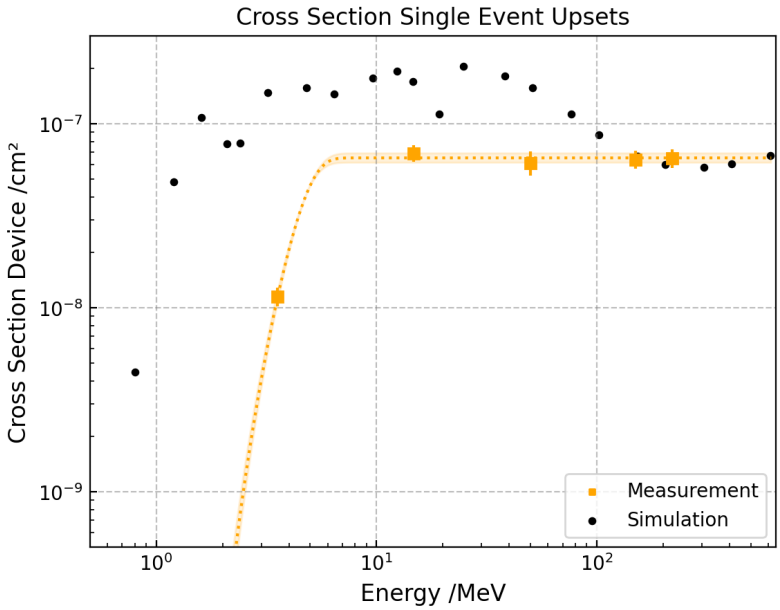

Figure 5.13: Comparison of the measured single event upsets with the values obtained from the G4SEE simulation.

(Cecchetto et al., 2021). Furthermore, the RPP model represents a strong simplification of the real sensitive area of charge collection and therefore also influences the accuracy of simulated results. At neutron energies above 100 MeV, the cross sections for both curves match again.

All in all, despite the uncertainties, the simulated data points and $\sigma(E)$ of the measured cross sections show satisfactory agreement. Therefore, the parameters E_{thresh} and σ_{sat} as well as the shape parameters W and s of $\sigma_{SEU}(E)$ are used for the intermediate neutron energy weighting function $w_{im}(E)$ for the determination of the neutron fluence in a mixed radiation environment. The parameters are shown in table 5.10.

Table 5.10: Extracted fit parameters from $\sigma_{SEU}(E)$ which are used for the intermediate neutron energy weighting function $w_{im}(E)$.

Device	σ_{sat}	E_{thresh}	W	s
SRAM Monitor	$(6.5 \pm 0.4) \cdot 10^{-8}$	(1.44 ± 0.06)	(3.36 ± 0.04)	(3.56 ± 0.02)

5.8 Validation of the Calculated SER in Mixed Radiation Environments

The measured thermal cross section of $(5.6 \pm 0.8) \cdot 10^{-10}\,\mathrm{cm}^2$ and high-energy cross section of $(6.5 \pm 0.4) \cdot 10^{-8}\,\mathrm{cm}^2$ for SEUs in the SRAM as well as the parameters for

$w_{im}(E)$ of table 5.10, can now be used to calculate the single event rate of the SRAM monitor in specific radiation environments. As described in section 2.5, the respective differential energy spectrum is divided in its thermal, intermediate, and high-energy range. Subsequently, it is weighted and multiplied by the respective weighting function and the associated measured cross section. The presented uncertainty of the resulting calculated SER is a direct consequence of the measurement uncertainty of the cross section.

5.8.1 Am-Be Neutron Source

For validation of the presented method, the single event rate of the SRAM monitor in the radiation environment of the Am-Be neutron source was calculated at two different distances with and without moderators and then compared to the measured values after certain exposure times. The results are displayed in table 5.11.

Table 5.11: Comparison of measured and calculated values for different distances and moderators at the Am-Be neutron source where the neutron spectra were previously determined with simulations.

Moderator	Distance / mm	Time/s	$N_{measured}$	$N_{calculated}$
Air	1	86 400	(50 ± 3)	(86 ± 5)
Air	30	64 500	(23 ± 1)	(28 ± 1)
Borosilicate Glass (6 mm)	30	58 080	(16 ± 1)	(25 ± 1)
Paraffin	30	82 500	(11 ± 1)	(8 ± 1)

The calculated number of bit flips at 30 mm distance to the source without moderator shows very good agreement within 20 % of the measured values. The number of bit flips for the position directly on top of the neutron source and behind a 6 mm thick borosilicate glass plate at 30 mm distance to the source is over-estimated by 72 % and 56 %, respectively. In contrast, the number of bitflips behind the paraffin wax moderator is under-estimated by 27 %. This might be indicative of an inaccuracy in the simulation of the neuron energy spectrum of the neutron source behind the paraffin moderator and possible additional influence of generated secondary protons. Considering the described high uncertainties in the simulation of the neutron energy spectrum of the neutron source, the calculation of the number of bit flips for the different positions relative to the neutron source is highly satisfactory. Moreover, the measurements confirm that the determined SEU response function leads to an acceptable calculation of the single event rate.

5.8.2 Comparison of Weibull Fits for different Chips

Cecchetto et al. characterized multiple SRAMs at different neutron energies between 0.144 MeV and 17 MeV for their cross sections for SEUs. Among others, they investigated

a 65 nm chip by Cypress (CY62167GE30-45ZXI) and the ESA SEU reference monitor. The Cypress chip was selected for comparison with the SRAM monitor since they both are based on the same semiconductor process technology of 65 nm. The well-characterized ESA monitor was chosen to show the changed SEU sensitivity of a larger chip technology. The SEU cross section functions for the two reference devices are presented in figure 5.14 in comparison with the measured cross sections and $\sigma(E)$ of the previously discussed SRAM monitor (Cecchetto et al., 2021). The different cross section curves are normalized to the saturation value σ_{sat} of the SRAM monitor. The corresponding parameters for $\sigma(E)$ of the three devices are shown in table 5.12.

Table 5.12: Comparison of Weibull fit parameters with chips characterized by Cecchetto et al. (Cecchetto et al., 2021).

Device	σ_{sat}	E_{thresh}	W	s
SRAM Monitor	$6.5 \cdot 10^{-8}$	1.44	3.36	3.56
Cypress 65 nm (Cecchetto et al., 2021)	$6.5 \cdot 10^{-8}$	0.2	13.08	2.99
ESA Monitor 250 nm (Cecchetto et al., 2021)	$6.5 \cdot 10^{-8}$	0.01	11.57	0.8

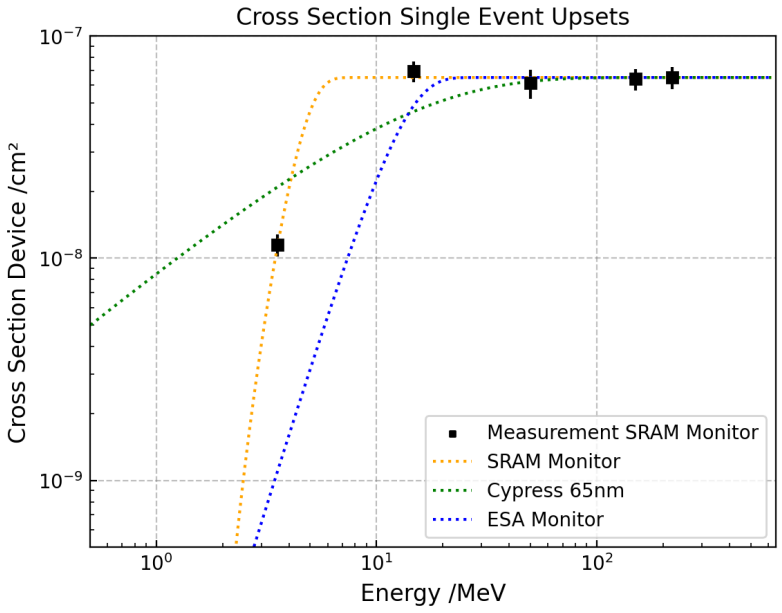

Figure 5.14: Comparison of the characterized Weibull fit with investigations by Cecchetto et al. (Cecchetto et al., 2021).

The Cypress chip as well as the ESA monitor present significantly lower threshold energies for the onset of effects of high-energy neutrons in comparison with the SRAM monitor. Furthermore, the cross section for SEUs for both reference devices only satu-

rates at neutron energies above 10 MeV in comparison with 6 MeV in the SRAM monitor. Therefore, the Cypress 65 nm and the ESA monitor have both a flatter increase in the cross section at intermediate neutron energies in contrast to the SRAM monitor. For further comparison of the three devices, the parameters of the $\sigma(E)$ curves of table 5.12 were used for the intermediate neutron energy weighting function $w_{im}(E)$. Subsequently, the expected number of bit flips for the radiation environment at the Am-Be neutron source at 30 mm distance were calculated for the two reference devices and compared with the measured and calculated bit flips of the SRAM monitor. As a consequence, the effect of different intermediate neutron energy weighting function $w_{im}(E)$ on the expected number of bit flips in a certain radiation environment can be further explored. The results are presented in table 5.13.

Table 5.13: Measured and calculated numbers of bit flips at 30 mm distance to the neutron source of the investigated SRAM Monitor in comparison with the Cypress 65nm chip and the ESA Monitor investigated by (Cecchetto et al., 2021).

Moderator	$N_{measured}$	$N_{SRAM-Monitor}$	$N_{Cypress65nm}$	$N_{ESA-Monitor}$
Air 30 mm	(23 ± 1)	(27 ± 1)	(28 ± 1)	(3.4 ± 0.2)

Although the two intermediate neutron energy weighting functions $w_{im}(E)$ of the Cypress chip and the SRAM monitor strongly differ in their shape and characteristic values, they result in a comparable number of bit flips in the investigated radiation environment. Therefore, the in the measurements determined weighting function for the SRAM monitor is sufficiently reliable to be used in further considerations. Both functions $w_{im}(E)$ may be used to calculate the number of bit flips for SRAMs produced in a 65 nm chip technology.

In contrast, the parameters for the weighting function for the ESA-monitor result in only 10 % of the number of bit flips observed in the SRAM-Monitor. This might be mainly caused by the saturation of the cross section at only 10 Mev neutron energies and a subsequent steep decrease towards lower neutron energies. Since the ESA-monitor chip is produced in a less sensitive and larger chip technology, this was an overall expected result.

Nevertheless, this analysis clarifies that different chip technologies can result in significant differences in the calculation of the expected bit flips for a device. As a result, if the parameters for the weighting function $w_{im}(E)$ cannot be determined experimentally or by simulation for a specific electronic device, they should be chosen from a reference SRAM processed in the same chip technology.

5.8.3 Cosmic Neutrons at Ground Levels

The now validated method for the calculation of the SER in the SRAM monitor in mixed radiation environments was applied to the cosmic neutron spectrum on ground levels. For the determination of the differential neutron fluxes the EXPACS tool by Sato was employed. It generates the neutron fluxes with the PARMA analytical radiation model of the atmosphere which is based on PHITS simulations (Sato, 2015). The cosmic neutron spectrum and consequent SER in the SRAM monitor for New York City on ground during solar minimum activity is presented in figure 5.15.

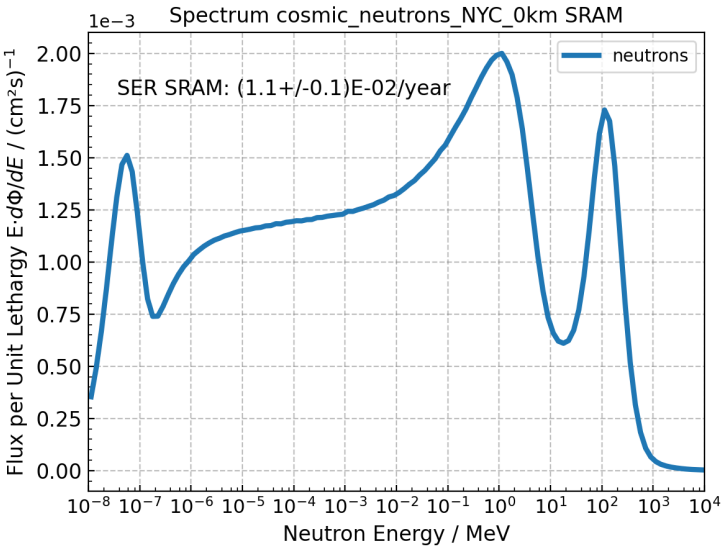

Figure 5.15: Neutron Spectrum for NYC at sea level and the corresponding calculated SER per year.

The SER was estimated with $(1.1 \pm 0.1) \cdot 10^{-2}\,\text{year}^{-1}$. Converted to failures in time per Mb (FIT/Mb), which is defined as the rate of a single failure in 10^9 device hours, a rate of 628 FITs/Mb can be specified for the SRAM monitor on ground in New York City.

The determined rate is compared to the previously presented simplified approach of the JESD89B standard to calculate the SER. For this purpose, the measured high-energy cross section was multiplied by an integrated neutron reference flux above 10 MeV of $3.596 \cdot 10^{-3}\,\text{cm}^{-2}\text{s}^{-1}$. This results in an SER of $(7.4 \pm 0.4) \cdot 10^{-3}\,\text{year}^{-1}$. Provided that the SEU response function is sufficiently accurate, the simplified approach underestimates the SER by 33 % most likely due to the neglect of neutron energies below 10 MeV. Similarly, it has been reported that the 1 MeV to 10 MeV neutrons account for 20 % of all effects by, e.g., Baggio et al., Cecchetto et al.

5.8.4 Cosmic Neutrons at Aviation Altitudes

Similar to the SER on ground levels, the SER at aviation altitudes was calculated using the determined cross sections and weighting functions for the SRAM monitor and the spectral neutron flux calculated with the EXPACS-tool (Sato, 2015). As a reference the differential neutron flux at 12 km altitude at 45° latitude and the longitude of NYC was used as proposed by the IEC standard (IEC, 2016). Additionally, protons above 20 MeV were included in the analysis. The respective neutron and proton energy spectra are depicted in figure 5.16.

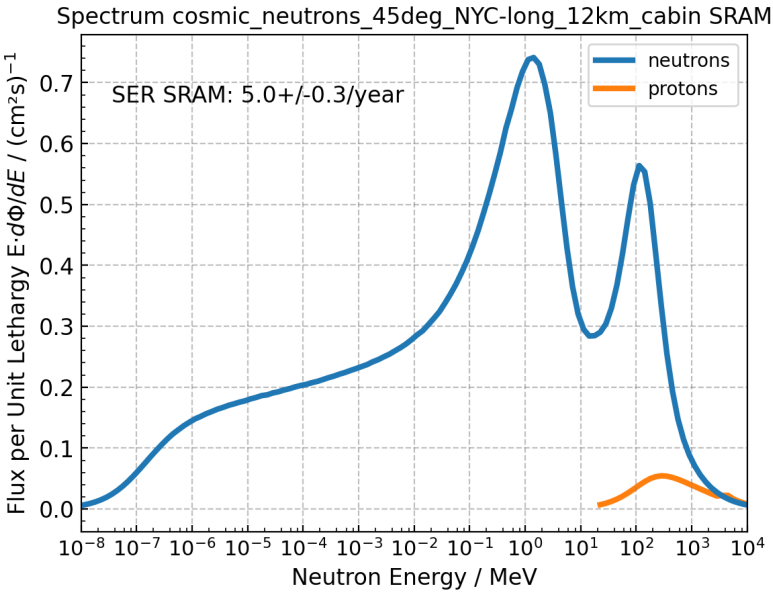

Figure 5.16: Neutron Spectrum at 12 km altitude and 45° latitude at the longitude of NYC and the corresponding calculated SER per year.

A bit flip rate of $(5.0 \pm 0.3)\,\mathrm{year}^{-1}$ was determined for the SRAM monitor. Likewise, this SER was compared to the explained simplified method for the SER calculation at aviation altitudes. Using the standard neutron flux of $6000\,\mathrm{cm}^{-2}\mathrm{h}^{-1}$ the bit flip rate is calculated with $(3.4 \pm 0.2)\,\mathrm{year}^{-1}$. The corrected neutron flux of $9200\,\mathrm{cm}^{-2}\mathrm{h}^{-1}$ for technologies below 150 nm where effects of neutron energies between 1 MeV and 10 MeV are accounted for, leads to an SER of $(5.2 \pm 0.3)\,\mathrm{year}^{-1}$. As a result, the corrected neutron flux is a close approximation for the event rate at aviation altitudes, however, the standard flux underestimates the SER by 32 %. It is therefore evident that for this SRAM type neutron energies between 1 MeV and 10 MeV should be taken into consideration when assessing the radiation effects of neutrons.

5.9 Discussion

With the performed measurements and simulations, it was possible to characterize the response of the SRAM monitor at multiple neutron and proton energies. The comparison with the simulated results showed fairly good agreement. Furthermore, the subsequent application of the determined thermal and high-energy cross sections as well as the SEU cross section curve as a weighting function to the Am-Be-neutron spectrum could sufficiently reproduce the measured values. Therefore, the presented method can be used to estimate the number of bit flips in electronic devices with a similar chip technology in further mixed neutron and proton radiation environments.

The characterized SRAM monitor can also be used for estimating the fluence of monoenergetic neutrons or protons as an SRAM dosimeter. Furthermore, the multiplicity and ratio of MCUs to the total amount of bit flips can be an indication of the underlying nuclear processes inside the silicon. When using the information on the multiplicity of the MCU events, it can be at least qualitatively differentiated if a mixed radiation environment consists of high-energy hadrons.

5.9.1 Limitations

The design of the SRAM monitor and the experimental implementation of the radiation effects testing have several limitations. Firstly, there was no control and monitoring of the power supply during irradiation, resulting in a fixed power supply voltage for the SRAMs in all experiments. It is well-known that there is an influence of the supply voltage on the SEE sensitivity which was not further investigated (Clemente et al., 2018). Moreover, the set-up did not allow for the monitoring of any single event latch-ups which are frequently reported with high-energy hadrons or in heavy ion testing. During static testing, the MCUs could not be discriminated in time. Therefore, all identified MCUs are based on the assumption that a locally delimited accumulation of bit flips is the result of a single impinging particle and that logically neighboring addresses are also physically adjacent. Hence, the number of MCUs could be over-estimated. During dynamic testing, there was a temporal resolution of all events which leads to a higher confidence in the identification of MCUs. However, due to expected high bit flip rates in certain accelerator environments and the corresponding dead-times during read and write operations this method was not always suitable during data acquisition. The SRAM was not tested in a true checkerboard pattern. Although no differences in the occurrence of 0 to 1 and 1 to 0 bit flips could be determined, the different pattern could have influenced the MCU sensitivity due to the differing physical proximity of the 0 and 1.

Moreover, the SRAMs were not tested with a different control system. Hence, it is not known if the measured cross sections for SEUs in the SRAMs are independent of the supporting system. In addition, there can be considerable differences in the sensitivity of

different chips of the same type and manufacturer. A countermeasure was the testing of multiple chips at the same time and averaging their response. However, different chips could lead to different results. Due to limited availability of beam time, it was not always possible to reach the 100 bit flips per chip recommended in the standards for good statistics. However, the total number of bit flips over all chips usually exceeded the recommendation.

In all attempted simulations, the unknown internal device structure is a major limitation. Small variations of the materials and layer sizes inside the chip could considerably alter the results. Furthermore, multiple educated guesses had to be made for input parameters for the simulation, e.g., the sensitive thickness which contribute to considerable uncertainties in the results.

For more sophisticated results, the chips should be further tested with LETs between $1\,\mathrm{MeVcm^2/mg}$ and $5\,\mathrm{MeVcm^2/mg}$ as well as further ion species to improve the fit of the Weibull function in heavy ion testing. Likewise, a test at monoenergetic neutron energies between 1 MeV and 10 MeV, e.g., at 2.5 MeV would be beneficial for data quality and the consequent determination of $\sigma(E)$.

5.10 Conclusion

Despite the considerable limitations, the radiation sensitivity of the SRAM monitor was well-characterized and acceptable parameters for an SEU cross section curve were determined. In further measurements with AIMDs, the device can now be used as a monitor of SEUs at certain fluences which are applied to the medical devices. Moreover, $\sigma(E)$ will be used to weigh the differential neutron energy spectra for the evaluation of the SER of AIMDs in mixed radiation environments. Therefore, only the thermal and high-energy cross section for radiation effects in those devices need to be determined for an evaluation of the reset rate of AIMDs in the cosmic neutron environments.

6. Active Implanted Medical Devices

After the many basic investigations of the SEU sensitivity in SRAMs, radiation effects in the memories of AIMDs and the occurrence of subsequent device resets could be examined. In contrast to the SRAMs, it was not possible to easily obtain direct information on the absolute number of bit flips in most AIMDs at a given fluence. Therefore, a reliability analysis as a method for the calculation of the thermal and high-energy cross section for device resets due to a single particle at a system level is presented. Subsequently, the AIMDs could be tested for their radiation sensitivity at thermal and high neutron energies. Finally, a reset rate in the cosmic radiation environment as well as in proton radiation therapy was finally calculated using the previously presented and validated method for the calculation of the SER in mixed radiation environments.

6.1 Reliability Analysis

When testing the reliability of a device, a Weibull distribution is employed for the determination of a mean time until a failure in the device can be observed. This concept is adjusted to estimate a mean fluence until the first reset in the device is observed and is hereafter described as mean-fluence-to-failure (Clement and Lasky, 2020). The corresponding cumulative Weibull distribution for the proportion of AIMDs having performed a reset and are found in back-up mode p at a certain fluence Φ is thus written as:

$$p(\Phi) = 1 - e^{-\left(\frac{\Phi}{\eta}\right)^{\beta}} \tag{6.1}$$

η describes the characteristic fluence at which 63.2 % of the devices have performed a reset. β defines a slope factor. In general, $\beta < 1$ indicates the early failure of devices, also known as *infant mortality*. This is most probably caused by defective parts or an incorrect design for the intended application. $\beta > 1$ describes *wear-out* failures due to degradation or aging. (Clement and Lasky, 2020) Since SEUs have been found to be random at high as well as at low fluences and a linear relation of the cross section with fluence is presumed, $\beta = 1$ is set. Therefore, the mean-fluence-to-failure equals η. Finally, the cross section for a device reset due to a single impinging particle can be determined using the inverse of the mean-fluence-to-failure. Therefore, it can be written as:

$$\sigma_{device} = \frac{1}{\eta} \tag{6.2}$$

As a result, the percentage of devices being found in back-up mode at a certain fluence is measured and then fitted to a Weibull distribution using the least-square method. From the determined η the cross section for device resets is subsequently calculated.

6.1.1 Uncertainty of the Percentage of Devices in Back-up Mode

The number of devices with an error p as a fraction of all tested devices n in one group was assumed to have an uncertainty of

$$\Delta p_{CIED} = A_{t-test} \cdot \sqrt{\frac{p \cdot (1-p)}{n}} \tag{6.3}$$

for a confidence interval of 1σ. Since the sample size was small, a t-test was performed for the A_{t-test} parameter depending on the degree of freedom of the measurement. A table with the values for A_{t-test} depending on the sample size is shown in the Appendix A.1.

6.2 Intrathecal Infusion Pumps

Before CIEDs were investigated at different neutron energies for the determination of their cross section for device resets, intrathecal infusion pumps were tested for their radiation effects with protons at an energy of 150 MeV. This resulted in a first understanding of the sensitivity of AIMDs to high-energy hadrons. Finally, their response could be compared with the sensitivity of the tested SRAMs. All in all, 8 explanted pumps were provided by the Department of Neurosurgery of the University Hospital Giessen for irradiation. which was performed at the MIT in Marburg in two sessions. One pump was irradiated twice. In preparation for the measurement, the pumps were checked for their functionality and their battery status with the corresponding interrogation device at the University Hospital Giessen.

The devices were placed in front of a water equivalent phantom at 114 cm distance to the extraction window of the proton beam on the patient table. All pumps were exposed to a fluence of $1.1 \cdot 10^9\,\mathrm{cm}^{-2}$. Using an ionization chamber, the applied proton dose was measured in the second irradiation session in July 2023. Figure 6.1 presents a radio chromic film which was placed behind the intrathecal pumps during irradiation. Dark areas represent more proton radiation reaching the film, thus, the big dark square depicts the scanning area of the beam which was 16 cm × 16 cm in this session. Consequently, it can be concluded that the pumps were completely irradiated. The bright areas that resemble the contours of the pumps are the areas where proton radiation was absorbed. The shapes of the batteries are visible towards the center of the irradiation field in each pump (1). The

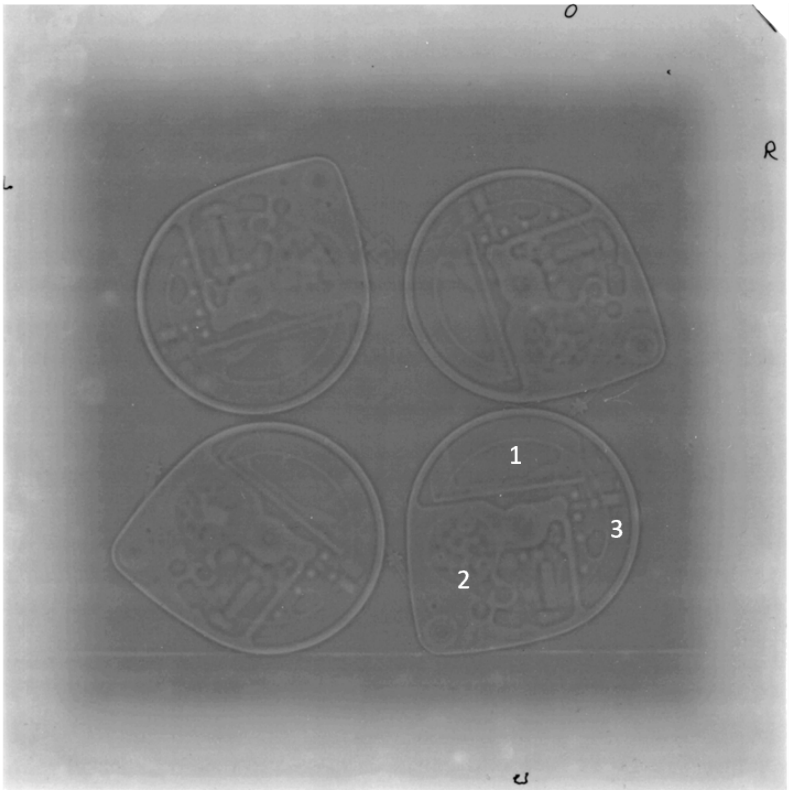

Figure 6.1: Radio chromic film of the irradiation of the intrathecal infusion pumps with 150 MeV protons. (1) marks the battery, (2) shows the peristaltic motor, and (3) the electronics.

peristaltic motor (2) and the electronics (3) can also be well-identified. After irradiation, the pumps were again interrogated and checked for their battery status and functionality. Any differences in the settings were recorded.

The tested devices and their status after irradiation are shown in table 6.1. Out of the 9 test sessions, altered functions were observed in 6 cases. In addition, 5 out of the 6 devices could not be directly reprogrammed and the manufacturer should have been contacted for further trouble shooting. Changes in the battery status were not observed in any of the devices. Two pumps showed the elective replacement indicator (ERI) already before irradiation but since one pump with ERI was fully functional afterwards and one showed a reset, this status might not have a distinct effect on device sensitivity. However, the sample size is too small to take any valid conclusions. The ionization chamber behind the devices measured a dose of 1.111 Gy.

In this experiment with a sample number of 9 tests, the percentage of devices in back-up mode in relation to all investigated devices was 66 %. Referring to the reliability analysis presented in section 6.1, the tested fluence is close to the characteristic fluence where 63 % of the pumps are being found in back-up mode. Therefore, in a rough estimation, the cross section for the effects of high energy protons in intrathecal infusion pumps is

Table 6.1: Tested intrathecal infusion pumps and their response to irradiation.

Model	Status	Remarks
SynchroMed II 8637-40		
SynchroMed II 8637-40	Safe Mode Minimum Flow Rate	-
SynchroMed II 8637-20	Safe Mode Minimum Flow Rate Restart of Pump Underdosing possible	ERI Not Reprogrammable
SynchroMed II 8637-20	Memory Error Settings not available Minimum Flow Rate Restart of Pump Underdosing possible	Not Reprogrammable
SynchroMed II 8637-20		ERI
SynchroMed II 8637-40	Safe Mode Settings not available Memory Error Minimum Flow Rate Underdosing possible	Not Reprogrammable Second Irradiation
SynchroMed II 8637-20	Safe Mode Restart of Pump Minimum Flow Rate	Not Reprogrammable
SynchroMed II 8637-40	Safe Mode Restart of Pump Minimum Flow Rate	Not Reprogrammable Second Irradiation
SynchroMed II 8637-20		

expected on the order of $10^{-9}\,\mathrm{cm}^2$. This is a first glimpse on the sensitivity of AIMDs to high-energy hadrons which might be used for very cautious predictions of failures in certain radiation environments. However, further tests at different fluences with further devices need to be performed to determine the cross section for device resets in more detail. The observed severe effects in the devices at the comparatively low proton dose when referring to the guidelines for radiation therapy, confirm the assumption that the device resets are independent of the absorbed proton dose and most likely the result of the statistical effects of hadronic interactions. Therefore, the effects may be stochastic and not deterministic in nature.

In comparison to the SRAMs, where a high-energy cross-section of $6.5 \cdot 10^{-8}\,\mathrm{cm}^2$ was observed, the intrathecal infusion pumps seem to be 65 times less susceptible to bit flips, assuming that one device reset is caused by one bit flip. This information contributes to specifying the fluences at which medical devices should be investigated in further experiments.

6.3 Cardiac Implanted Electronic Devices

Over a period of several months, pacemakers (PM) and ICDs were collected after replacement and upgrade surgeries at the *Krankenhaus Porz am Rhein*. The devices were then used for the measurement of their sensitivity to particle radiation. Two weeks prior to the irradiation at FNG and EMMA, they were interrogated for their battery status and correct function. Furthermore, standard stimulation settings were applied to each device according to Bjerre, Kronborg, Nielsen, Hoyer, Jensen, Zaremba, Lagdsmand, Sondergaard, Nyström, and Kronborg (2021). The stimulation rate was set to 60 bpm with an output pulse of 3.5 V at 0.4 ms. The pacing mode was either set to ventricular inhibitory pacing (VVI) or dual chamber pacing mode (DDD) according to the device specifications. In ICDs the tachycardia detection zones were programmed to 171/188/229 bpm. Shock therapy was turned off to ensure safe device handling.

Two to four weeks after each irradiation campaign the devices were again interrogated for their functionality. Any severe device corruptions like resets and back-up modes were recorded as well as any changed stimulation parameters and the battery status. Finally, it was checked if the devices could be reinitialized or reprogrammed if they were found in back-up mode.

6.3.1 The Effect of High-Energy Neutrons on CIEDs

Over the course of 5 months, 34 devices of four different manufacturers (14 Biotronik / 4 Medtronic / 15 Abbott-St. Jude / 1 Boston Scientific) could be collected. They were interrogated and programmed to the previously described settings.

The CIEDs were tested with monoenergetic neutrons at 14.7 MeV for the determination of the high-energy neutron cross section for device resets. Although, the assessment with a neutron energy of 14.7 MeV may underestimate the MCU sensitivity of the devices and it may underestimate the high-energy neutron cross section by a factor of two (Clemens et al., 2011; Miller et al., 2013), the results can be used to well-approximate the response in an atmospheric neutron environment (Cecchetto et al., 2021). In addition, the previous SRAM testing showed full saturation of the cross section, already at 14.7 MeV.

Testing took place at the FNG. The 34 devices were divided into three groups of fluences in an even distribution of PMs and ICDs of different manufacturers. The devices

Figure 6.2: Set up of CIEDs at FNG at a radius of 8 cm at 5 cm distance to the target which is behind the acrylic glass plate in this picture.

were placed at a distance of 5 cm to the target at a radius of 8 cm to the center of the target which resulted in a mean flux of $(2.4 \pm 0.7) \cdot 10^6\,\mathrm{cm^{-2}s^{-1}}$ on the device electronics. Therefore, all PMs and ICDs of each group could be irradiated at the same time. The set-up is further depicted in figure 6.2. The previous test results of the SRAM chips, the knowledge of sensitivity of the intrathecal infusion pumps and previous irradiations of CIED, e.g., by Trigano et al., have led to the selection of fluences for device testing. Since it was assumed that CIEDs are less sensitive to particle radiation than intrathecal infusion pumps it was estimated that the characteristic fluence would be around $4 \cdot 10^9\,\mathrm{cm^{-2}}$. Thus, the device groups were irradiated at $8 \cdot 10^8\,\mathrm{cm^{-2}}$, $4 \cdot 10^9\,\mathrm{cm^{-2}}$, and $2 \cdot 10^{10}\,\mathrm{cm^{-2}}$.

The devices were interrogated two weeks after irradiation. All ICDs and their respective response to 14 MeV neutrons are shown in the Appendix A.2, all PMs are described in Appendix A.3. Out of the 34 tested devices, 26 performed resets. In more detail, 17 out of 21 ICDs and 9 out of 13 pacemakers were found in back-up mode. All devices working normally after irradiation were at maximum irradiated with a fluence of $4 \cdot 10^9\,\mathrm{cm^2}$. Looking at the various manufacturers and models, differences become evident. All Biotronik ICDs at any fluence showed an *Implant Error*, meaning they were found in back-up mode. Hence, the stimulation parameters changed to VVI mode with pacing at 70 bpm and 7.5 V at 1.5 ms output. Most of the ICDs were programmed to only one tachycardia zone at OFF/OFF/171 bpm or OFF/OFF/350 ms. However, two devices had OFF/OFF/400 ms as their tachycardia zones. In contrast to all other Biotronik devices, these two could not be reinitialized and reprogrammed to original parameters. For the Medtronic ICDs, only

the device irradiated with the highest fluence indicated a system restart but no changed parameters were identified. Similarly, the ICDs of St. Jude Medical only showed effects at fluences above $4 \cdot 10^9\,\mathrm{cm}^2$. These devices were found in back-up mode (*Back Up VVI*) and the stimulation parameters were set to VVI mode at 67 bpm and an output of 5.0 V at 0.6 ms. No information on the tachycardia zones could be obtained in back-up mode for this manufacturer. However, the log information of the devices still held the originally programmed parameters. Neither of the St. Jude Medical devices could be directly reinitialized on site, therefore, further communication with the manufacturer support would be required for reprogramming.

Looking at the pacemakers, all Biotronik devices showed some form of error. However, the pacemakers which presented a *Data Error* in the first assessment did not show any error messages in the log-file. Furthermore, the stimulation parameters did not change and no reprogramming intervention was necessary. Therefore, it was concluded that this error would not have direct effects on the patient and the devices were regarded as fully functional after the irradiation. In contrast, the device which presented an *Implant Error* also showed the error in the log file and the stimulation output was changed to 3.0 V at 1 ms indicating a full device reset. However, all devices could be reinitialized for further use. The Boston Scientific and Medtronic devices did not show any device resets at the irradiated fluences. In contrast, all St. Jude Medical devices were found in back-up mode and could not be reinitialized directly without the manufacturer's support. The stimulation parameters in back-up mode were changed to VVI mode at 67 bpm and an output of 5.0 V at 0.6 ms.

In general, no changes in the battery status were observed in any of the devices. Furthermore, all CIEDs could be interrogated and could communicate with the device reader although they were in back-up mode.

The results were further analyzed in the reliability analysis. The error bars are the 1σ confidence interval of the fraction of the devices in back-up mode, given a small sample size. The cumulative Weibull distribution shown in equation 6.1 was fitted to the observed proportion of devices in back-up mode for each fluence using the method of non-linear least squares. The corresponding graphs for ICDs and PMs are presented in figure 6.3. Although only three data points were available, an η could be calculated for both types of devices. In both curves the fraction of devices in back-up mode at the second fluence seems to be overestimated which might be the result of the resetting of all tested devices at the third fluence and the corresponding high confidence at the 100 %-value. The analysis results in a fitted mean-fluence-to-failure of $(1.1 \pm 0.3) \cdot 10^9\,\mathrm{cm}^{-2}$ for ICDs and $(1.9 \pm 0.3) \cdot 10^9\,\mathrm{cm}^{-2}$ for PMs. Subsequently, the cross section for a reset in the device was calculated using equation 6.2. The cross-section due to the effects of 14.7 MeV neutrons can be estimated with $(9.1 \pm 2.5) \cdot 10^{-10}\,\mathrm{cm}^2$ for ICDs, and with $(5.3 \pm 0.8) \cdot 10^{-10}\,\mathrm{cm}^2$

for PMs.

Additionally, an analysis of the log files of the St. Jude Medical devices revealed a list of bit flips. Hence, a cross section could be determined by dividing the number of bit flips by the fluence like previously performed with the SRAMs. This revealed a cross section for these specific devices of $6.4 \cdot 10^{-9}$ cm^2 for ICDs and $5.4 \cdot 10^{-9}$ cm^2 for PMs. There is a considerable difference between the results of the reliability analysis and the memory read out of the St. Jude Medical devices. This could be explained by error correcting codes that not every bit flip results in a reset of the device. Furthermore, the reliability analysis presents an average mean-fluence-to failure of several different manufacturers and device types that appear to have different radiation sensitivities. Therefore, this analysis underscores the importance of further investigations with many more devices to compensate for radiation sensitivity differences in individual device types and manufacturers or to investigate them separately.

6.3.2 Thermal Neutrons with CIEDs

For the determination of the thermal neutron cross section for CIEDs, the devices were irradiated at EMMA. Over the course of further 5 months additional 15 explanted devices could be collected. All previously irradiated devices which could be reinitialized and were fully functional were reused. Thus, a total number of 32 devices (18 Biotronik / 5 Medtronic / 5 Abbott-St. Jude / 2 Boston Scientific) were investigated. Two weeks before the measurement campaign, they were checked for their functionality as well as their battery status. In all devices, the previously defined settings were programmed.

The devices were again evenly divided into three groups of fluences. The beam at EMMA only had a size of 6 cm × 6 cm, therefore the CIEDs had to be irradiated individually. After the first measurement with the SRAM monitor, it was concluded that fluences of $2.3 \cdot 10^8$ cm^{-2}, $1.2 \cdot 10^9$ cm^{-2} and $5.7 \cdot 10^9$ cm^{-2} should suffice for observing device resets to back-up mode for analysis. The devices could only be interrogated 4 weeks after irradiation due to device activation and consequent radiation protection measures. As a result, one device reached its end-of-life status and could no longer be interrogated. Furthermore, one device was not irradiated due to a collapse of the primary beam which was only noticed in the log-files after the measurement.

The response to the irradiation with thermal neutrons of the remaining 30 devices is shown in the Appendix table A.4 for ICDs and table A.5 for pacemakers. 9 out of 30 devices were found in back-up mode or performed an electrical reset. Out of the 9 devices with effects, there were 7 ICDs and only 2 pacemakers affected. For Biotronik ICDs, an *Implant Error* was observed in devices at all three fluences, although only one device showed the error at the lowest fluence, three devices at the medium fluence and two devices at the highest fluence. The stimulation settings were again changed to VVI

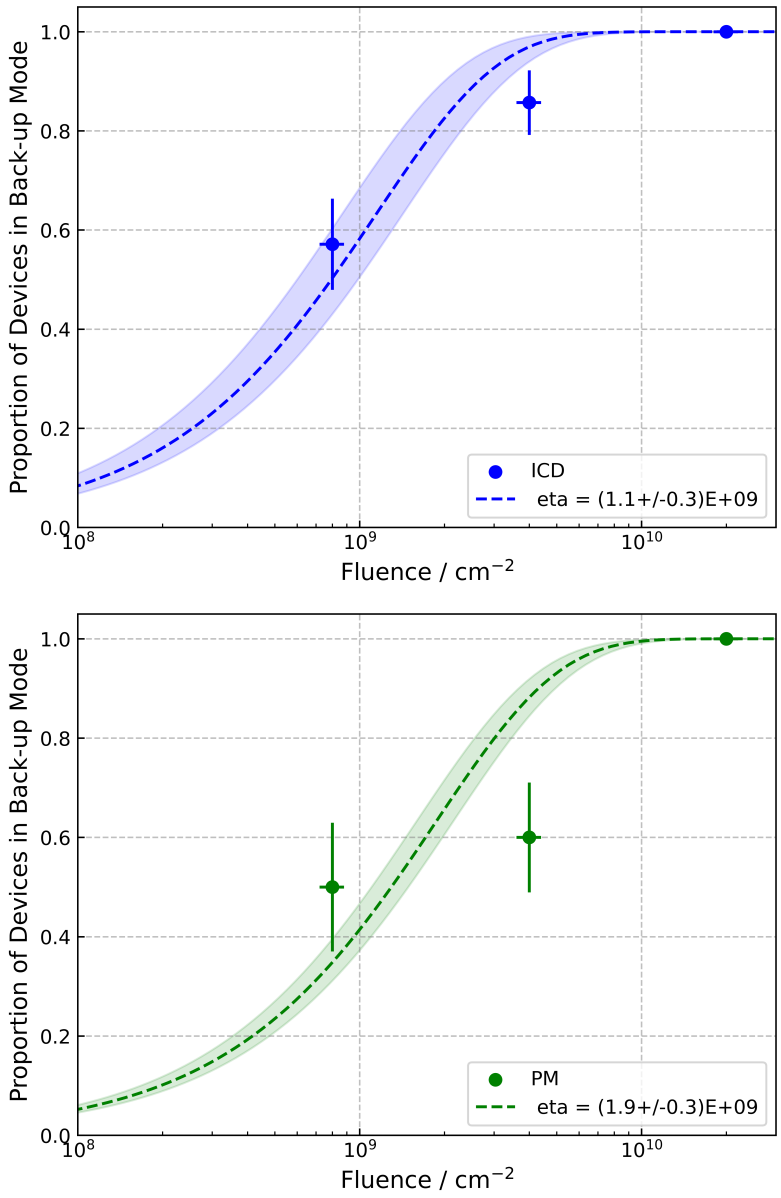

Figure 6.3: Failure curves for ICDs (top) and PMs (bottom) at 14.7 MeV neutron irradiation.

mode with pacing at 70 bpm and 7.5 V at 1.5 ms output. The tachycardia settings were programmed to only a single zone at OFF/OFF/171 bpm. In contrast to the irradiation with 14.7 MeV neutrons, no different settings were found in the tachycardia zones. All devices could be reinitialized. Besides the Biotronik ICDs, only one Medtronic ICD performed a system restart after the highest fluence of thermal neutrons. However, again no change in any stimulation parameter settings was observed. The two devices from Boston Scientific and St. Jude Medical did not show any anomalies.

In the analysis of the pacemakers only two devices produced by St. Jude Medical were found in back-up mode, one after a fluence of $1.2 \cdot 10^9\,\mathrm{cm}^{-2}$ and one after a fluence of $5.7 \cdot 10^9\,\mathrm{cm}^{-2}$. The stimulation parameters changed to VVI-mode with a pacing at 67 bpm and an output of 4 V at 0.6 ms. Similar to the previous measurement, the devices of St. Jude Medical could not be directly reinitialized without the help of a manufacturer representative. In addition, one pacemaker from Biotronik showed a *Battery Error*. However, the battery voltage did not change in comparison to the pre-irradiation check. Since neither changes in the stimulation settings were observed nor a reset or back-up mode was indicated, this device was not regarded as device with an error. Considerable changes in the battery status were not observed in any of the devices.

The results from the thermal neutron irradiation were analyzed in the same way as the 14 MeV neutron irradiation data. The resulting graphs and fits with the cumulative Weibull function for the reliability analysis are depicted in figure 6.4. The mean-fluence-to-failure for ICDs was found to be $(3.0 \pm 0.8) \cdot 10^9\,\mathrm{cm}^{-2}$. Thereof, a cross section of $(3.3 \pm 0.9) \cdot 10^{-10}\,\mathrm{cm}^2$ was calculated. In the first examined fluence the PMs did not show any resets. Therefore, this point was excluded from the fit which resulted in a fit of only two data points. However, a mean-fluence-to-failure of $(2.1 \pm 0.9) \cdot 10^{10}\,\mathrm{cm}^{-2}$ could still be calculated. It results in a cross section of $(4.7 \pm 2.0) \cdot 10^{-11}\,\mathrm{cm}^2$.

6.3.3 Comparison and Significance of Events

With the previously described experiments two cross sections for resets of CIEDs induced by thermal and high-energy neutrons were determined. They are summarized for ICDs and PMs in table 6.2.

Table 6.2: Summary of the thermal and fast cross sections in CIEDs.

Device	σ_{th}/**cm²**	σ_{fast}/**cm²**	**Ratio** σ_{th} / σ_{fast}
ICD	$(2.1 \pm 0.9) \cdot 10^{-10}\,\mathrm{cm}^2$	$(9.1 \pm 2.5) \cdot 10^{-10}\,\mathrm{cm}^2$	(0.23 ± 0.04)
PM	$(4.7 \pm 2.0) \cdot 10^{-11}\,\mathrm{cm}^2$	$(5.3 \pm 0.8) \cdot 10^{-10}\,\mathrm{cm}^2$	0.09 ± 0.01

Differences in the sensitivity to neutron radiation of the different device types are noticeable. In general, it can be observed that the investigated ICDs are more susceptible

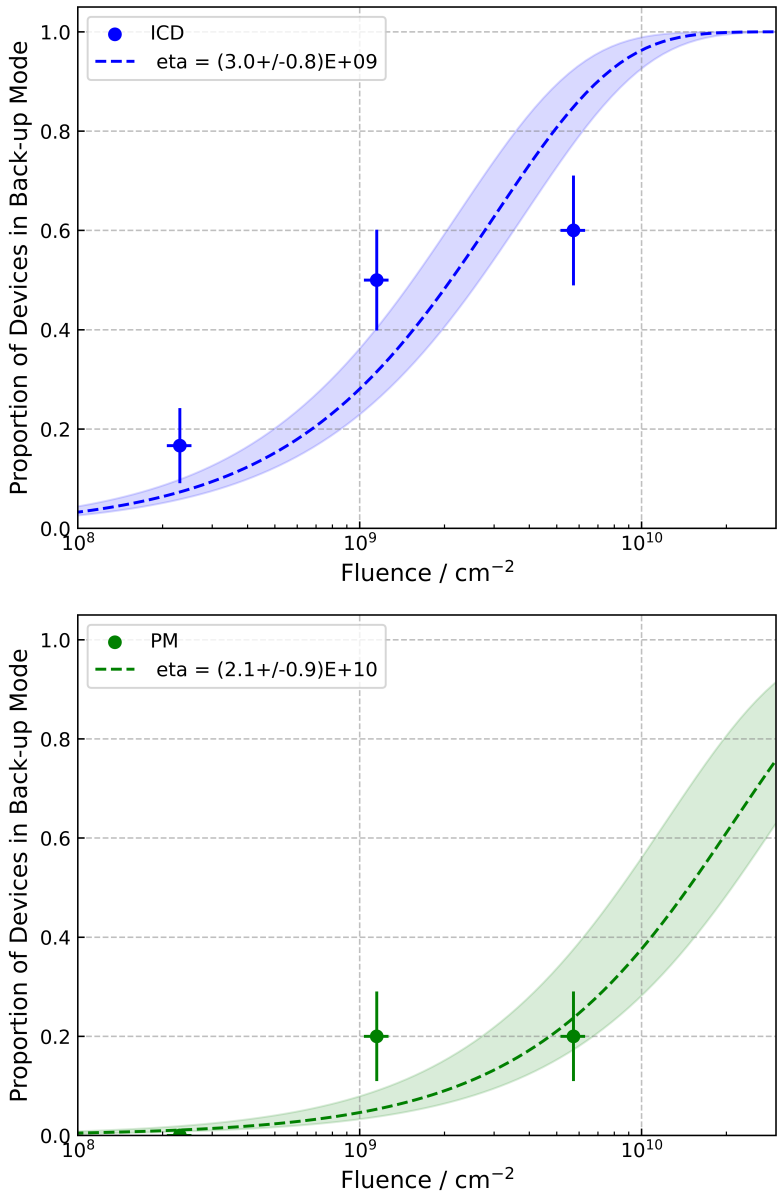

Figure 6.4: Failure curves for ICDs (top) and PMs (bottom) for thermal neutron irradiation.

to neutron radiation than the PMs. Regarding high-energy neutrons, the ICDs are 72 % more sensitive than the PMs, in the measurement with thermal neutrons even a factor of 4.5 was between the sensitivity of ICDs and PMs was determined. Similar findings of a higher risk of device malfunction in radiation therapy in ICDs than PMs have been reported before (Malavasi et al., 2023) and were correlated with more neutron capture reactions in ICDs (Zecchin et al., 2016).

The previously investigated SRAMs with a high-energy neutron cross section for SEUs of $6.5 \cdot 10^{-8}\,\mathrm{cm}^2$, were 71 times more susceptible to high-energy neutrons than the ICDs and 122 times more sensitive than PMs. However, the thermal cross section of

$5.6 \cdot 10^{-10}\,\mathrm{cm}^2$ is only a factor 2.6 greater in the SRAMs than in the ICDs and 12 times greater than in PMs showing a similar sensitivity to thermal neutrons in SRAMs and CIEDs.

Referring to the ratio of σ_{th} / σ_{fast}, the results of the CIEDs with (0.23 ± 0.04) and (0.09 ± 0.01) are in stark contrast to the previous SRAM measurements where a ratio of 0.009 was observed. The ratio for ICDs even exceeds a ratio of 0.2 where Normand et al. concluded that BPSG is most likely present around the sensitive volume. Therefore, environments with an increased thermal neutron flux in comparison to the high-energy neutron flux are much more of concern in the medical devices, particularly in ICDs, than in the tested SRAMs. Severe levels of thermal neutrons were found, e.g., close to the linear accelerator in radiation therapy (Wilkinson et al., 2005). Furthermore, during BNCT therapy, the thermal neutron flux is two orders of magnitude higher than the high-energy neutron flux which would also affect PMs (Koivunoro et al., 2011). As a consequence, the contribution of thermal neutrons to the overall reset rate should not be neglected in the assessment of medical devices in these environments. In contrast, the ratio between thermal and fast fluxes in the atmospheric environment is defined by the standards as 0.5 for ground levels and 1.1 inside aircraft (JEDEC, 2021; IEC, 2016). Therefore, effects from thermal neutrons may be less likely to be observed in the cosmic radiation environment.

Over the course of radiation testing, no complete loss of function was seen in any of the CIEDs. Furthermore, no effects on the battery status were recorded. Therefore, it can be assumed that no deterministic total dose effects were induced and that all effects in the devices can be attributed to stochastic effects of the neutrons.

The observed electrical resets into back-up mode are preprogrammed for the event of a memory error to restore the main function of the CIED. Therefore, device integrity is maintained and the devices can still provide basic therapy and protect patients from sudden death. However, the safety-mode provides only simple pacing with increased output to ensure the capture of the stimulus. This can lead to high battery consumption as well as discomfort for the patient and occasionally to symptoms (Bjerre et al., 2021). Furthermore, in ICDs with only one available ventricular fibrillation zone, limited discrimination for shock-therapy is possible. In rare cases, when the threshold heart rate is set too low, this can lead to inappropriate shocks during exercising or due to oversensing of the sinus rhythm (Philbert et al., 2016). Some devices were locked in the back-up mode and could neither be reinitialized nor reprogrammed. This would require immediate attention and could even result in the acute replacement of the device.

6.4 Estimation of Reset Rate in Different Radiation Environments

Using the determined thermal and high-energy neutron cross sections for device resets and the parameters for the weighting function w_{im} determined with the SRAM monitor

the reset rate for CIEDs in mixed radiation environments can be calculated. Further investigations especially focus on the atmospheric neutron spectrum on ground levels, at aviation altitudes and during severe space weather events. Moreover, the reset rate during proton radiation therapy is determined.

6.4.1 Atmospheric Spectrum on Ground

The differential atmospheric neutron flux for five different cities on ground was extracted from the EXPACS-tool (Sato, 2015) and the corresponding reset rates were subsequently calculated. Similar to the investigations with SRAMs, the rate of radiation induced resets was calculated for New York City during solar minimum activity which serves as reference neutron spectrum for standard values. The cosmic neutron spectrum and the resulting SERs for ICDs and PMs are shown in figure 6.5.

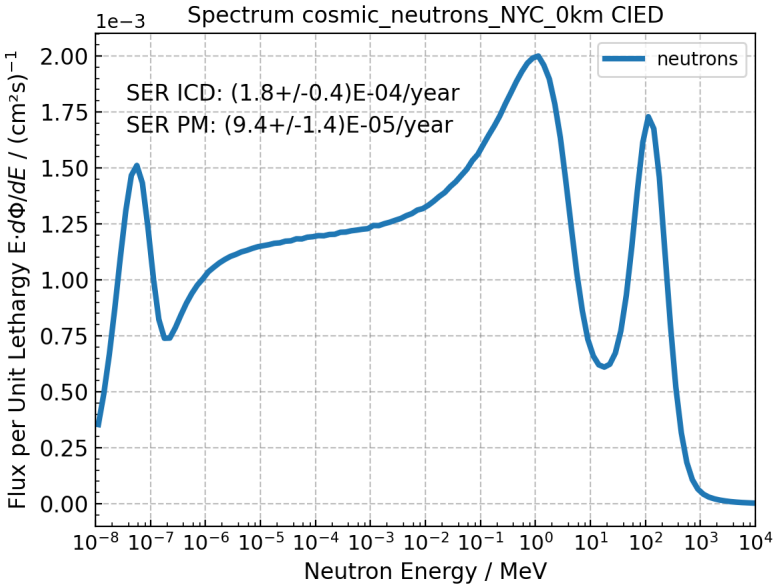

Figure 6.5: Neutron spectrum on ground in NYC and the calculated back-up rate for the CIEDs per year.

The back-up rate was estimated with $(1.8 \pm 0.4) \cdot 10^{-4}\,\mathrm{year}^{-1}$ for ICDs and $(9.4 \pm 1.4) \cdot 10^{-5}\,\mathrm{year}^{-1}$ for PMs. Similar to the SRAMs, these results are compared to the simplified approach of the JESD89B standard. Therefore, the cross section obtained from the measurement with 14 MeV neutrons was multiplied by an integrated neutron flux above 10 MeV of $3.596 \cdot 10^{-3}\,\mathrm{cm}^{-2}\mathrm{s}^{-1}$ (JEDEC, 2021). This results in an SER of $(1.0 \pm 0.3) \cdot 10^{-4}\,\mathrm{year}^{-1}$ and $(6.0 \pm 0.9) \cdot 10^{-5}\,\mathrm{year}^{-1}$, respectively for ICDs and PMs. This is an underestimation of 40 % and 36 % of the calculated rate with the presented method. The observed difference might be the result of effects of neutrons with an energy between 1 MeV and 10 MeV. However, within the uncertainty limits, it appears that the simplified approach approximates the back-up rate in the atmospheric environment

well. In their study with a neutron spallation source, Trigano et al. estimated a failure rate between $1.2 \cdot 10^{-5}\,\text{year}^{-1}$ to $1.2 \cdot 10^{-4}\,\text{year}^{-1}$ for pacemakers at sea level which is consistent with the calculated values for pacemakers.

Further back-up rates for CIEDs in the cosmic neutron environment were calculated for high elevations and geographic locations with high cut off rigidities and consequent high geomagnetic shielding from cosmic radiation. As one example, the city of Denver at an altitude of 1609 m and an R_c of 3 GV was chosen. For comparison, Nairobi at a similar altitude but higher R_c of 14.8 GV was selected. Reykjavik at an R_c of 0.6 GV at sea level as well as Bangkok at 17.5 GV were chosen to account for further effects of the Earth's magnetic field. The results in comparison with the values in New York City which is usually used as reference are shown in table 6.3.

Table 6.3: Comparison of back-up rates on ground at different altitudes and geomagnetic latitudes

Location	Altitude / m	R_c / GV	SER ICD/ year^{-1}	SER PM/ year^{-1}
New York City	0	2.1	$(1.8 \pm 0.4) \cdot 10^{-4}$	$(9.4 \pm 1.4) \cdot 10^{-5}$
Denver	1609	3	$(7.1 \pm 1.7) \cdot 10^{-4}$	$(3.8 \pm 0.6) \cdot 10^{-4}$
Nairobi	1661	14.8	$(3.1 \pm 0.8) \cdot 10^{-4}$	$(1.7 \pm 0.2) \cdot 10^{-4}$
Reykjavik	0	0.6	$(1.8 \pm 0.4) \cdot 10^{-4}$	$(9.8 \pm 1.4) \cdot 10^{-5}$
Bangkok	0	17.5	$(6.9 \pm 1.7) \cdot 10^{-5}$	$(3.7 \pm 0.5) \cdot 10^{-5}$

The calculated rate is 4 times higher in Denver than in New York City due to the higher flux of neutrons with increasing altitude. Similarly, Trigano et al. found a back-up rate increase of a factor 5.6 at 2 km altitude compared to sea level. However, they did not state a geographical location for their results. When comparing the back-up rates at Denver and Nairobi a factor of 2 in the back-up rates between the two cities can be observed. Only minor changes in the back up rates in the lower geomagnetically shielded city of Reykjavik in comparison with New York City can be described. In Bangkok at sea level but a much higher cut-off rigidity, the reset rate is reduced by a factor 2 compared to New York City. Thus, for most people around the globe, the standard calculations may be used for the estimation of the back-up rate, however, people living at higher altitudes may have an increased risk of altered function in their devices.

6.4.2 Atmospheric Spectrum at Aviation Altitudes

At aviation altitudes, the neutron flux is distinctly increased compared to ground level. Furthermore, there is a considerable flux of protons present. Therefore, the back-up rate for CIEDs is expected to be higher. The full neutron energy spectrum and proton flux above 20 MeV of the EXPACS calculations by Sato at 12 km altitude and 45° latitude

were used at the longitude of NYC as proposed by the standard (IEC, 2017). The influence of the thermal neutron flux inside an aircraft is highly discussed. However, the EXPACS tool provides a calculation for a cabin environment which was subsequently used. The result is depicted in figure 6.6. In this configuration, the influence of the thermal neutron flux inside the aircraft is small which contradicts previous studies and the IEC standard (Weulersse et al., 2018; Weulersse et al., 2023). Nevertheless, accurate results for reset rates in this radiation environment are expected with the used spectrum since the thermal neutron cross section for CIED resets is still considerably reduced in comparison to the high-energy cross section.

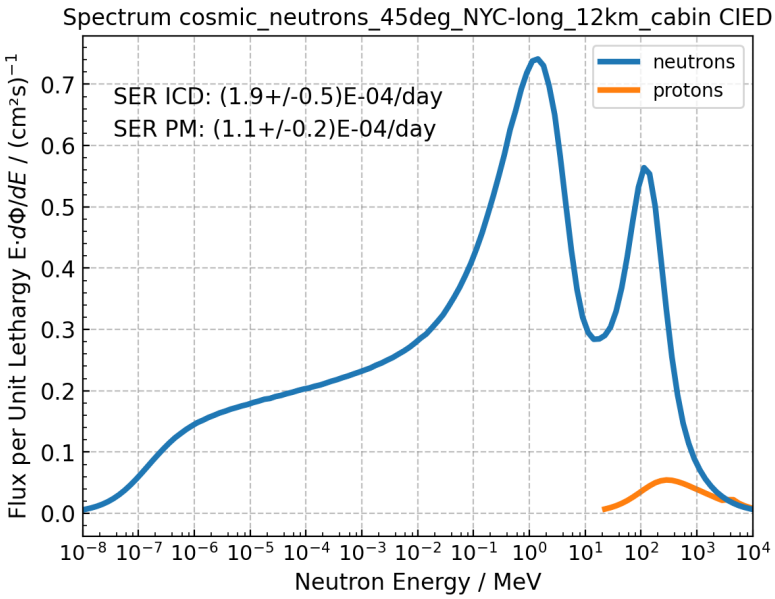

Figure 6.6: Neutron spectrum and proton spectrum above 20 MeV at 12 km altitude and 45° latitude. The calculated back-up rate for the CIEDs is given per day.

A back-up rate of $(1.9 \pm 0.5) \cdot 10^{-4}\,\mathrm{day}^{-1}$ was calculated for ICDs and $(1.1 \pm 0.2) \cdot 10^{-4}\,\mathrm{day}^{-1}$ for PMs. As before, this rate was compared with the simplified model of multiplying the cross section for the high-energy neutrons by a neutron flux of $9200\,\mathrm{cm}^{-2}\mathrm{h}^{-1}$. This assumes that the CIEDs use a technology below 150 nm and are sensitive to neutron energies between 1 MeV and 10 MeV. The simplified approach results in a rate of $(2.0 \pm 0.6) \cdot 10^{-4}\,\mathrm{day}^{-1}$ and $(1.2 \pm 0.2) \cdot 10^{-4}\,\mathrm{day}^{-1}$, for ICDs and PMs respectively which is very accurate to the calculated values.

In addition, calculations of the back-up rate based on parameters for a flight over the pole at 0 GV and 43 000 ft were performed. The reset rate in comparison to the rate of the standard neutron spectrum at aviation altitudes are presented in table 6.4.

There is an increase of 36 % in the reset rate in the polar flight scenario compared to the standard spectrum. In contrast, Trigano et al. estimated a back-up mode rate at 12 km

Table 6.4: Comparison of back-up rates at aviation altitudes for the standard flux and a worst-case scenario at a polar route.

Location	Altitude / ft	R_c / GV	SER ICD / day^{-1}	SER PM / day^{-1}
Standard	40 000	1.8	$(1.9 \pm 0.4) \cdot 10^{-4}$	$(1.1 \pm 0.1) \cdot 10^{-4}$
Polar Flight	43 000	0	$(2.6 \pm 0.7) \cdot 10^{-4}$	$(1.5 \pm 0.2) \cdot 10^{-4}$

with $7.6 \cdot 10^{-6}\,\mathrm{day}^{-1}$ to $7.6 \cdot 10^{-5}\,\mathrm{day}^{-1}$ for pacemakers which might be the result of different cosmic radiation models.

6.4.3 Severe Space Weather Events

For the determination of the effects of severe space weather events on CIEDs, all historically measured GLEs were analyzed. The corresponding neutron spectra were calculated by D. Matthiä using the Geant4 based PANDOCA model for radiation transport in the atmosphere by Matthiä et al. in combination with the solar proton fluence models for solar particle events by Raukunen et al. as input parameters (Personal Communication Matthiä, 2024)(Matthiä et al., 2014; Raukunen et al., 2018). Only the additional component of the solar radiation storm is considered and the calculated neutron spectra do not include the background GCR. Therefore, the calculated SER must be added to the rate in the corresponding cosmic neutron environment. An overview of the back-up rates for all GLEs dependent on the altitude is presented in figure 6.7 for ICDs and PMs.

The three events with the strongest effects on CIEDs, GLE 5, GLE 10, and GLE 69, were selected for further analysis. The back-up rates for the full event were calculated in both device types for different altitudes and two different cut-off rigidities. The corresponding results for both CIEDs are shown in figure 6.8.

GLE 5 presents the highest calculated reset rate of all so far recorded events. On ground at 0 GV a back-up rate of $(9.9 \pm 2.7) \cdot 10^{-7}\,\mathrm{event}^{-1}$ was determined for ICDs while at the highest commercial aviation altitude at 43 000 ft, a rate of $(4.6 \pm 1.2) \cdot 10^{-3}\,\mathrm{event}^{-1}$ was calculated. Looking at the calculations at 1.98 GV which corresponds to the cut-off rigidity near NYC where most of the standards are defined, a back-up rate of $(5.5 \pm 1.5) \cdot 10^{-7}\,\mathrm{event}^{-1}$ on ground and $(4.7 \pm 1.3) \cdot 10^{-4}\,\mathrm{event}^{-1}$ at the highest aviation altitude could be assumed. For ground levels, this is a decrease of about 80 % compared to 0 GV, however, on aviation altitudes it is an order of magnitude lower. Similar results were found for PMs, however, the back-up rate in these devices is generally lower. For 0 GV at 43 000 ft a back-up rate of $(2.6 \pm 0.4) \cdot 10^{-3}\,\mathrm{event}^{-1}$ was calculated for PMs. A comprehensive overview of the detailed rates for ICDs and PMs for GLE 5 and additionally for GLE 10, and GLE69 is given in the Appendix table A.6 and table A.7.

GLE 10 and GLE 69 are considerably weaker in their effects on CIEDs compared to

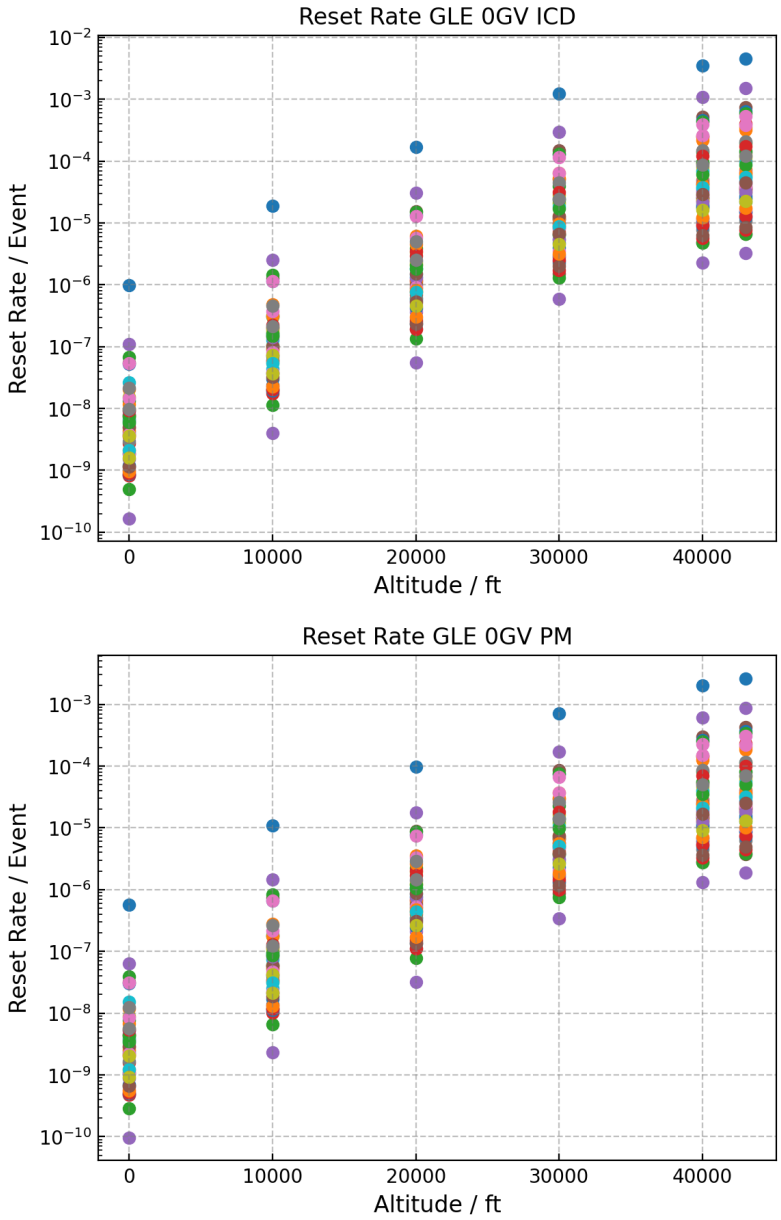

Figure 6.7: Back-up rate for PMs and ICDs at different altitudes for all so far measured GLEs at 0 GV.

GLE 5. Interestingly, they differ significantly in their temporal profile. While GLE 10 is a rather long event with two maxima in neutron flux, GLE 69 shows a short but high peak. As shown in figure 6.8 their overall effect is comparable. However, the probability of experiencing a short but strong event to its full extent at aviation altitudes is higher than a weaker but longer event. Therefore, the GLE 69 seems to be a more relevant event for the assessment of the back-up rate in CIEDs than the GLE 10.

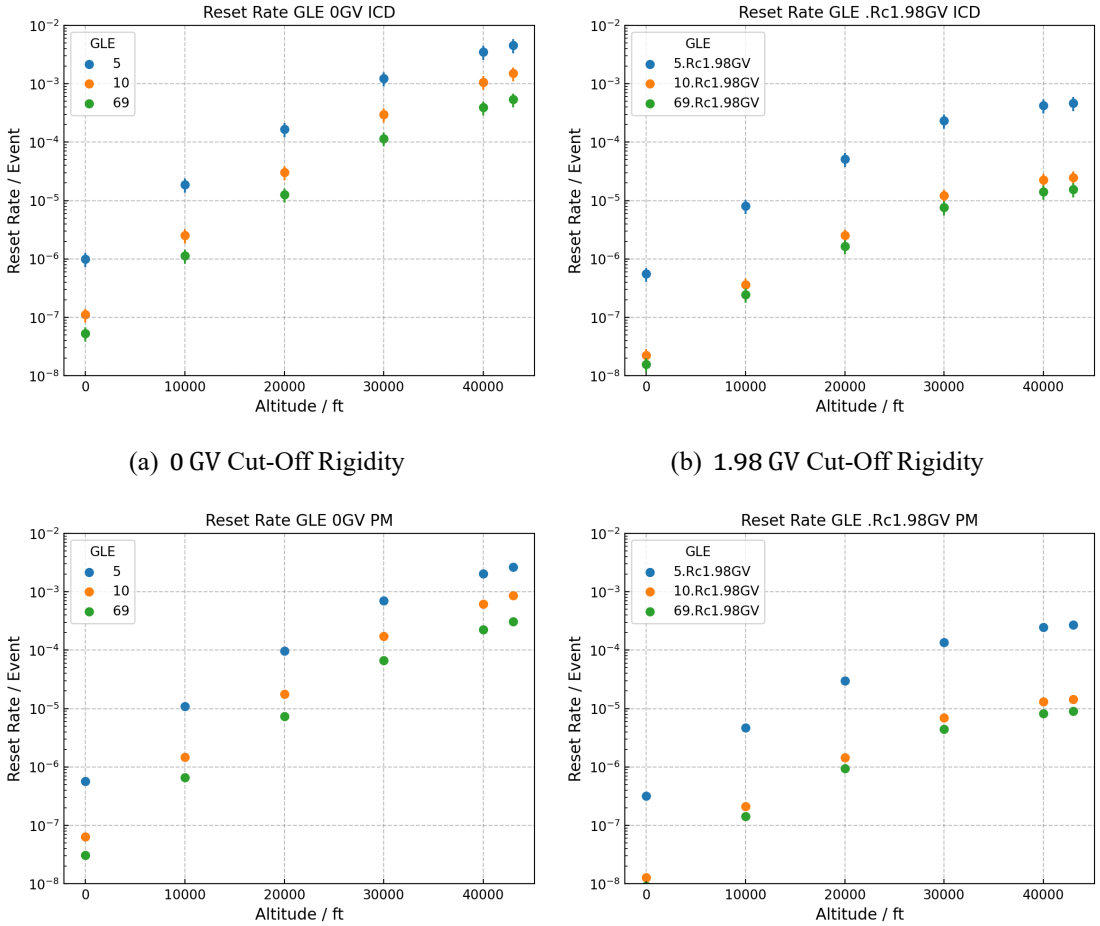

(a) 0 GV Cut-Off Rigidity

(b) 1.98 GV Cut-Off Rigidity

(c) 0 GV Cut-Off Rigidity

(d) 1.98 GV Cut-Off Rigidity

Figure 6.8: Back-Up rate in ICDs (a,b) and PMs (c,d) at different altitudes and cut-off rigidities for GLE 5, GLE 10, and GLE 69.

6.4.4 Proton Radiation Therapy

The secondary neutron spectrum for proton radiation therapy is very complex and difficult to assess. There are usually considerable differences between simulations and measurements due to high measurement uncertainties and limitations in the simulation models. Especially, the secondary neutron spectrum inside a phantom or a patient's body is difficult to determine experimentally and mostly rely on Monte Carlo simulations (De Saint-Hubert et al., 2022). In a first approach to calculate a secondary neutron spectrum which could be used for the determination of the reset rate of CIEDs in radiation therapy, a proton beam with an energy of 130 MeV was simulated in a male ICRP phantom. The calculations were performed by D. Matthiä with Geant4 (Version 11.02.01.1) (personal communication Matthiä, 2024). The neutrons were scored at a sphere surface with a diameter of 4 cm at a distance of 8-12 cm to the isocenter. The resulting secondary neutron spectrum and a reset rate for ICDs and PMs per primary particle at this location is shown

in figure 6.9.

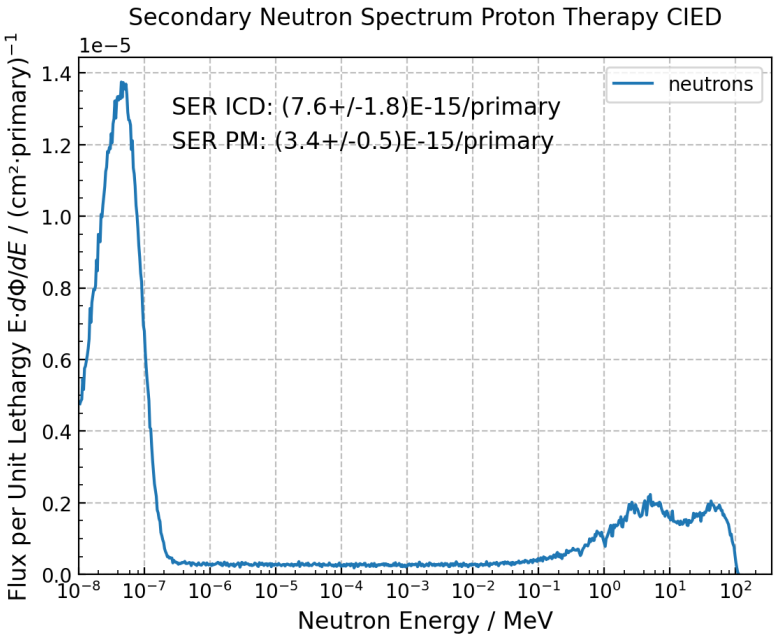

Figure 6.9: Simulation of a neutron spectrum at 10 cm distance to the proton beam.(Personal Communication (Matthiä, 2024)

The neutron spectrum shows a high thermal peak and considerably lower evaporation and high energy peaks. The neutron fluxes in different energy ranges of the neutron spectrum agree well with calculations which were performed by De Saint-Hubert et al., 2022. In contrast to the previous radiation environments, the thermal neutron contribution becomes relevant for the calculations of the reset rate in proton radiation therapy. A rate of $(7.6 \pm 1.8) \cdot 10^{-15}$ primary-1 for ICDs and $(3.4 \pm 0.5) \cdot 10^{-15}$ primary^{-1} for PMs was determined. Depending on the treatment volume, the primary particles needed for 1 Gy can be estimated and multiplied with the reset rate per primary particle.

Finally, the reset rate was exemplarily calculated for a simplified proton radiation treatment plan for prostate cancer. A sketch of the simulation set-up is presented in figure 6.10. A Spread Out Bragg Peak (SOBP) was used in the volume of the prostate in 19-21 cm depth inside the phantom made of water. It was irradiated from the left side. A total number of $2 \cdot 10^{10}$ primary protons were used for a dose of 1 Gy in the therapy volume. The simulations were performed by L. Derksen with the Geant4 based MC tool for radiation therapy TOPAS. The produced neutrons were scored at different distances from the prostate in 48 boxes which were 5 cm × 5 cm × 5 cm. (Personal Communication Derksen, 2024)

The reset rates were calculated for all 48 scoring positions and are shown in figure 6.11 for ICDs and figure 6.12 for PMs. The values are given per Gy in the treatment volume. Secondary neutron spectra for different positions are presented in the Appendix A.2. As

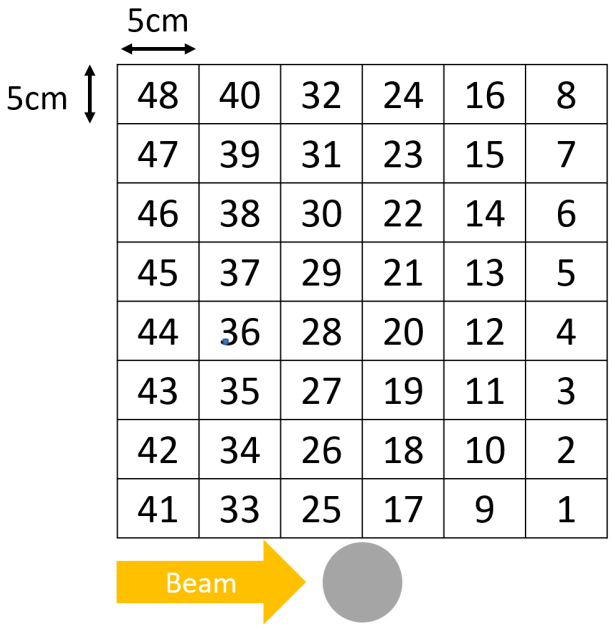

Figure 6.10: Simulation of a prostate cancer proton therapy treatment plan. The gray circle is the equivalent of the treatment volume of the prostate.

expected, the highest reset rates for the devices are in close proximity to the treatment volume directly lateral to the beam path. Here the neutron spectrum is dominated by the fast neutron peak. However, further distant lateral to the beam path, the thermal peak is the most prominent peak of the spectrum, since the fast neutrons were most likely moderated until they reached thermal equilibrium. Distal to the SOBP the thermal peak is equally high or lower as the fast neutron peak. Looking at the different positions from left to right, the maximum value of the fast peak remains constant or even increases. Thus, beginning from 15 cm distance to the treatment volume, the reset rate is higher distal to the SOBP.

Due to the general decrease in the neutron flux with lateral distance from the treatment volume, the reset rate also decreases. At 25 cm distance, the rate has already dropped by two orders of magnitude. The reset rates for ICDs are almost a factor 2 higher than the rates for PMs compared to a factor 1.7 in the cosmic radiation environment. This is most likely explained by the higher sensitivity to thermal neutrons of ICDs.

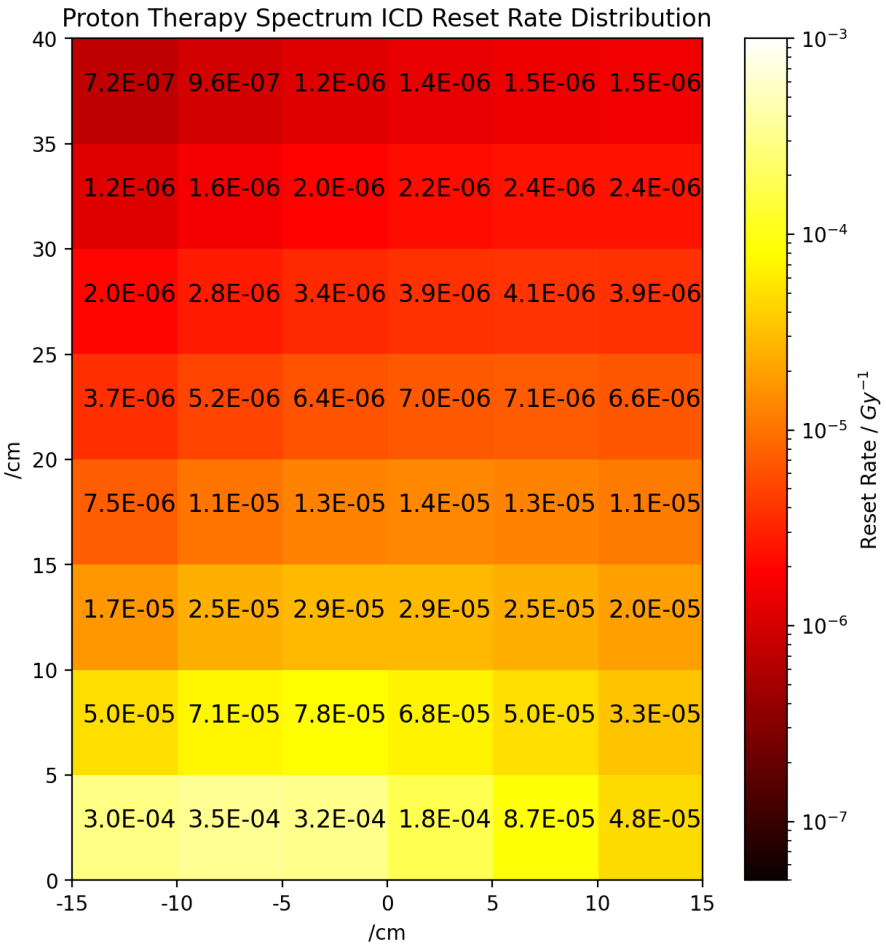

Figure 6.11: Calculated back-up rate for ICDs per Gy in the treatment volume for various distances to the isocenter of irradiation.

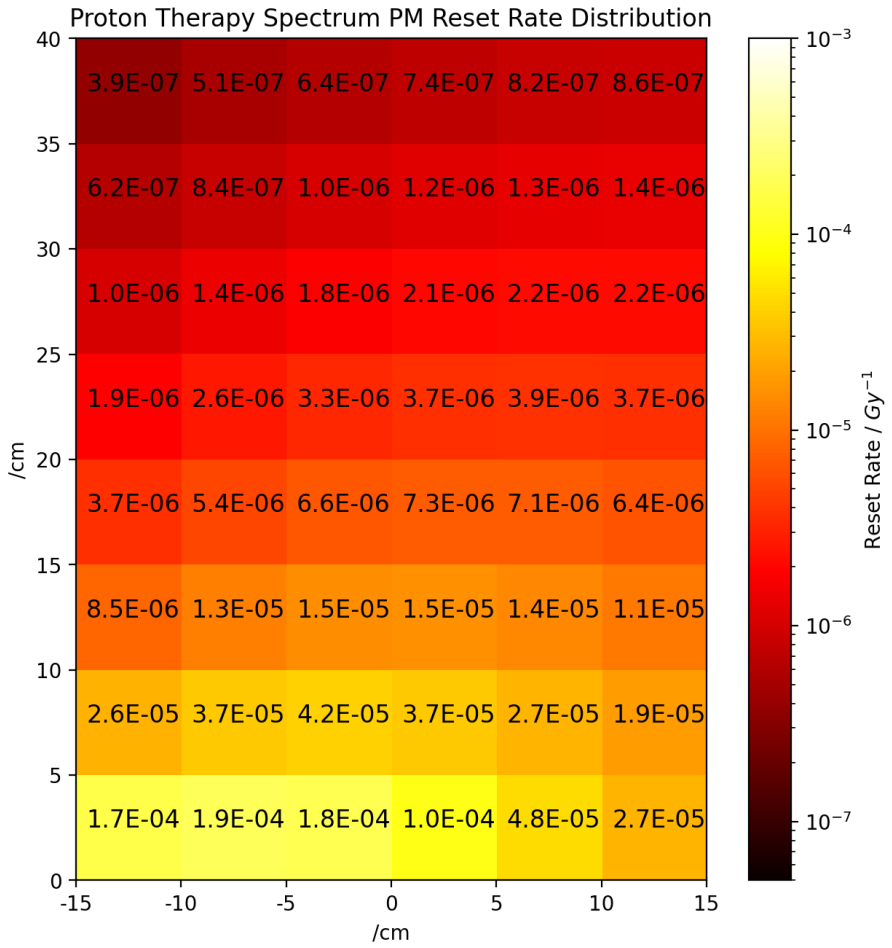

Figure 6.12: Calculated back-up rate for PMs per Gy in the treatment volume at various distances to the isocenter of irradiation.

6.5 Discussion

With the previously described method, rates for CIEDs falling into back-up mode could be determined for mixed radiation environments. For most cases, the event rates are comparably low. Therefore, it is unlikely for the individual patient to experience a device reset due to a cosmic neutron. However, there is an estimated number of 8 to 10 million patients in the world. Assuming the results for the standard neutron spectrum on ground, this would statistically lead to 2 - 3 cosmic radiation induced device reset per day worldwide. This corresponds well to the results observed in the screening of the MAUDE database, assuming that only 20 % of all resets are reported.

Naturally, the number of people with CIEDs who fly is lower. However, due to the higher flux of neutrons at aviation altitudes especially over the poles, the event rate is increased. The calculations result in an odds ratio for a device error of roughly 1 in 5300 for ICDs per day and 1 in 9000 for PMs per day which can be used as a conservative estimation for a return flight from Germany to the US-West Coast. Therefore, such device resets could be occasionally observed after flights as previously described in the case reports.

Severe space weather events which have been reported in the near history do not considerably increase the reset rate on ground. In contrast, at flight altitudes the probability of experiencing a reset during a GLE-5 type event can increase to up to 0.5 % over the whole event for ICDs. However, small variations in flight altitude or geomagnetic latitude can change the probability considerably. Historically, much stronger events have been observed which can be inferred from ice cores and tree samples (Mekhaldi et al., 2015). As described in section 2.2.1, Dyer et al. stated a combined neutron and proton flux above 10 MeV at 40 000 ft at 0 GV during an event occurring once in 150 years could reach $2.5 \cdot 10^7\,\mathrm{cm^{-2}h^{-1}}$ (Dyer et al., 2017). Using the common method of multiplying this value by the high-energy neutron cross section for resets in CIEDs, this results in a back-up rate of $0.02\,\mathrm{h^{-1}}$ for ICDs and $0.01\,\mathrm{h^{-1}}$ for PMs. Thus, several device resets could potentially be observed especially on polar flights during such events.

For atmospheric conditions, testing with neutrons at an energy of 14.7 MeV and using the simplified approach of determining the reset rate in a multiplication by a standard flux, seems to be sufficiently accurate. Thus, the effect of thermal neutrons in the cosmic radiation environment is only minor.

When looking at a full proton therapy treatment plan for prostate cancer of about 70 Gy, the probability of device reset at 5-10 cm distance to the treatment volume 5 cm lateral to the beam path (Pos 33) is estimated with (2.4 ± 0.6) % for ICDs and (1.3 ± 0.2) % for PMs using equation 6.1. However, at 35-40 cm distance, the probability decreases to $(7 \pm 2) \cdot 10^{-3}$ % for ICDs and $(4 \pm 1) \cdot 10^{-3}$ % for PMs. The here presented values are specific for the underlying treatment plan and only give a first impression on the reset rates and consequent probabilities for devices being found in back-up mode during proton

radiation therapy. Depending on the size of the tumor, the applied dose and hence, the number of primary protons, the reset rate changes. In contrast to the assessments in the cosmic neutron spectrum, the thermal neutron fluence becomes more relevant for the determination of the reset rate in proton radiation therapy. The secondary neutron spectrum for proton therapy was simulated in a water cylinder. However, neutrons may be generated and moderated differently in tissue and the size and morphology of the phantom may also influence the secondary neutron production (Vedelago et al., 2024). In the first presented spectrum which was calculated in a phantom consisting of ICRP soft tissue, the thermal peak is much higher in relation to the fast peaks compared to equivalent positions in the proton therapy treatment plan. Although this can also be the result of different models and physical parameters in the simulation, it may also be influenced by the different phantom materials and morphologies.

Accordingly, an individual analysis during treatment planning based on the location and size of the tumor and the consequent neutron spectrum is necessary for the calculation of the reset rate in CIEDs. In conclusion, further research is necessary to further evaluate the influence of the distance of the device to the tumor, position inside the body, and the treatment plan on the reset rate in more depth.

6.5.1 Limitations

The performed analysis has several limitations. Firstly, there was only a small number of devices available on which the measurements and subsequent analysis are based. This leads to a considerable measurement uncertainty. The dataset is rather inhomogeneous with different device types and manufacturers which all could have different sensitivities to neutron radiation. Furthermore, only three fluences could be evaluated due to the limited number of devices. With more data points the reliability analysis may be more precise. Finally, it is not known which chip technology size was used for the memory elements in the medical devices. Due to the previously discussed effects of the chip technology on the radiation sensitivity of the device to intermediate neutron energies, the use of the parameters determined with the SRAM parameters might not be adequate for the calculation of reset rate in CIEDs. This might result in a great uncertainty of the response of the CIEDs to neutrons with energies between $1\,\mathrm{MeV}$ and $10\,\mathrm{MeV}$.

6.6 Conclusion

Despite the limitations, the response of CIEDs in different neutron radiation environments was characterized. This enables for a risk analysis for potential severe malfunctions during air travel or radiation therapy. Consequently, radiation protection measures for people relying on CIEDs can be applied.

7. Discussion

The main objective of this thesis was to develop a method for the prediction of AIMD resets to back-up mode in several radiation environments for scientifically informed discussions about the risk of patients and possible radiation protection measures. Therefore, the cross sections for resets due to thermal and high-energetic neutrons were measured. Additionally, an energy dependent cross section function $\sigma(E)$ for single event upsets based on measurements of basic SRAM chips with monoenergetic proton and neutron radiation was determined. Using both results, the probability of device resets on flight altitudes and further terrestrial neutron radiation environments was analyzed. However, the consequences of the observed changes of device status need to be further discussed for the estimation of risk for people with active implanted medical devices.

Several device manufacturers issued technical reports about the effect of therapeutic radiation on their devices. Solely one manufacturer informs about the possibility of device resets due to cosmic radiation (Medtronic CRM Technical Services, n.d.). Boston Scientific describes that although their device memories have error-correction mechanisms included, the device will enter the back-up mode if the damage is beyond the capability of correction. The devices then still provide basic function, however, a replacement is recommended if it is deemed appropriate for the patient (Boston Scientific, 2012). Biotronik also describes the back-up mode caused by radiation as a safety feature which is not always associated with a malfunction of the device (Biotronik, 2019). Similarly, Medtronic states that a back-up mode does not involve damage in the device but makes further interrogation of the device necessary (Medtronic CRM Technical Services, 2013).

Consequently, the back-up or safety mode should ensure basic care and protection for the patient while the device might be damaged. However, the preprogrammed parameters in safety mode might not be appropriate for all patients. Therefore, several side effects can occur. There can be a loss of cardiac synchrony between the atrium and ventricle or between both ventricles due to the single chamber ventricular pacing (Boston Scientific, 2023). This is also described as the pacemaker syndrome and may lead to a reduction in cardiac output and back pressure into the venous system. The possible unipolar sensing in the back-up mode is associated with pacemaker inhibition due to myopotential oversensing (Burgemeestre and Timmer, 2022). In this case, electrical potentials from skeletal

muscles are falsely sensed as cardiac activity leading to an inhibition of the pacemaker. Especially in patients who are pacemaker-dependent, this could lead to syncopes. Finally, due to the altered stimulation settings to high stimulation amplitudes, there can be extracardiac stimulation of skeletal muscles or the phrenic nerve (Boston Scientific, 2023). Inappropriate shocks due to false detection of tachycardia have been reported in back-up mode in ICDs which caused severe pain and mental distress (Philbert et al., 2016).

It is important to note that not all patients experience the potential side effects from the altered stimulation. Nevertheless, device resets into back-up mode require timely attention in particular if the described symptoms occur. This may be easy to apply if the reset was caused by radiation therapy where the patient is under close medical surveillance. However, effects caused by cosmic radiation during air-travel might not be as simple to deal with. In the worst-case, suddenly occurring symptoms caused by device resets during flights could potentially lead to a diversion of the plane.

7.1 Risk Assessment

With the calculated probabilities of device resets and the descriptions of the potential effects on patients, a risk assessment for the exposure to particle radiation can be proposed. The standard ISO14971:2019 for the application of risk management to medical devices defines risk as the ”combination of the probability of the occurrence of harm and the severity of that harm” (ISO, 2019b). For the analysis, severity scales (table 7.1) and occurrence levels (table 7.2) need to be defined for the specific purpose. The occurence rates are defined for an individual patient and is frequently given as examples according to ISO14971:2019.

Table 7.1: Definition of the Severity Scale.

Severity	**Description**
Negligible	Inconvenience and temporary discomfort
Minor	Temporary injury or impairment not requiring medical or surgical intervention
Major	Injury or impairment requiring medical or surgical intervention
Critical	Permanent impairment or irreversible injury
Fatal	Death

Furthermore, a risk evaluation matrix needs to be defined which is shown in table 7.3. The chosen risk classes are based on a risk strategy for radiation therapy presented by Klüter et al. and are focused on implementing high patient safety. It depicts three different risk classes: low (green), medium (yellow), and high risk (red). The low risk

Table 7.2: Definition of the Risk Occurence Scales.

Description	**Occurence Rate**
Frequent	≥ 0.1
Probable	$\geq 0.01 and < 0.1$
Occasional	$\geq 10^{-3} and < 0.01$
Remote	$\geq 10^{-4} and < 10^{-3}$
Improbable	$< 10^{-4}$

class assumes that the risk is generally acceptable while in the medium risk class the risk is only acceptable if the risk is "as low as reasonably achievable" (ALARA-principle). The high risk class is not acceptable and further risk control measures need to be implemented. (Klüter et al., 2021)

Table 7.3: Risk Acceptance Matrix with the defined occurrence levels. Adapted from Klüter et al., 2021.

Probability	Negligible	Minor	Major	Critical	Fatal
Frequent					
Probable					
Occasional					
Remote					
Improbable					

The process of risk assessment according to the standard is presented in figure 7.1 (ISO, 2019b). First, a hazard must be identified which is in this case the exposure to a particle radiation environment. Subsequently, the occurrence of a reset to back-up mode in the CIED is defined as the hazardous situation. A probability $P1$ can be defined which was deduced from the reliability analyisis for several hazardous situations in the previous chapter. Finally, harm is characterized as the "... injury or damage to the health of people ..." (ISO, 2019b) and a probability $P2$ for its occurrence must be determined. Harm was defined as the effect of back-up or safety mode on the patient in this assessment. Patients who experience a reset to back-up mode always need interrogation and reprogramming of their devices and should hear an alarm tone which can induce psychological side effects. Therefore, the severity of the event is classified as minor if the patient does not show any other symptoms. However, as described in the previous section a back-up mode can be associated with several side effects and even the exchange of the device. Then the severity level would change at least to major since medical or surgical intervention is needed. Depending on the symptoms or the dependency on the CIED, the severity level might even

be worse. Since the probability for the occurrence of symptoms which are associated with the back-up mode is not known, the risk can only be estimated downward. For the best case, the probability of occurrence of harm is set to $P2 = 1$ with a severity level of minor.

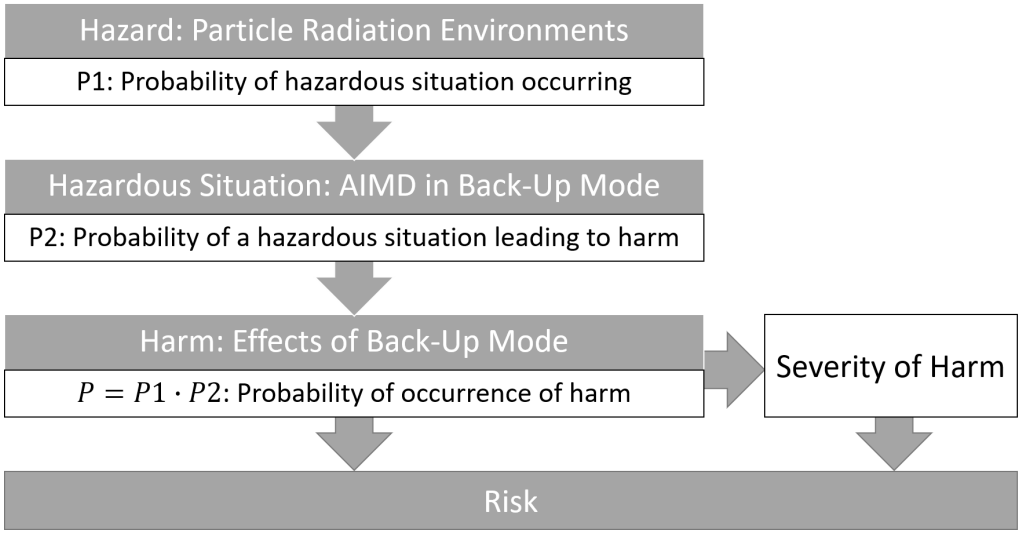

Figure 7.1: Schematic drawing of the risk assessment process according to ISO14971:2019 (ISO, 2019b).

Table 7.4 shows probabilities of the occurrence of harm for some examples of the investigated radiation environments and the associated risk levels according to the risk evaluation matrix in table 7.3. The chosen examples represent the highest potential reset rates of each scenario. Therefore, the risk assessment is based on a ”worst-case” analysis.

Table 7.4: Probabilities of harm for ICDs in different situations and the according risk level.

Radiation Environment	Device	Probability of Harm	Risk Level
Living in NYC for a year	ICD	$(1.5 \pm 0.4) \cdot 10^{-4}$	Medium
	PM	$(8.3 \pm 1.2) \cdot 10^{-5}$	Low
Polar Return Flight	ICD	$(2.3 \pm 0.6) \cdot 10^{-4}$	Medium
	PM	$(1.3 \pm 0.2) \cdot 10^{-4}$	Medium
GLE5-Type Radiation Event at 43 000 ft	ICD	$(4.7 \pm 0.4) \cdot 10^{-3}$	Medium
	PM	$(2.7 \pm 0.4) \cdot 10^{-3}$	Medium
Radiation Therapy Treatment at 5 cm lateral to the beam in 5 cm distance to the tumor (Pos 33)	ICD	$(2.4 \pm 0.6) \cdot 10^{-2}$	Medium
	PM	$(1.3 \pm 0.2) \cdot 10^{-2}$	Medium

For the cosmic radiation environment on ground, a low risk for PMs and medium

risk for ICDs could be identified over a one year period. For a polar return flight, e.g., from Germany to the US West Coast which equals roughly a day, a medium risk in a conservative estimation was determined. Although the probabilities for resets are higher, a full GLE5-type radiation event at aviation altitudes at 43 000 as well as a full course of radiation therapy with the tumor being 5 cm from the device, still pose a medium risk for effects on the patient. Therefore, in all scenarios the risk is deemed acceptable if it is as low as reasonable achievable. However, it has to be kept in mind, that the results are only a downward estimation of the risk based on a small and diverse sample size of devices. Further research is needed to more accurately calculate the reset rates for CIEDs in certain radiation environments. Furthermore, the risk might change if the probabilities for different side effects of the back-up mode are further assessed which might increase the severity level to major in some cases.

7.2 Radiation Protection Measures

In general, the standard suggests to keep the risk as low as reasonably practicable in the ALARP concept (ISO, 2019b). However, it is difficult to effectively shield patients from neutrons which primarily cause the effects. Therefore, reducing the exposure to neutrons as much as possible is the most effective protection from single event effects in CIEDs. It was found that during extreme solar radiation events, a lower altitude in the atmosphere can decrease the rate of resets in devices considerably. Consequently, it may be advised to fly lower to protect patients with CIEDs from medical emergencies when neutron fluxes exceed a certain level during such extreme space weather events (Matthiä et al., 2015).

In general, the probability for incidents at aviation altitudes are remote for the individual and a medium risk was identified. Prudent advice for patients willing to fly might be necessary to avoid any uncertainties. Still it could be given a cautious recommendation to have the devices checked soon after long-haul flights to detect any changes early on.

Concerning the therapeutic use of radiation, the guidelines already suggest the avoidance of neutron-producing radiotherapy in patients with CIEDs which is supported by the previous findings. In cases where neutron production cannot be avoided, e.g., in proton radiation therapy, the detailed analysis of the secondary neutron spectrum at the location of the device may help to assess the risk of malfunction to weigh up a decision for or against the method of therapy.

Some of the manufacturers for CIEDs suggest that radiation therapy is contraindicated in patients with implanted devices since normal device functionality cannot be guaranteed at therapeutic levels of radiation (Biotronik, 2019; St. Jude Medical Technical Services, 2016). However, certain precautions like no direct irradiation and a minimization of the cumulative dose on the device are recommended to reduce the risk (Biotronik, 2019). In any case, they all agree on close monitoring of the patient during and after the treatments

to detect any device alterations. Dose limits which can be applied to the devices are heavily discussed in scientific literature (ref to section 3.1.3) and among the manufacturers. While Boston Scientific does not define a safe therapeutic radiation dose, Biotronik recommends device relocation above a cumulative incident dose of 5 Gy (Boston Scientific, 2012; Hayes, 2024). Medtronic defines dose limits between 1 Gy to 5 Gy depending on the device type before damage to the devices may occur (Medtronic CRM Technical Services, 2013). St. Jude Medical does also not define any dose threshold for device damage. However, when testing the devices with an X-ray source, they did not see any effects up to a cumulative dose of 30 Gy (St. Jude Medical Technical Services, 2016).

Based on the previous findings, it has to be distinguished between cumulative dose effects from the applied radiation and resets due to single event effects caused by neutrons. While the dose recommendations of the manufacturers might refer to the deterministic effects in devices, there is no safe dose for the stochastical effects of neutrons. The only way of effectively protecting patients from single event effects is the reduction of the neutron flux at the location of the device.

In conclusion, it is important that medical personnel is aware of the effects of cosmic radiation and therapeutic radiation in medical devices and of the necessity to minimize the exposure to neutrons.

7.3 Outlook

In further investigations, the calculated reset rates for specific radiation environments need to be validated. Therefore, several CIEDs could be exposed to a simulated treatment of radiation therapy with a fully characterized secondary neutron field. The observed fraction of devices with resets should be compared with the prior calculated value to determine the accuracy of the model.

Although the results are satisfactory and a first calculation of reset rates could be performed, further measurements with more devices should be attempted in the future for a more sophisticated prediction of device resets. Thus, differences in the radiation sensitivity of pacemaker and ICD models as well as manufacturers could be further explored. Moreover, the presented method can be applied to additional implanted medical devices such as neurostimulators, infusion pumps, or cochlear implants. However, the effects of resets on the patient in these devices might not be as severe as in cardiac devices.

Additionally, further radiation environments might be interesting to explore. Especially in radiation therapy, there are many more conditions which could be investigated, e.g., treatments involving photon radiation, or heavy ion-radiation. It would be interesting to further characterize the effect of beam energy, treatment planning and position of the devices toward the isocenter of radiation on the probability of malfunction. However, adequate simulations of the secondary neutron spectrum under the different conditions are

necessary.

With the increase of commercial spaceflight and eventually space tourism, the question if patients with implanted CIEDs are suitable for space flight arises. Reyes et al. discuss the effects of suborbital and orbital flights on implanted medical devices based on a literature review on the effects of radiation on these devices. They conclude that suborbital flights should not pose any more risks for patients than cross-country flights and short orbital flights may be possible as long as several precautions and preparations are made (Reyes et al., 2014). However, they just compare the absorbed doses in these radiation environments with limits which have been considered acceptable in radiation therapy. Although the radiation environment in space differs considerably from the investigated radiation environments in the atmosphere, a rough estimation of the reset rate on a suborbital or orbital flight might be possible when only considering the effects of hadrons above 20 MeV. Depending on the results, it could be decided if patients with CIEDs might even fly to space in the near or far future.

8. Conclusion

The reset rate of pacemakers and ICDs could be determined for several radiation environments. The major finding is that the probability for the individual patient for experiencing such an event due to cosmic radiation on ground is remote. However, looking at the total number of patients worldwide, a not negligible number of events may be observed. At aviation altitudes, there could be occasional events especially at polar flights on high altitudes. Since the number of passengers having an AIMD is not known but expected to be just a fraction of the total number of patients with implanted devices, incidents are overall expected to be rare. Nevertheless, medical personnel should be aware of the possibility of resets during or after flights. During extreme solar radiation events with elevated neutron fluxes at aviation altitudes frequent effects might be observed. Hence, it should be aimed for the development of accurate and reliable predictions of the radiation in the atmosphere during such events to apply consequent protection measures at aviation altitudes. Current radiation therapy guidelines mostly focus on cumulative doses in the devices and the avoidance of neutron production during irradiation for accurate treatment planning. However, for the safe irradiation of patients with AIMDs, it is crucial to accurately estimate the secondary neutron radiation field at the location of the device which is a starting point for further research.

Overall this thesis proofs that neutrons affect active implanted medical devices, however, with a detailed assessment of the various radiation environments, radiation protection measures can be applied to protect patients from adverse events.

9. Publications and Conference Contributions

Conference Contributions

- **Plettenberg, M.C.**, M.M. Meier, K. Schennetten, D. Matthiä, M. Wirtz (2021) Effekte von Weltraumwetterereignissen auf aktive implantierte Medizingeräte. 5. Nationaler Weltraumwetterworkshop 2021, 22.09.2021, online. Oral Presentation

- **Plettenberg, M. C.**, M.M. Meier, K.Marsalek, K. Schennetten, H.G. Zaunick, K.T. Brinkmann (2022) Are Cosmic Neutrons a Threat to Pacemakers? - Testing SRAMs with an Am-Be Neutron Source. SEE/MAPLD 2022, 2022-05-15 - 2022-05-19, San Diego, USA. Poster Presentation

- **Plettenberg, M. C.**, M.M. Meier, K. Marsalek, K. Schennetten, H.G. Zaunick, K.T. Brinkmann (2022) Testing an active control device for bit flips in neutron and heavy ion radiation environments. SERESSA 2022 18th International School on the Effects of Radiation on Embedded Systems for Space Applications, 2022-12-05 - 2022-12-09, Zurich, Switzerland. Poster Presentation

- **Plettenberg, M.**, M.M. Meier, K. Schennetten, H.G. Zaunick, K.T. Brinkmann (2023) Entwicklung einer Methodik zur Unterschuchung der Ausfallrate von aktiven implantierten Medizingeräten auf Reiseflughöhen. 61. Jahrestagung der DGLRM, 2023-10-19 - 2023-10-21, Cologne, Germany. Poster Presentation

- **Plettenberg, M.C.**, E. Berenjkoub, D. Matthiä, K. Schennetten, H.G. Zaunick, K.T. Brinkmann, M.M. Meier (2023). Radiation Effects on Pacemakers and Implanted Defibrillators During Increased Space Weather Activity. Mini-ISWAT Meeting European Space Weather Week, 2023-11-18 - 2023-11-19, Toulouse, France. Oral Presentation

- **Plettenberg, M.**, F. Schwarm, H.-G. Zaunick, M.M. Meier, M. A. Kolodziej, E. Uhl, K.-T. Brinkmann (2024) The Impact of High Energy Proton Radiation on Intrathecal

Infusion Pumps. 75. Jahrestagung der Deutschen Gesellschaft für Neurochirurgie, 2024-06-09 - 2024-06-12, Göttingen, Deutschland. Poster Presentation

- **Plettenberg, M.C.**, E. Berenjkoub, D. Matthiä, K. Schennetten, H.G. Zaunick, K.T. Brinkmann, M.M. Meier (2024). Effects of Cosmic Radiation on Cardiac Implanted Electronic Devices. 48th European Radiation Research Society Meeting, 2024-09-10 - 2024-09-13, Aveiro, Portugal. Oral Presentation

- **Plettenberg, M.C.**, D. Matthiä, K. Schennetten, K.T. Brinkmann, M. M. Meier (2024) Effekte starker solarer Strahlungsereignisse auf die Funktion von Herzschrittmachern und implantierten Defibrillatoren. 6. Nationaler Weltraumwetterworkshop, 2024-09-24 - 2024-09-26, Neustrelitz, Germany. Oral Presentation

Co-Author in Publications

- Meier, M. M., K. Copeland, K.E.J. Klöble, D. Matthiä,**M.C. Plettenberg**, K. Schennetten, M. Wirtz, C.E. Hellweg (2020) Radiation in the Atmosphere—A Hazard to Aviation Safety? Atmosphere, 11 (12), Page 1358. Multidisciplinary Digital Publishing Institute (MDPI). doi: `10.3390/atmos11121358`. ISSN 2073-4433.

- Meier, M. M. , T. Berger, T. Jahn, D. Matthiä,**M.C. Plettenberg**, M. Scheibinger, K. Schennetten, M. Wirtz (2023) Impact of the South Atlantic Anomaly on radiation exposure at flight altitudes during solar minimum. Scientific Reports, 13 (1), Page 9348. Nature Publishing Group. doi: `10.1038/s41598-023-36190-5`. ISSN 2045-2322.

A. Appendix

A.1 Bit Flips over Time at the AmBe Neutron Source with Moderators

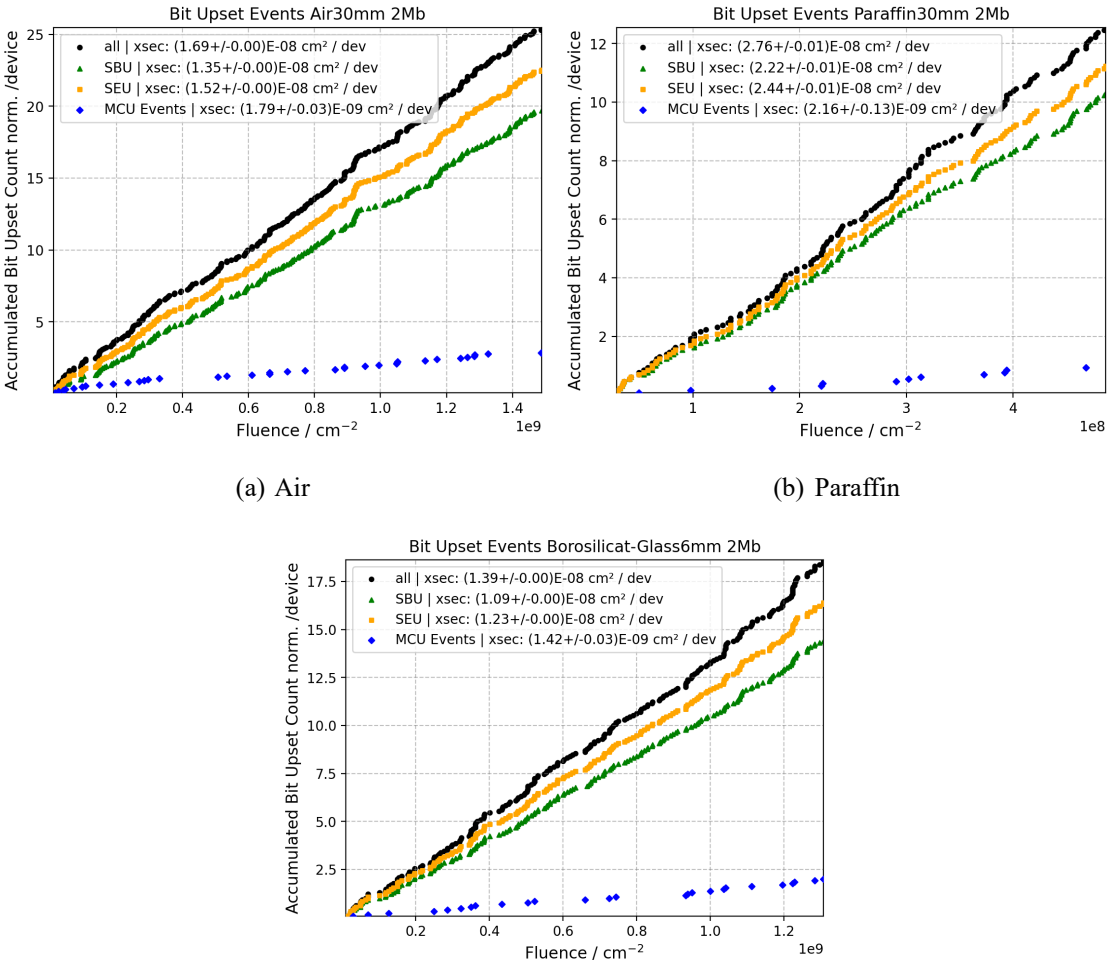

(a) Air

(b) Paraffin

(c) Borosilicat Glass

Figure A.1: Accumulated bit flips over fluence for two moderators and air condidition. The black line shows all bit flips, the orange line the SEU, the green line the SBU and the blue line the MCUs. The fitted cross section is shown in the legend.

A.2 T-Test Values

Table A.1: Values for the T-Test depending on the number of samples per group for 1σ confidence interval.

Number of Samples	T-Value
2	0.63
3	0.55
4	0.52
5	0.51
6	0.50
7	0.49
8	0.49
9	0.49
10	0.48
11	0.48
12	0.48
13	0.48
14	0.48
15	0.48

A.3 Detailed Results of CIEDs after Irradidation

Table A.2: Tested ICDs at 14.7 MeV neutrons and their response to irradiation.

Manufacturer	Fluence n/cm²	Type	Status
Biotronik	$8 \cdot 10^8$	ICD-Dual	Implant Error
		ICD-CRT	Implant Error
		ICD-CRT	Implant Error
		ICD-Single	Implant Error
	$4 \cdot 10^9$	ICD-CRT	Implant Error
		ICD-CRT	Implant Error
		ICD-Dual	Implant Error
		ICD-Single	Implant Error
	$2 \cdot 10^{10}$	ICD-CRT	Implant Error
		ICD-CRT	Implant Error
		ICD-Single	Implant Error
Medtronic	$8 \cdot 10^8$	ICD-Dual	
	$4 \cdot 10^9$	ICD-Dual	
	$2 \cdot 10^{10}$	ICD-Single	System Restart
St. Jude Medical	$8 \cdot 10^8$	ICD-Single	
		ICD-Dual	
	$4 \cdot 10^9$	ICD-Dual	Back Up VVI
		ICD-CRT	Back Up VVI
	$2 \cdot 10^{10}$	ICD-Single	Back Up VVI
		ICD-Single	Back Up VVI
		ICD-Single	Back Up VVI

Table A.3: Tested PMs at 14.7 MeV neutrons and their response to irradiation.

Manufacturer	Fluence n/cm²	Type	Status
Biotronik	$8 \cdot 10^8$	PM-Dual	Data Error
	$4 \cdot 10^9$	PM-Dual	Data Error
	$2 \cdot 10^{10}$	PM-Dual	Implant Error
Medtronic	$4 \cdot 10^9$	PM-Dual	
Boston Scientific	$8 \cdot 10^8$	PM-CRT	
St. Jude Medical	$8 \cdot 10^8$	PM-Dual	Back Up VVI
		PM-Dual	Back Up VVI
	$4 \cdot 10^9$	PM-CRT	Back Up VVI
		PM-Dual	Back Up VVI
		PM-Dual	Back Up VVI
	$2 \cdot 10^{10}$	PM-Dual	Back Up VVI
		PM-Single	Back Up VVI
		PM-Dual	Back Up VVI

Table A.4: Tested ICDs and their response to thermal neutrons, all devices with an * were irradiated before with 14 MeV neutrons.

Manufacturer	Fluence n/cm²	Type	Status
Biotronik	$2.3 \cdot 10^8$	ICD-Dual	*
		ICD-Dual	* Implant Error
		ICD-Dual	
		ICD-CRT	*
	$1.2 \cdot 10^9$	ICD-Single	* Implant Error
		ICD-CRT	Implant Error
		ICD-CRT	*
		ICD-CRT	* Implant Error
	$5.7 \cdot 10^9$	ICD-Single	* Implant Error
		ICD-CRT	
		ICD-CRT	*
		ICD-CRT	* Implant Error
Medtronic	$2.3 \cdot 10^8$	ICD-Dual	*
	$1.2 \cdot 10^9$	ICD-Dual	*
	$5.7 \cdot 10^9$	ICD-Single	* System Restart
Boston Scientific	$2.3 \cdot 10^8$	ICD-Single	
St. Jude Medical	$1.2 \cdot 10^9$	ICD-Dual	

Table A.5: Tested PMs and their response to thermal neutrons, all devices with a * were irradiated before with 14 MeV neutrons.

Manufacturer	Fluence n/cm²	Type	Status
Biotronik	$2.3 \cdot 10^8$	PM-Dual	Battery error
	$1.2 \cdot 10^9$	PM-Dual	*
		PM-Dual	
	$5.7 \cdot 10^9$	PM-CRT	
		PM-CRT	
Medtronic	$2.3 \cdot 10^8$	PM-Dual	*
	$5.7 \cdot 10^9$	PM-Dual	
Boston Scientific	$1.2 \cdot 10^9$	PM-CRT	
St. Jude Medical	$2.3 \cdot 10^8$	PM-Dual	
	$1.2 \cdot 10^9$	PM-Dual	Back Up VVI
		PM-Dual	
	$5.7 \cdot 10^9$	PM-Dual	
		PM-Dual	Back Up VVI

A.4 Failure Rates for GLEs

Table A.6: GLE Back up rates per event for ICDs.

	GLE5		GLE10		GLE69	
altitude / ft	0 GV	1.98 GV	0 GV	1.98 GV	0 GV	1.98 GV
0	9.9E-07	5.5E-07	1.1E-07	2.2E-08	5.3E-08	1.6E-08
10000	1.9E-05	8.1E-06	2.5E-06	3.7E-07	1.1E-06	2.5E-07
20000	1.7E-04	5.2E-05	3.1E-05	2.5E-06	1.3E-05	1.6E-06
30000	1.2E-03	2.3E-04	3.0E-04	1.2E-05	1.2E-04	7.6E-06
40000	3.5E-03	4.3E-04	1.1E-03	2.3E-05	3.9E-04	1.4E-05
43000	4.6E-03	4.7E-04	1.5E-03	2.5E-05	5.4E-04	1.6E-05

Table A.7: GLE Back up rates per event for PMs.

	GLE5		GLE10		GLE69	
altitude / ft	0 GV	1.98 GV	0 GV	1.98 GV	0 GV	1.98 GV
0	5.7E-07	3.2E-07	6.4E-08	1.3E-08	3.1E-08	9.1E-09
10000	1.1E-05	4.7E-06	1.5E-06	2.1E-07	6.6E-07	1.4E-07
20000	9.6E-05	3.0E-05	1.8E-05	1.5E-06	7.4E-06	9.5E-07
30000	7.1E-04	1.3E-04	1.7E-04	7.0E-06	6.7E-05	4.4E-06
40000	2.0E-03	2.5E-04	6.2E-04	1.3E-05	2.3E-04	8.2E-06
43000	2.6E-03	2.7E-04	8.7E-04	1.4E-05	3.1E-04	9.0E-06

A.5 Secondary Neutron Spectra Proton Therapy

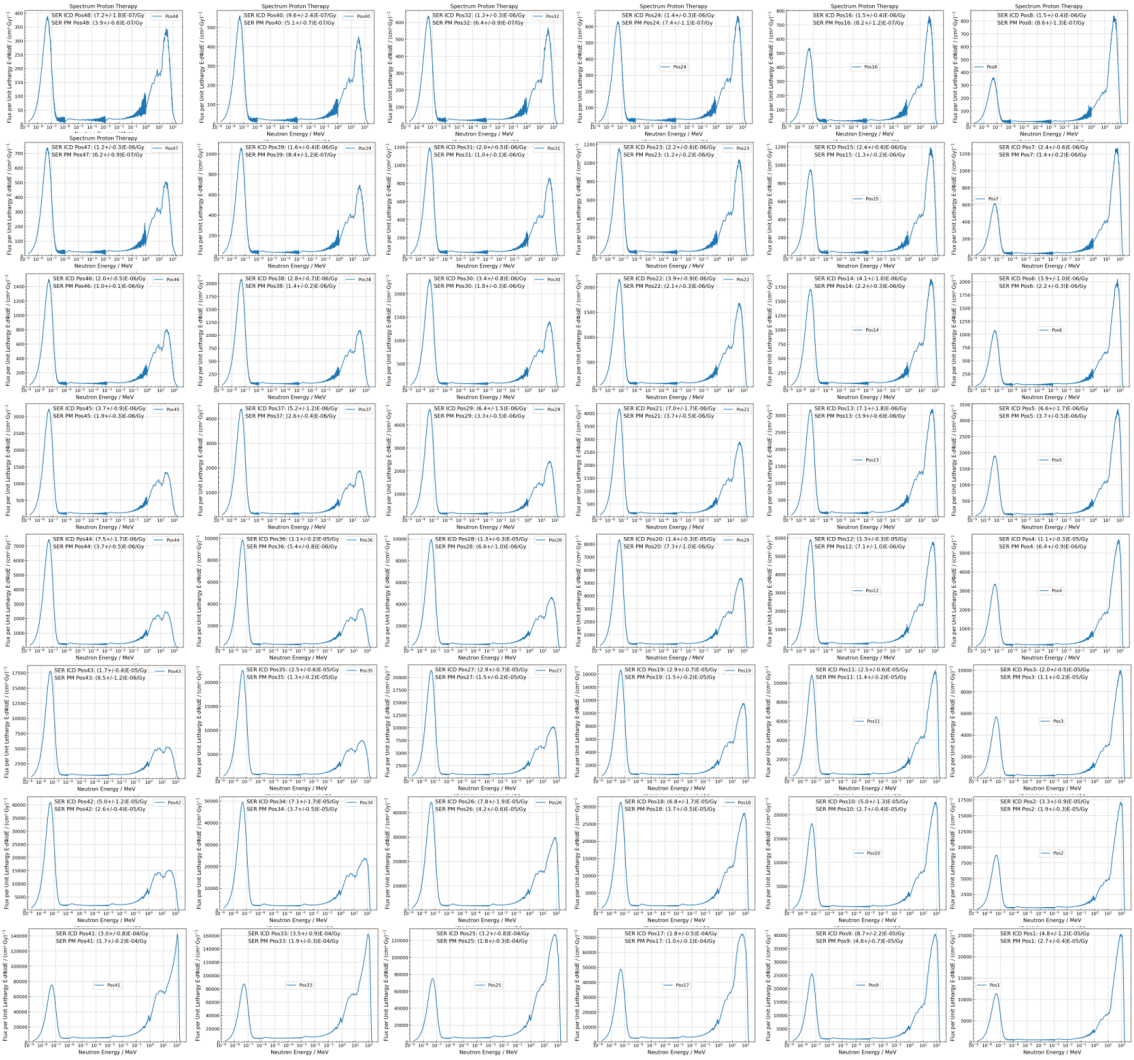

Figure A.2: 48 simulated spectra for the different positions towards the treatment volume. (Personal Communication Derksen, 2024)

Bibliography

Adamec, R., J.-M. Haefliger, J. P. Killisch, John P. M. Niederer, and P. Jaquet (1982). "Damaging Effect of Therapeutic Radiation on Programmable Pacemakers". In: *Pacing and Clinical Electrophysiology* 5.

Agostinelli, S. et al. (2003). "Geant4—a simulation toolkit". In: *Nuclear Instruments and Methods in Physics Research Section A: Accelerators, Spectrometers, Detectors and Associated Equipment* 506.3, pp. 250–303. ISSN: 0168-9002. DOI: https://doi.org/10.1016/S0168-9002(03)01368-8.

Ajiro, Y., F. Mori, and K. Iwade (2017). "Abrupt disruption of remote monitoring transmission as an indicator of safe backup mode". In: *Europace* 19.4, p. 595.

Allison, J. et al. (2006). "Geant4 developments and applications". In: *IEEE Transactions on Nuclear Science* 53.1, pp. 270–278. ISSN: 1558-1578. DOI: 10.1109/TNS.2006.869826.

Allison, J. et al. (2016). "Recent developments in Geant4". In: *Nuclear Instruments and Methods in Physics Research Section A: Accelerators, Spectrometers, Detectors and Associated Equipment* 835, pp. 186–225. ISSN: 0168-9002. DOI: https://doi.org/10.1016/j.nima.2016.06.125.

Alía, R. G. et al. (2017). "Simplified SEE Sensitivity Screening for COTS Components in Space". In: *IEEE Transactions on Nuclear Science* 64.2, pp. 882–890. ISSN: 1558-1578. DOI: 10.1109/TNS.2017.2653863.

Alía, R. G. et al. (2018). "Single Event Effect cross section calibration and application to quasi-monoenergetic and spallation facilities". In: *EPJ Nuclear Sci. Technol.* 4, p. 1. DOI: https://doi.org/10.1051/epjn/2017031.

Alía, R. G. et al. (2019). "Ultraenergetic Heavy-Ion Beams in the CERN Accelerator Complex for Radiation Effects Testing". In: *IEEE Transactions on Nuclear Science* 66.1, pp. 458–465. ISSN: 1558-1578. DOI: 10.1109/TNS.2018.2883501.

Alía, R. G. et al. (2023). "Heavy Ion Energy Deposition and SEE Intercomparison Within the RADNEXT Irradiation Facility Network". In: *IEEE Transactions on Nuclear Science* 70.8, pp. 1596–1605. ISSN: 1558-1578. DOI: 10.1109/TNS.2023.3260309.

Auden, E. C. et al. (2020). "Thermal Neutron-Induced Single-Event Upsets in Microcontrollers Containing Boron-10". In: *IEEE Transactions on Nuclear Science* 67.1, pp. 29–37. ISSN: 1558-1578. DOI: 10.1109/TNS.2019.2951996.

Australian Transport Safety Bureau (2008). "In-flight upset-Airbus A330-303, VH-QPA, 154 km west of Learmonth, WA, 7 October 2008". In: *Australian Transport Safety Bureau (ATSB), Canberra (Australia). Aviation Occurrence Investigation AO-2008-070*.

Baggio, J., D. Lambert, V. Ferlet-Cavrois, P. Paillet, C. Marcandella, and O. Duhamel (2007). “Single Event Upsets Induced by 1–10 MeV Neutrons in Static-RAMs Using Mono-Energetic Neutron Sources”. In: *IEEE Transactions on Nuclear Science* 54.6, pp. 2149–2155. ISSN: 1558-1578. DOI: 10.1109/TNS.2007.910039.

Bagur, R. et al. (2017). “Radiotherapy-Induced Cardiac Implantable Electronic Device Dysfunction in Patients With Cancer”. In: *The American Journal of Cardiology* 119.2, pp. 284–289. ISSN: 0002-9149. DOI: https://doi.org/10.1016/j.amjcard.2016.09.036.

Baraniuk, C. (2022). *The computer errors from outer space*. Newspaper Article. URL: https://www.bbc.com/future/article/20221011-how-space-weather-causes-computer-errors.

Barth, J. L., C.S. Dyer, and E.G. Stassinopoulos (2003). “Space, atmospheric, and terrestrial radiation environments”. In: *IEEE Transactions on nuclear science* 50.3, pp. 466–482. ISSN: 0018-9499. DOI: 10.1109/TNS.2003.813131.

Bartlett, D. T., J. L. Chartier, M. Matzke, A. Rimpler, and D. J. Thomas (2003). “Concepts and quantities in spectrometry and radiation protection”. In: *Radiat Prot Dosimetry* 107.1-3, pp. 23–35. ISSN: 0144-8420 (Print) 0144-8420. DOI: 10.1093/oxfordjournals.rpd.a006387.

Baumann, R. and K. Kruckmeyer (2019). *Radiation Handbook for Electronics*. Texas Instruments.

Baumann, R. C. (2005). “Radiation-induced soft errors in advanced semiconductor technologies”. In: *IEEE Transactions on Device and Materials Reliability* 5.3, pp. 305–316. ISSN: 1530-4388. DOI: 10.1109/tdmr.2005.853449.

Belverud, S., A. Mogilner, and M.l Schulder (2008). “Intrathecal pumps”. In: *Neurotherapeutics* 5.1, pp. 114–122. ISSN: 1933-7213.

Berger, Martin J, JS Coursey, MA Zucker, and J Chang (1998). *Stopping-power and range tables for electrons, protons, and helium ions*. NIST Physics Laboratory Gaithersburg, MD.

BFArM, Bundesinstitut für Arzneimittel und Medizinprodukte (2005). *Rückruf von St. Jude Medical -ICD Photon, Photon Micro und Atlas*. Press Release. URL: https://www.bfarm.de/SharedDocs/Kundeninfos/DE/01/2005/02528-05_kundeninfo_de.html.

BFArM, Bundesinstitut für Arzneimittel und Medizinprodukte (2017). *Dringende Sicherheitsinformation zu EMBLEM S-ICD von Boston Scientific CRM*. Press Release. URL: https://www.bfarm.de/SharedDocs/Kundeninfos/DE/01/2017/05887-17_kundeninfo_de.html.

Bhakta, D. and L. D. Foreman (2008). “Cosmic radiation: Not science fiction, but clinical reality”. In: *Heart Rhythm* 5.8, pp. 1204–1205. ISSN: 1547-5271.

Biotronik (2019). *BIOTRONIK Compendium*. Report. URL: https://biolink.biotronikusa.com/images/fca/pdf/BTN0655.pdf.

Bjerre, H. L. et al. (2021). "Risk of Cardiac Implantable Electronic Device Malfunctioning During Pencil Beam Proton Scanning in an In Vitro Setting". In: *International Journal of Radiation Oncology*Biology*Physics* 111.1, pp. 186–195. ISSN: 0360-3016. DOI: https://doi.org/10.1016/j.ijrobp.2021.03.053.

Boissonnat, G. et al. (2017). "Characterization and performances of DOSION, a dosimetry equipment dedicated to radiobiology experiments taking place at GANIL". In: *Nuclear Instruments and Methods in Physics Research Section A: Accelerators, Spectrometers, Detectors and Associated Equipment* 856, pp. 1–6. ISSN: 0168-9002. DOI: https://doi.org/10.1016/j.nima.2016.12.040.

Boston Scientific (2012). *Therapeutic radiation and implantable pacemakers and defibrillators*. Report. URL: https://www.bostonscientific.com/content/dam/bostonscientific/quality/education-resources/english/ACL_Therapeutic_Radiation_20120925.pdf.

Boston Scientific (2023). *Urgent Medical Device Information*. Report. URL: https://www.bostonscientific.com/content/dam/bostonscientific/quality/documents/Recent\%20Product\%20Advisories/2023_Nov_BSC_INGENIO-EL_HighImpedance_PhysLtr_FINAL07-US.pdf.

Bradley, P. D. and E. Normand (1998). "Single event upsets in implantable cardioverter defibrillators". In: *IEEE Transactions on Nuclear Science* 45.6, pp. 2929–2940. ISSN: 1558-1578. DOI: 10.1109/23.736549.

Brown, D.A. et al. (2018). "ENDF/B-VIII.0: The 8^{th} Major Release of the Nuclear Reaction Data Library with CIELO-project Cross Sections, New Standards and Thermal Scattering Data". In: *Nuclear Data Sheets* 148. Special Issue on Nuclear Reaction Data, pp. 1 –142. ISSN: 0090-3752. DOI: https://doi.org/10.1016/j.nds.2018.02.001.

Burgemeestre, G. M. and S. A. J. Timmer (2022). "Syncope due to pacemaker failure to capture after device transition into Safety Mode". In: *HeartRhythm Case Rep* 8.7, pp. 482–484. ISSN: 2214-0271 (Print) 2214-0271. DOI: 10.1016/j.hrcr.2022.04.008.

Burger, H. et al. (2024a). "Jahresbericht 2021 des Deutschen Herzschrittmacher- und Defibrillator-Registers – Teil 1: Herzschrittmacher". In: *Herzschrittmachertherapie + Elektrophysiologie* 35.1, pp. 46–60. ISSN: 1435-1544. DOI: 10.1007/s00399-023-00985-w.

Burger, H. et al. (2024b). "Jahresbericht 2021 des Deutschen Herzschrittmacher- und Defibrillator-Registers – Teil 2: Implantierbare Kardioverter-Defibrillatoren (ICD)". In: *Herzschrittmachertherapie + Elektrophysiologie* 35.1, pp. 61–79. ISSN: 1435-1544. DOI: 10.1007/s00399-023-00987-8.

Cazzaniga, C., D. Raspino, G. J. Sykora, and C. D. Frost (2021). “Dosimetry of Thermal Neutron Beamlines at a Pulsed Spallation Source for Application to the Irradiation of Microelectronics”. In: *IEEE Transactions on Nuclear Science* 68.5, pp. 921–927. ISSN: 1558-1578. DOI: 10.1109/TNS.2021.3064681.

Cecchetto, M. (2021). “Experimental and Simulation Study of Neutron-Induced Single Event Effects in Accelerator Environment and Implications on Qualification Approach”. Presented 13 Apr 2021. Montpellier University. URL: https://cds.cern.ch/record/2809556.

Cecchetto, M., R. García Alía, and F. Wrobel (2019). “Impact of Energy Dependence on Ground Level and Avionic SEE Rate Prediction When Applying Standard Test Procedures”. In: *Aerospace* 6.11, p. 119. ISSN: 2226-4310.

Cecchetto, M. et al. (2021). “0.1–10 MeV Neutron Soft Error Rate in Accelerator and Atmospheric Environments”. In: *IEEE Transactions on Nuclear Science* 68.5, pp. 873–883. ISSN: 0018-9499 1558-1578. DOI: 10.1109/tns.2021.3064666.

Clair, W.K., H. Williams, J. Hygaard, and P.J. Saavedra (2013). “A travel alert”. In: *J Innovation in CRM* 4, pp. 1457–1460.

Clemens, M. A. et al. (2011). “The Effects of Neutron Energy and High-Z Materials on Single Event Upsets and Multiple Cell Upsets”. In: *IEEE Transactions on Nuclear Science* 58.6, pp. 2591–2598. ISSN: 0018-9499. DOI: 10.1109/tns.2011.2171716.

Clement, N. L. and R. C. Lasky (2020). “Weibull Distribution and Analysis: 2019”. In: *2020 Pan Pacific Microelectronics Symposium (Pan Pacific)*, pp. 1–5. DOI: 10.23919/PanPacific48324.2020.9059313.

Clemente, J. A. et al. (2018). “SEU Characterization of Three Successive Generations of COTS SRAMs at Ultralow Bias Voltage to 14.2-MeV Neutrons”. In: *IEEE Transactions on Nuclear Science* 65.8, pp. 1858–1865. ISSN: 1558-1578. DOI: 10.1109/TNS.2018.2800905.

Coronetti, A. et al. (2020). “SEU characterization of commercial and custom-designed SRAMs based on 90 nm technology and below”. In: *2020 IEEE Radiation Effects Data Workshop (in conjunction with 2020 NSREC)*, pp. 1–8. DOI: 10.1109/REDW51883.2020.9325822.

Coronetti, A. et al. (2021). “Assessment of Proton Direct Ionization for the Radiation Hardness Assurance of Deep Submicron SRAMs Used in Space Applications”. In: *IEEE Transactions on Nuclear Science* 68, pp. 937–948.

Correas, V. et al. (2009). “Prediction of Multiple Cell Upset Induced by Heavy Ions in a 90 nm Bulk SRAM”. In: *IEEE Transactions on Nuclear Science* 56.4, pp. 2050–2055. ISSN: 1558-1578. DOI: 10.1109/TNS.2009.2013622.

De Saint-Hubert, M. et al. (2022). “The influence of nuclear models and Monte Carlo radiation transport codes on stray neutron dose estimations in proton therapy”. In:

Radiation Measurements 150, p. 106693. ISSN: 1350-4487. DOI: https://doi.org/10.1016/j.radmeas.2021.106693.

Derksen, L. (2024). Personal Communication.

Didi, A., A. Dadouch, O. Jaï, J. Tajmouati, and H. El Bekkouri (2017). "Neutron activation analysis: Modelling studies to improve the neutron flux of Americium–Beryllium source". In: *Nuclear Engineering and Technology* 49.4, pp. 787–791. ISSN: 1738-5733. DOI: https://doi.org/10.1016/j.net.2017.02.002.

Dirk, J. D., M. E. Nelson, J. F. Ziegler, A. Thompson, and T. H. Zabel (2003). "Terrestrial thermal neutrons". In: *IEEE Transactions on Nuclear Science* 50.6, pp. 2060–2064. ISSN: 1558-1578. DOI: 10.1109/TNS.2003.821587.

Dodd, P. E. and L. W. Massengill (2003). "Basic mechanisms and modeling of single-event upset in digital microelectronics". In: *IEEE Transactions on Nuclear Science* 50.3, pp. 583–602. ISSN: 1558-1578. DOI: 10.1109/TNS.2003.813129.

Dodd, P. E. and F. W. Sexton (1995). "Critical charge concepts for CMOS SRAMs". In: *IEEE Transactions on Nuclear Science* 42.6, pp. 1764–1771. ISSN: 1558-1578. DOI: 10.1109/23.488777.

Dong, A. X., R. P. Gwinn, N. M. Warner, L. M. Caylor, and M. J. Doherty (2016). "Mitigating bit flips or single event upsets in epilepsy neurostimulators". In: *Epilepsy Behav Case Rep* 5, pp. 72–4. ISSN: 2213-3232 (Print) 2213-3232 (Electronic) 2213-3232 (Linking). DOI: 10.1016/j.ebcr.2016.04.002.

Durantel, F. et al. (2016). "Dosimetry for radiobiology experiments at GANIL". In: *Nuclear Instruments and Methods in Physics Research Section A: Accelerators, Spectrometers, Detectors and Associated Equipment* 816, pp. 70–77. ISSN: 0168-9002. DOI: https://doi.org/10.1016/j.nima.2016.01.052.

Dyer, C. S., A. Hands, K. Ryden, and F. Lei (2017). "Extreme atmospheric radiation environments and single event effects". In: *IEEE Transactions on Nuclear Science* 65.1, pp. 432–438. ISSN: 0018-9499.

Dyer, C. S. and F. Lei (2001). "Monte Carlo calculations of the influence on aircraft radiation environments of structures and solar particle events". In: *IEEE Transactions on Nuclear Science* 48.6, pp. 1987–1995. ISSN: 1558-1578. DOI: 10.1109/23.983161.

Dyer, C. S., F. Lei, S. N. Clucas, D. F. Smart, and M. A. Shea (2003). "Solar particle enhancements of single-event effect rates at aircraft altitudes". In: *IEEE Transactions on Nuclear Science* 50.6, pp. 2038–2045. ISSN: 0018-9499 1558-1578. DOI: 10.1109/tns.2003.821375.

Eckert & Ziegler Nuclitec GmbH (2009). *Sealed Radiation Sources Product Information*. Dataset.

Elders, J., M. Kunze-Busch, R. Jan Smeenk, and J. LRM Smeets (2013). "High incidence of implantable cardioverter defibrillator malfunctions during radiation therapy: neu-

trons as a probable cause of soft errors". In: *Europace* 15.1, pp. 60–65. ISSN: 1532-2092.

ESA, European Space Agency (2014). *ESCC Basic Specification No. 25100, Single Event Effect Test Methods and Guidelines*. Standard.

EU (2017). "Regulation (EU) 2017/745 of the European Parliament and of the Council of 5 April 2017 on medical devices, amending Directive 2001/83/EC, Regulation (EC) No 178/2002 and Regulation (EC) No 1223/2009 and repealing Council Directives 90/385/EEC and 93/42/EEC". In: *Official Journal of the European Union* L.117, pp. 1–332.

Falco, M. D. et al. (2021). "A randomized in vitro evaluation of transient and permanent cardiac implantable electronic device malfunctions following direct exposure up to 10 Gy". In: *Strahlenther Onkol* 197.3, pp. 198–208. ISSN: 1439-099X (Electronic) 0179-7158 (Linking). DOI: 10.1007/s00066-020-01651-7.

FDA, U.S. Food & Drug Administration (2020). *MAUDE - Manufacturer and User Facility Device Experience*. Dataset. URL: https://www.accessdata.fda.gov/scripts/cdrh/cfdocs/cfmaude/search.cfm.

Ferrick, A. M., N. Bernstein, A. Aizer, and L. Chinitz (2008). "Cosmic radiation induced software electrical resets in ICDs during air travel". In: *Heart Rhythm* 5.8, pp. 1201–1203. ISSN: 1547-5271. DOI: https://doi.org/10.1016/j.hrthm.2008.04.018.

Francke, A. (2022). Personal Communication.

Gauter-Fleckenstein, B. et al. (2015). "DEGRO/DGK guideline for radiotherapy in patients with cardiac implantable electronic devices". In: *Strahlenther Onkol* 191.5, pp. 393–404. DOI: 10.1007/s00066-015-0817-3.

Gebhardt, R., M. Ludwig, S. Kirsner, K. Kisling, and A. K. Kosturakis (2013). "Implanted Intrathecal Drug Delivery Systems and Radiation Treatment". In: *Pain Medicine* 14.3, pp. 398–402. ISSN: 1526-2375. DOI: 10.1111/pme.12037.

Gelblum, D. Y. and H. Amols (2009). "Implanted cardiac defibrillator care in radiation oncology patient population". In: *Int J Radiat Oncol Biol Phys* 73.5, pp. 1525–31. ISSN: 1879-355X (Electronic) 0360-3016 (Linking). DOI: 10.1016/j.ijrobp.2008.06.1903.

Gibson, JAB (1986). "The relative tissue kerma sensitivity of thermoluminescent materials to neutrons". In: *Radiation protection dosimetry* 15.4, pp. 253–266. ISSN: 1742-3406.

Giot, D., P. Roche, G. Gasiot, J. L. Autran, and R. Harboe-Sorensen (2008). "Heavy Ion Testing and 3-D Simulations of Multiple Cell Upset in 65 nm Standard SRAMs". In: *IEEE Transactions on Nuclear Science* 55.4, pp. 2048–2054. ISSN: 1558-1578. DOI: 10.1109/TNS.2008.916063.

Glikson, M. and P. A. Friedman (2001). “The implantable cardioverter defibrillator”. In: *The Lancet* 357.9262, pp. 1107–1117. ISSN: 0140-6736. DOI: https://doi.org/10.1016/S0140-6736(00)04263-X.

Glikson, M. et al. (2021). “2021 ESC Guidelines on cardiac pacing and cardiac resynchronization therapy: Developed by the Task Force on cardiac pacing and cardiac resynchronization therapy of the European Society of Cardiology (ESC) With the special contribution of the European Heart Rhythm Association (EHRA)”. In: *European Heart Journal* 42.35, pp. 3427–3520. ISSN: 0195-668X. DOI: 10.1093/eurheartj/ehab364.

Goldhagen, P, JM Clem, and JW Wilson (2004). “The energy spectrum of cosmic-ray induced neutrons measured on an airplane over a wide range of altitude and latitude”. In: *Radiation protection dosimetry* 110.1-4, pp. 387–392. ISSN: 1742-3406.

Goldhagen, Paul (2003). “Cosmic-ray neutrons on the ground and in the atmosphere”. In: *MRS bulletin* 28.2, pp. 131–135. ISSN: 1938-1425.

Gomez, D. R. et al. (2013). “Malfunctions of implantable cardiac devices in patients receiving proton beam therapy: incidence and predictors”. In: *Int J Radiat Oncol Biol Phys* 87.3, pp. 570–5. ISSN: 1879-355X (Electronic) 0360-3016 (Print) 0360-3016 (Linking). DOI: 10.1016/j.ijrobp.2013.07.010.

Gorbunov, M. S. et al. (2014). “Design of 65 nm CMOS SRAM for Space Applications: A Comparative Study”. In: *IEEE Transactions on Nuclear Science* 61.4, pp. 1575–1582. ISSN: 1558-1578. DOI: 10.1109/TNS.2014.2319154.

Gordon, MS et al. (2004). “Measurement of the flux and energy spectrum of cosmic-ray induced neutrons on the ground”. In: *IEEE Transactions on Nuclear Science* 51.6, pp. 3427–3434. ISSN: 0018-9499.

Grant, J. D. et al. (2015). “Radiotherapy-Induced Malfunction in Contemporary Cardiovascular Implantable Electronic Devices: Clinical Incidence and Predictors”. In: *JAMA Oncology* 1.5, pp. 624–632. ISSN: 2374-2437. DOI: 10.1001/jamaoncol.2015.1787.

Harboe-Sorensen, R., F. X. Guerre, and A. Roseng (2005). “Design, Testing and Calibration of a ”Reference SEU Monitor” System”. In: *2005 8th European Conference on Radiation and Its Effects on Components and Systems*, B3–1–B3–7. ISBN: 0379-6566. DOI: 10.1109/RADECS.2005.4365561.

Hashii, H. et al. (2013). “Comparison of the effects of high-energy photon beam irradiation (10 and 18 MV) on 2 types of implantable cardioverter-defibrillators”. In: *Int J Radiat Oncol Biol Phys* 85.3, pp. 840–5. ISSN: 1879-355X (Electronic) 0360-3016 (Linking). DOI: 10.1016/j.ijrobp.2012.05.043.

Hashimoto, T. et al. (2012). “Influence of secondary neutrons induced by proton radiotherapy for cancer patients with implantable cardioverter defibrillators”. In: *Radiation Oncology* 7.10.

Hashimoto, T. et al. (2022). “Particle therapy using protons or carbon ions for cancer patients with cardiac implantable electronic devices (CIED): a retrospective multi-institutional study”. In: *Japanese Journal of Radiology* 40.5, pp. 525–533. ISSN: 1867-108X. DOI: 10.1007/s11604-021-01218-1.

Hayes, David (2024). *Managing Radiation Therapy in the CIED Patient*. Discussion Forum. URL: https://www.biotronik.com/sites/default/files/2024-05/1_%20Managing%20Radiation%20Therapy%20for%20CIED%20Patients.pdf.

Hess, V. (1912). “Über Beobachtungen der durchdringenden Strahlung bei sieben Freiballonfahrten”. In: *Z. Phys.* 13, p. 1084.

Hoecht, S., P Rosenthal, D. Sancar, S. Behrens, W. Hinkelbein, and U. Hoeller (2002). “Implantable cardiac defibrillators may be damaged by radiation therapy”. In: *Journal of clinical oncology : official journal of the American Society of Clinical Oncology* 20 8, pp. 2212–3.

Hurkmans, C. W., E. Scheepers, B. G. F. Springorum, and H. Uiterwaal (2005). “Influence of radiotherapy on the latest generation of pacemakers”. In: *Radiotherapy and Oncology* 76.1, pp. 93–98. ISSN: 0167-8140. DOI: https://doi.org/10.1016/j.radonc.2005.06.011.

ICRP (2007). “ICRP publication 103”. In: *Ann ICRP* 37.2.4, p. 2.

IEC, International Electrotechnical Comission (2016). *IEC62396-1:2016: Process management for avionics - Atmospheric radiation effects - Part 1: Accommodation of atmospheric radiation effects via single event effects within avionics electronic equipment*. Standard.

IEC, International Electrotechnical Comission (2017). *IEC62396-2:2017: Process management for avionics—Atmospheric radiation effects. Accommodation of atmospheric radiation effects via single event effects within avionics electronic equipment*. Standard.

Indik, J. H. et al. (2017). “2017 HRS expert consensus statement on magnetic resonance imaging and radiation exposure in patients with cardiovascular implantable electronic devices”. In: *Heart Rhythm* 14.7, e97–e153. ISSN: 1556-3871 (Electronic) 1547-5271 (Linking). DOI: 10.1016/j.hrthm.2017.04.025.

Ing, H., R. A. Noulty, and T. D. McLean (1997). “Bubble detectors—A maturing technology”. In: *Radiation Measurements* 27.1, pp. 1–11. ISSN: 1350-4487. DOI: https://doi.org/10.1016/S1350-4487(96)00156-4.

ISO, International Organization for Standardization (2014). *ISO14708:2014: Implants for surgery — Active implantable medical devices — Part 1: General requirements for safety, marking and for information to be provided by the manufacturer*. Standard.

ISO, International Organization for Standardization (2019a). *Implants for surgery — Active implantable medical devices — Part 7: Particular requirements for cochlear and auditory brainstem implant systems*. Standard.

ISO, International Organization for Standardization (2019b). *ISO 14971:2019: Medical devices — Application of risk management to medical devices*. Standard.

ISSI, Integrated Silicon Solution Inc. (2021a). *IS62/65WVS2568GALL, IS62/65WVS2568GBLL - 256Kx8 low voltage, fast serial SRAM with SPI, SDI and SQI interface*. Dataset.

ISSI, Integrated Silicon Solution Inc. (2021b). *IS62/65WVS5128GALL, IS62/65WVS5128GBLL - 256Kx8 low voltage, fast serial SRAM with SPI, SDI and SQI interface*. Dataset.

JEDEC (2017). *JESD57A: Test Procedures for the Measurement of Single-Event Effects in Semiconductor Devices from Heavy Ion Irradiation*. Standard.

JEDEC (2021). *JESD89B: Measurement and Reporting of Alpha Particle and Terrestrial Cosmic Ray-Induced Soft Errors in Semiconductor Devices*. Standard.

Kapa, S., L. Fong, C. R. Blackwell, M. G. Herman, P. J. Schomberg, and D. L. Hayes (2008). "Effects of Scatter Radiation on ICD and CRT Function". In: *Pacing and Clinical Electrophysiology* 31.6, pp. 727–732. ISSN: 0147-8389. DOI: https://doi.org/10.1111/j.1540-8159.2008.01077.x.

Katzenberg, C. A., F. Marcus, R. S. Heusinkveld, and R. B. Mammana (1982). "Pacemaker Failure Due to Radiation Therapy". In: *Pacing and Clinical Electrophysiology* 5.

Klüter, Sebastian et al. (2021). "A practical implementation of risk management for the clinical introduction of online adaptive Magnetic Resonance-guided radiotherapy". In: *Physics and Imaging in Radiation Oncology* 17, pp. 53–57. ISSN: 2405-6316. DOI: https://doi.org/10.1016/j.phro.2020.12.005.

Kobayashi, D. (2021). "Scaling Trends of Digital Single-Event Effects: A Survey of SEU and SET Parameters and Comparison With Transistor Performance". In: *IEEE Transactions on Nuclear Science* 68.2, pp. 124–148. ISSN: 1558-1578. DOI: 10.1109/TNS.2020.3044659.

Koivunoro, H. et al. (2011). "Epithermal neutron beam interference with cardiac pacemakers". In: *Applied Radiation and Isotopes* 69.12, pp. 1904–1906. ISSN: 0969-8043. DOI: https://doi.org/10.1016/j.apradiso.2011.03.028.

Kramer, D. et al. (2011). "LHC RadMon SRAM Detectors Used at Different Voltages to Determine the Thermal Neutron to High Energy Hadron Fluence Ratio". In: *IEEE Transactions on Nuclear Science* 58, pp. 1117–1122.

Kry, Stephen F. et al. (2017). "AAPM TG 158: Measurement and calculation of doses outside the treated volume from external-beam radiation therapy". In: *Medical Physics* 44.10, e391–e429. ISSN: 0094-2405. DOI: https://doi.org/10.1002/mp.12462.

Köhli, Markus, Jannis Weimar, Martin Schrön, Roland Baatz, and Ulrich Schmidt (2021). "Soil Moisture and Air Humidity Dependence of the Above-Ground Cosmic-Ray Neu-

tron Intensity". In: *Frontiers in Water* 2. ISSN: 2624-9375. DOI: 10.3389/frwa.2020.544847.

Lau, D. H. et al. (2008). "Defibrillator reset by radiotherapy". In: *International Journal of Cardiology* 130.1, e37–e38. ISSN: 0167-5273. DOI: https://doi.org/10.1016/j.ijcard.2007.06.145.

Lawrence, R. K. and A. T. Kelly (2008). "Single Event Effect Induced Multiple-Cell Upsets in a Commercial 90 nm CMOS Digital Technology". In: *IEEE Transactions on Nuclear Science* 55.6, pp. 3367–3374. ISSN: 1558-1578. DOI: 10.1109/TNS.2008.2005981.

Lee, R. W., S. K. Huang, E. Mechling, and I. Bazgan (1986). "Runaway atrioventricular sequential pacemaker after radiation therapy". In: *The American Journal of Medicine* 81.5, pp. 883–886. ISSN: 0002-9343. DOI: https://doi.org/10.1016/0002-9343(86)90361-X.

Lewin, A. A., C. F. Serago, J.G. Schwade, A. A. Abitbol, and S. C. Margolis (1984). "Radiation induced failures of complementary metal oxide semiconductor containing pacemakers: A potentially lethal complication". In: *International Journal of Radiation Oncology*Biology*Physics* 10.10, pp. 1967–1969. ISSN: 0360-3016. DOI: https://doi.org/10.1016/0360-3016(84)90279-7.

Lovell, J. L., M. L. Duldig, and J. E. Humble (1998). "An extended analysis of the September 1989 cosmic ray ground level enhancement". In: *Journal of Geophysical Research: Space Physics* 103.A10, pp. 23733–23742. ISSN: 0148-0227. DOI: https://doi.org/10.1029/98JA02100.

Lucsányi, D., R. G. Alía, K. Biłko, M. Cecchetto, S. Fiore, and E. Pirovano (2022). "G4SEE: A Geant4-Based Single Event Effect Simulation Toolkit and Its Validation Through Monoenergetic Neutron Measurements". In: *IEEE Transactions on Nuclear Science* 69.3, pp. 273–281. ISSN: 1558-1578. DOI: 10.1109/TNS.2022.3149989.

Makkar, A. et al. (2012). "Effect of radiation therapy on permanent pacemaker and implantable cardioverter-defibrillator function". In: *Heart rhythm* 9 12, pp. 1964–8.

Malavasi, V. L. et al. (2020). "Radiotherapy-induced malfunctions of cardiac implantable electronic devices in cancer patients". In: *Intern Emerg Med* 15.6, pp. 967–973. ISSN: 1970-9366 (Electronic) 1828-0447 (Linking). DOI: 10.1007/s11739-019-02240-y.

Malavasi, V. L. et al. (2023). "A systematic review and meta-analysis on oncological radiotherapy in patients with a cardiac implantable electronic device: Prevalence and predictors of device malfunction in 3121 patients". In: *European Journal of Clinical Investigation* 53.1, e13862. ISSN: 0014-2972.

Martone, M., M. Angelone, and M. Pillon (1994). "The 14 MeV Frascati neutron generator". In: *Journal of Nuclear Materials* 212-215, pp. 1661–1664. ISSN: 0022-3115. DOI: https://doi.org/10.1016/0022-3115(94)91109-6.

Matsubara, H., T. Ezura, Y. Hashimoto, K. Karasawa, T. Nishio, and M. Tsuneda (2020). "Prediction of radiation-induced malfunction for cardiac implantable electronic devices (CIEDs)". In: *Med Phys* 47.4, pp. 1489–1498. ISSN: 2473-4209 (Electronic) 0094-2405 (Linking). DOI: 10.1002/mp.14057.

Matthiä, D. (2024). Personal Communication.

Matthiä, D., M. M. Meier, and G. Reitz (2014). "Numerical calculation of the radiation exposure from galactic cosmic rays at aviation altitudes with the PANDOCA core model". In: *Space Weather* 12.3, pp. 161–171. ISSN: 15427390. DOI: 10.1002/2013sw001022.

Matthiä, Daniel, Martin Schaefer, and Matthias M. Meier (2015). "Economic impact and effectiveness of radiation protection measures in aviation during a ground level enhancement". In: *J. Space Weather Space Clim.* 5. URL: https://doi.org/10.1051/swsc/2015014.

McCracken, K.G., H. Moraal, and P.H. Stoker (2008). "Investigation of the multiple-component structure of the 20 January 2005 cosmic ray ground level enhancement". In: *Journal of Geophysical Research: Space Physics* 113.A12. ISSN: 0148-0227.

Medtronic CRM Technical Services (n.d.). *RADIATION Rev. C, p.1 of 2*. Report. Medtronic. URL: https://www.eviq.org.au/getmedia/3c5bc4fa-7b2d-419d-973b-b3546bdbc6fb/430-Mx-of-pacemakers-and-ICDs-in-patients-receiving-RT-Medtronic-Pace-ICD-letter.pdf.aspx.

Medtronic CRM Technical Services (2013). *Therapeutic Radiation*. Report. Medtronic, Inc. URL: https://www.internationaljournalofcardiology.com/cms/10.1016/j.ijcard.2017.12.061/attachment/77cadbe3-b1d3-42ad-bd4d-fa948710592d/mmc6.pdf.

Mekhaldi, F. et al. (2015). "Multiradionuclide evidence for the solar origin of the cosmic-ray events of AD 774/5 and 993/4". In: *Nature Communications* 6.1, p. 8611. ISSN: 2041-1723. DOI: 10.1038/ncomms9611.

Microchip Technology Inc. (2011). *23A1024/23LC1024 - 1Mbit SPI Serial SRAM with SDI and SQI Interface*. Dataset.

Miften, M. et al. (2019). "Management of Radiotherapy Patients with Implanted Cardiac Pacemakers and Defibrillators: A Report of the AAPM TG-203". In: *Medical physics*.

Miller, F., Cécile Weulersse, Thierry Carrière, Nicolas Guibbaud, Sébastien Morand, and R. Gaillard (2013). "Investigation of 14 MeV Neutron Capabilities for SEU Hardness Evaluation". In: *IEEE Transactions on Nuclear Science* 60, pp. 2789–2796.

Mond, H. G. and A. Proclemer (2011). "The 11th World Survey of Cardiac Pacing and Implantable Cardioverter-Defibrillators: Calendar Year 2009–A World Society of Arrhythmia's Project". In: *Pacing and Clinical Electrophysiology* 34.

Mouton, J., R. Haug, A. Bridier, B. Dodinot, and F. Eschwege (2002). “Influence of high-energy photon beam irradiation on pacemaker operation”. In: *Physics in Medicine & Biology* 47.16, p. 2879. ISSN: 0031-9155. DOI: 10.1088/0031-9155/47/16/304.

Naseri, A. and A. Mesbahi (2010). “A review on photoneutrons characteristics in radiation therapy with high-energy photon beams”. In: *Rep Pract Oncol Radiother* 15.5, pp. 138–44. DOI: 10.1016/j.rpor.2010.08.003.

Nemec, J. (2007). “Runaway Implantable Defibrillator—A Rare Complication of Radiation Therapy”. In: *Pacing and Clinical Electrophysiology* 30.5, pp. 716–718. ISSN: 0147-8389. DOI: https://doi.org/10.1111/j.1540-8159.2007.00735.x.

Normand, E., K. Vranish, A. Sheets, M. Stitt, and R. Kim (2006). “Quantifying the Double-Sided Neutron SEU Threat, From Low Energy (Thermal) and High Energy (>10 MeV) Neutrons”. In: *IEEE Transactions on Nuclear Science* 53.6, pp. 3587–3595. ISSN: 1558-1578. DOI: 10.1109/TNS.2006.886209.

Normand, Eugene and Laura Dominik (2010). “Cross comparison guide for results of neutron SEE testing of microelectronics applicable to avionics”. In: *2010 IEEE Radiation Effects Data Workshop*. IEEE, pp. 8–8. ISBN: 1424484049.

Obermueller, L., C. Cazzaniga, S. Kulmiya, and C. D. Frost (2018). *A Fast Neutron Monitor Based on Single Event Effects in SRAMs Using Commercial off-the-Shelf Components*. Conference Paper. DOI: 10.1109/radecs45761.2018.9328731.

Odell, D. W. et al. (2021). “The Effect of Measured Radiotherapy Dose on Intrathecal Drug Delivery System Function”. In: *Neuromodulation: Technology at the Neural Interface* 24.7, pp. 1204–1208. ISSN: 1094-7159. DOI: https://doi.org/10.1111/ner.13372.

Okano, N. et al. (2021). “Safety verification of carbon-ion radiotherapy for patients with cardiac implantable electronic devices (CIEDs)”. In: *Journal of Radiation Research* 63, pp. 122 –127.

Oshiro, Y. et al. (2008). “Proton beam therapy interference with implanted cardiac pacemakers”. In: *Int J Radiat Oncol Biol Phys* 72.3, pp. 723–7. ISSN: 1879-355X (Electronic) 0360-3016 (Linking). DOI: 10.1016/j.ijrobp.2008.01.062.

Paz, O., N. Teodorovich, Y. Kogan, and M. Swissa (2017). “Transatlantic flight: Not only jet lag”. In: *Heart Rhythm* 14(7), pp. 1556–3871. DOI: 10.1016/j.hrthm.2017.03.033.

Petersen, E. L., J. C. Pickel, E. C. Smith, P. J. Rudeck, and J. R. Letaw (1993). “Geometrical factors in SEE rate calculations”. In: *IEEE Transactions on Nuclear Science* 40.6, pp. 1888–1909. ISSN: 1558-1578. DOI: 10.1109/23.273465.

Philbert, B. T. et al. (2016). “Is modification of the VVI backup mode in implantable cardioverter-defibrillators from St Jude medical required due to increased risk of inappropriate shocks?” In: *EP Europace* 19.5, pp. 808–811. ISSN: 1099-5129. DOI: 10.1093/europace/euw083.

Pickel, J. C. (1982). “Effect of CMOS Miniaturization on Cosmic-Ray-Induced Error Rate”. In: *IEEE Transactions on Nuclear Science* 29.6, pp. 2049–2054. ISSN: 1558-1578. DOI: 10.1109/TNS.1982.4336494.

Poluianov, S. V., I. G. Usoskin, A. L. Mishev, M. A. Shea, and D. F. Smart (2017). “GLE and Sub-GLE Redefinition in the Light of High-Altitude Polar Neutron Monitors”. In: *Solar Physics* 292.11, p. 176. ISSN: 1573-093X. DOI: 10.1007/s11207-017-1202-4. URL: https://doi.org/10.1007/s11207-017-1202-4.

Pourhamidi, A. H. (1983). “Radiation Effect On Implanted Pacemakers”. In: *Chest* 84.4, pp. 499–500. ISSN: 0012-3692. DOI: https://doi.org/10.1378/chest.84.4.499.

Pradhan, A.S. (1981). “Thermoluminescence Dosimetry and its Applications”. In: *Radiation Protection Dosimetry* 1.3, pp. 153–167. ISSN: 0144-8420. DOI: 10.1093/oxfordjournals.rpd.a079971.

Quinn, H., A. Watkins, L. Dominik, and C. Slayman (2019). “The Effect of 1–10-MeV Neutrons on the JESD89 Test Standard”. In: *IEEE Transactions on Nuclear Science* 66.1, pp. 140–147. ISSN: 1558-1578. DOI: 10.1109/TNS.2018.2884908.

Raitt, M. H. et al. (1994). “Runaway pacemaker during high-energy neutron radiation therapy”. In: *Chest* 106.3, pp. 955–7. ISSN: 0012-3692 (Print) 0012-3692 (Linking). DOI: 10.1378/chest.106.3.955.

Raukunen, O. et al. (2018). “Two solar proton fluence models based on ground level enhancement observations”. In: *J. Space Weather Space Clim.* 8, A04.

Reed, R. A. et al. (2007). “Impact of Ion Energy and Species on Single Event Effects Analysis”. In: *IEEE Transactions on Nuclear Science* 54.6, pp. 2312–2321. ISSN: 0018-9499. DOI: 10.1109/tns.2007.909901.

Reed, R. A. et al. (2013). “Anthology of the Development of Radiation Transport Tools as Applied to Single Event Effects”. In: *IEEE Transactions on Nuclear Science* 60.3, pp. 1876–1911. ISSN: 1558-1578. DOI: 10.1109/TNS.2013.2262101.

Reyes, D. P., Steven S. McClure, Jeffery C. Chancellor, Rebecca S. Blue, Tarah L. Castleberry, and James M. Vanderploeg (2014). “Implanted medical devices in the radiation environment of commercial spaceflight”. In: *Aviation, space, and environmental medicine* 85 11, pp. 1106–13.

Rieppo, R. (1984). “The thermalization of 241Am/Be-neutrons in paraffin. The absolute intensities of 241Am/Be-neutrons as a function of neutron energy”. In: *The International Journal of Applied Radiation and Isotopes* 35.1, pp. 41–43. ISSN: 0020-708X. DOI: https://doi.org/10.1016/0020-708X(84)90129-7.

Riva, G. et al. (2018). “Radiotherapy in patients with cardiac implantable electronic devices: clinical and dosimetric aspects”. In: *Medical Oncology* 35.5, p. 73. ISSN: 1559-131X. DOI: 10.1007/s12032-018-1126-3.

Röhn-Klinikum AG (2024). *Technische Details*. Web Page. URL: https://www.mit-marburg.de/fuer-forscher/technische-details.html.

Røed, K. et al. (2011). "Method for measuring mixed field radiation levels relevant for SEEs at the LHC". In: *2011 12th European Conference on Radiation and Its Effects on Components and Systems*, pp. 516–523. ISBN: 0379-6566. DOI: 10.1109/RADECS.2011.6131358.

Sato, T. (2015). "Analytical Model for Estimating Terrestrial Cosmic Ray Fluxes Nearly Anytime and Anywhere in the World: Extension of PARMA/EXPACS". In: *PLOS ONE* 10.12, e0144679. DOI: 10.1371/journal.pone.0144679.

Seidensaal, K. et al. (2019). "Active-Scanned Protons and Carbon Ions in Cancer Treatment of Patients With Cardiac Implantable Electronic Devices: Experience of a Single Institution". In: *Frontiers in Oncology* 9.

Serre, S. et al. (2012). "Geant4 analysis of n-Si nuclear reactions from different sources of neutrons and its implication on soft-error rate". In: *IEEE Transactions on Nuclear Science* 59.4, pp. 714–722. ISSN: 0018-9499.

Sharifzadehgan, A. et al. (2020). "Radiotherapy in Patients With a Cardiac Implantable Electronic Device". In: *The American Journal of Cardiology* 128, pp. 196–201. ISSN: 0002-9149. DOI: https://doi.org/10.1016/j.amjcard.2020.04.045.

Shrestha, S., W. D. Newhauser, W.P. Donahue, and A. Perez-Andujar (2022). "Stray neutron radiation exposures from proton therapy: physics-based analytical models of neutron spectral fluence, kerma and absorbed dose". In: *Physics in Medicine & Biology* 67.12, p. 125019. ISSN: 0031-9155.

Sierawski, B. D. et al. (2009). "Impact of Low-Energy Proton Induced Upsets on Test Methods and Rate Predictions". In: *IEEE Transactions on Nuclear Science* 56.6, pp. 3085–3092. ISSN: 1558-1578. DOI: 10.1109/TNS.2009.2032545.

Sierawski, B. D. et al. (2010). "Contribution of low-energy (10 MeV) neutrons to upset rate in a 65 nm SRAM". In: *2010 IEEE International Reliability Physics Symposium*, pp. 395–399. ISBN: 1938-1891. DOI: 10.1109/IRPS.2010.5488796.

Sierawski, B. D. et al. (2011). "Effects of scaling on muon-induced soft errors". In: *2011 International Reliability Physics Symposium*, pp. 3C.3.1–3C.3.6. ISBN: 1938-1891. DOI: 10.1109/IRPS.2011.5784484.

Singh, A. K., D. Siingh, and R. P. Singh (2010). "Space Weather: Physics, Effects and Predictability". In: *Surveys in Geophysics* 31.6, pp. 581–638. ISSN: 1573-0956. DOI: 10.1007/s10712-010-9103-1.

Smart, D. F. and M. A. Shea (2005). "A review of geomagnetic cutoff rigidities for earth-orbiting spacecraft". In: *Advances in Space Research* 36.10, pp. 2012–2020. ISSN: 0273-1177. DOI: https://doi.org/10.1016/j.asr.2004.09.015.

Smart, D.F. and M.A. Shea (1985). "Galactic cosmic radiation and solar energetic particles". In: *Handbook of geophysics and the space environment*, pp. 6–1.

Soejima, T. et al. (2011). “Radiation therapy in patients with implanted cardiac pacemakers and implantable cardioverter defibrillators: a prospective survey in Japan”. In: *Journal of radiation research* 52 4, pp. 516–21.

Souliman, S.K. and J. Christie (1994). “Pacemaker Failure Induced by Radiotherapy”. In: *Pacing and Clinical Electrophysiology* 17.3, pp. 270–273. ISSN: 0147-8389. DOI: https://doi.org/10.1111/j.1540-8159.1994.tb01387.x.

Spiezia, G. et al. (2011). “The LHC radiation monitoring system—RadMon”. In: *Proc. Sci* 143, pp. 1–12.

St. Jude Medical Technical Services (2016). *Effects of Therapeutic Radiation on St. Jude Medical Implantable Cardiac Rhythm Devices*. Report. URL: https://www.internationaljournalofcardiology.com/cms/10.1016/j.ijcard.2017.12.061/attachment/f84737ce-9228-4b4a-9789-263b360e8719/mmc7.pdf.

Stolarczyk, L. et al. (2018). “Dose distribution of secondary radiation in a water phantom for a proton pencil beam—EURADOS WG9 intercomparison exercise”. In: *Physics in Medicine & Biology* 63.8, p. 085017. ISSN: 0031-9155. DOI: 10.1088/1361-6560/aab469.

Thomas, D., R. Becker, H. A. Katus, W. Schoels, and C. A. Karle (2004). “Radiation therapy-induced electrical reset of an implantable cardioverter defibrillator device located outside the irradiation field”. In: *Journal of Electrocardiology* 37.1, pp. 73–74. ISSN: 0022-0736. DOI: https://doi.org/10.1016/j.jelectrocard.2003.10.005.

Trigano, A., G. Hubert, J. Marfaing, and K. Castellani (2012). “Experimental study of neutron-induced soft errors in modern cardiac pacemakers”. In: *J Interv Card Electrophysiol* 33.1, pp. 19–25. ISSN: 1572-8595 (Electronic) 1383-875X (Linking). DOI: 10.1007/s10840-011-9609-6.

Ueyama, T. et al. (2016). “Pacemaker malfunction associated with proton beam therapy: a report of two cases and review of literature-does field-to-generator distance matter?” In: *Oxf Med Case Reports* 2016.8, omw049. ISSN: 2053-8855 (Print) 2053-8855 (Electronic) 2053-8855 (Linking). DOI: 10.1093/omcr/omw049.

Usoskin, I. (2024). *Cosmic Ray Station of the University of Oulu / Sodankyla Geophysical Observatory*. Web Page. URL: https://cosmicrays.oulu.fi/.

Vedelago, J., F. A. Geser, I. D. Munoz, A. Stabilini, E. G. Yukihara, and O. Jäkel (2022). “Assessment of secondary neutrons in particle therapy by Monte Carlo simulations”. In: *Physics in Medicine & Biology* 67.1, p. 015008. ISSN: 0031-9155.

Vedelago, J., S. Schmidt, C. Stengl, C. P. Karger, and O. Jäkel (2024). “Secondary neutrons in proton and light ion beam therapy: a review of current status, needs and potential solutions”. In: *Radiation Measurements* 176, p. 107214. ISSN: 1350-4487. DOI: https://doi.org/10.1016/j.radmeas.2024.107214.

Warren, K. M. et al. (2005). “The contribution of nuclear reactions to heavy ion single event upset cross section measurements in a high-density SEU hardened SRAM”. In: *IEEE Transactions on Nuclear Science* 52.6, pp. 2125–2131. ISSN: 1558-1578. DOI: 10.1109/TNS.2005.860677.

Weller, R. A. et al. (2009). “General Framework for Single Event Effects Rate Prediction in Microelectronics”. In: *IEEE Transactions on Nuclear Science* 56.6, pp. 3098–3108. ISSN: 1558-1578. DOI: 10.1109/TNS.2009.2033916.

Weulersse, C., M. Mazurek, C. D. Pinas, R. Mills, and B. Guerard (2023). “Thermal Neutron Measurements Inside an Aircraft for SEE Assessment”. In: *IEEE Transactions on Nuclear Science* 70.8, pp. 1548–1554. ISSN: 1558-1578. DOI: 10.1109/TNS.2023.3256095.

Weulersse, C. et al. (2018). “Contribution of Thermal Neutrons to Soft Error Rate”. In: *IEEE Transactions on Nuclear Science* 65.8, pp. 1851–1857. ISSN: 1558-1578. DOI: 10.1109/TNS.2018.2813367.

Wilkinson, J. D., C. Bounds, T. Brown, B. J. Gerbi, and J. Peltier (2005). “Cancer-radiotherapy equipment as a cause of soft errors in electronic equipment”. In: *IEEE Transactions on Device and Materials Reliability* 5.3, pp. 449–451. ISSN: 1530-4388.

Willems, E. et al. (2003). *18/05/2003: Rapport concernant les élections du 18 mai 2003*. Report. URL: https://www.poureva.be/article.php3?id_article=32&lang=fr.

Wu, H. and D. Wang (2007). “Radiation-induced Alarm and Failure of an Implanted Programmable Intrathecal Pump”. In: *The Clinical Journal of Pain* 23.9. ISSN: 0749-8047.

Yahagi, Y. et al. (2007). “A Novel Feature of Neutron-Induced Multi-Cell Upsets in 130 and 180 nm SRAMs”. In: *IEEE Transactions on Nuclear Science* 54, pp. 1030–1036.

Yap, M. L., E. Zubizarreta, F. Bray, J. Ferlay, and M.l Barton (2016). “Global Access to Radiotherapy Services: Have We Made Progress During the Past Decade?” In: *Journal of Global Oncology* 2.4, pp. 207–215. DOI: 10.1200/jgo.2015.001545.

Yeung, C. et al. (2019). “Radiotherapy for patients with cardiovascular implantable electronic devices: an 11-year experience”. In: *Journal of Interventional Cardiac Electrophysiology* 55.3, pp. 333–341. ISSN: 1572-8595. DOI: 10.1007/s10840-018-0506-0.

Yoshida, T., S. Murayama, K. Yasui, T. Tomida, and A. Urikura (2023). “Pacemaker Malfunction During Passive Proton Beam Therapy for Localized Prostate Cancer: Case Reports and a Literature Review”. In: *Cureus* 15.

Zaremba, T., A. R. Jakobsen, A. M. Thogersen, L. Oddershede, and S. Riahi (2014). “The effect of radiotherapy beam energy on modern cardiac devices: an in vitro study”. In: *Europace* 16.4, pp. 612–6. ISSN: 1532-2092 (Electronic) 1099-5129 (Linking). DOI: 10.1093/europace/eut249.

Zaremba, T. et al. (2015). “Risk of Device Malfunction in Cancer Patients with Implantable Cardiac Device Undergoing Radiotherapy: A Population-Based Cohort Study”. In: *Pacing and Clinical Electrophysiology* 38.3, pp. 343–356. ISSN: 0147-8389. DOI: https://doi.org/10.1111/pace.12572.

Zaunick, H.-G. (2022). Personal Communication.

Zecchin, M. et al. (2016). “Malfunction of cardiac devices after radiotherapy without direct exposure to ionizing radiation: mechanisms and experimental data”. In: *Europace* 18.2, pp. 288–93. ISSN: 1532-2092 (Electronic) 1099-5129 (Linking). DOI: 10.1093/europace/euv250.

Ziegler, J. F. and W.A. Lanford (1979). “Effect of cosmic rays on computer memories”. In: *Science* 206.4420, pp. 776–788. ISSN: 0036-8075.

Ziegler, J. F., M. D. Ziegler, and J. P. Biersack (2010). “SRIM – The stopping and range of ions in matter (2010)”. In: *Nuclear Instruments and Methods in Physics Research Section B: Beam Interactions with Materials and Atoms* 268.11, pp. 1818–1823. ISSN: 0168-583X. DOI: https://doi.org/10.1016/j.nimb.2010.02.091.

Zweng, A., R. Schuster, R. Hawlicek, and H. S. Weber (2008). “Life-Threatening Pacemaker Dysfunction Associated with Therapeutic Radiation: A Case Report”. In: *Angiology* 60.4, pp. 509–512. ISSN: 0003-3197. DOI: 10.1177/0003319708315305.